

A Computational Framework for Mineralogical Thermodynamics of the Earth's Mantle

(Dissertation)

vorgelegt von Thomas C. Chust

(geboren am 11. Oktober 1981 in Freising, Deutschland),

eingereicht an der Fakultät Biologie, Chemie, Geowissenschaften
der Universität Bayreuth

zur Erlangung des Dr. rer. nat.

Die vorliegende Arbeit wurde in der Zeit von März 2009 bis August 2017 in Bayreuth am Bayerischen Geoinstitut unter Betreuung von Herrn Dr. Gerd Steinle-Neumann angefertigt.

Vollständiger Abdruck der von der Fakultät für Biologie, Chemie und Geowissenschaften der Universität Bayreuth genehmigten Dissertation zur Erlangung des akademischen Grades eines Doktors der Naturwissenschaften (Dr. rer. nat.).

Dissertation eingereicht am:	15.08.2017
Zulassung durch die Promotionskommission:	28.09.2017
Wissenschaftliches Kolloquium:	21.12.2017

Amtierender Dekan: Prof. Dr. Stefan Peiffer

Prüfungsausschuss:	
Dr. Gerd Steinle-Neumann	(1. Gutachter)
Prof. Dr. Daniel Frost	(2. Gutachter)
Dr. Hauke Marquardt	(Vorsitz)
Prof. Dr. Gregor Golabek	

Summary

We present a newly developed software framework that evaluates phase equilibria and thermodynamics of multicomponent systems by Gibbs energy minimization, with application to mantle petrology. The code EoS is versatile in terms of the formulation of equations-of-state and mixing properties, and allows for the computation of properties of single phases, solution phases and multiphase aggregates. Currently, it contains three equation-of-state formulations widely used in high-pressure mineralogy and petrology: The Caloric–Murnaghan, Caloric–Modified-Tait and Birch–Murnaghan–Mie–Debye–Grüneisen models, together with published databases. Models and databases can be changed transparently without requiring any modification of EoS, using its application programming interface or the command line interface. Due to its modular design, documented programming interfaces and easily editable databases in a text-based format, the program can readily be extended with new formulations of equations-of-state and changes or extensions to thermodynamic datasets. The provided model of solid solutions can be combined with any equation-of-state for the solution endmembers. The code is distributed as open source software and can be found on the accompanying optical disc or on its project website (<https://bitbucket.org/chust/eos>).

The energy minimization code used to determine stable phase assemblages employs both linear programming and non-linear optimization techniques. Solution phases with varying composition are represented by multiple candidate pseudocompounds, each with a fixed composition, to linearize the problem of selecting stable phases. The representation in pseudocompounds allows for an application of the simplex method to find the energetic optimum efficiently. Pseudocompound compositions are determined by non-linear optimization, requiring an iteration scheme between the two optimization steps to refine the solution. The entire optimization process is implemented independently of the equations-of-state and can be used with any database or subset of phases. We have implemented the physical model code in F#, a programming language that combines aspects of other object-oriented and functional languages. The structure of the physical theory lends itself to an object-oriented design, while many of the implementation details can be formulated concisely using a functional approach. Compiler support for physical units helps to guarantee implementation correctness without imposing a runtime penalty. We have implemented the equations-of-state and various numerical algorithms, e.g., root finding and the non-linear optimization ourselves. Performance-critical operations, e.g., communication between parallel processes and the linear optimizer, which benefit from an implementation in native code, are delegated to external libraries.

We demonstrate the use of the program by reproducing and comparing physical properties of mantle phases and assemblages with previously published work and experimental data. We successively increase the problem complexity, starting from elastic and thermal single phase properties, moving to solution phase behavior and phase equilibria computations for simplified compositions up to six-component compositions. We explore phase relations and physical properties in the Earth's mantle using reduced pyrolite compositions in the MgO-SiO₂, FeO-MgO-SiO₂, CaO-FeO-MgO-SiO₂, FeO-MgO-Al₂O₃-SiO₂, CaO-FeO-MgO-Al₂O₃-SiO₂, and Na₂O-CaO-FeO-MgO-

Al_2O_3 - SiO_2 systems. In addition, we consider models for dry bulk oceanic crust and depleted mantle compositions, and a mixture of these two lithologies, sometimes used as an alternative model for mantle petrology (mechanical mixture). Chemically complex systems allow us to trace the budget of minor chemical components in order to explore whether they lead to the formation of new phases or extend stability fields of existing ones. Notable examples are the appearance of clinopyroxenes with the addition of Ca and significant extensions of garnet and akimotoite stability fields with the addition of Al and with increasing silica fraction.

Self-consistently computed thermophysical properties for a homogeneous pyroclitic mantle and the mechanical mixture show no discernible differences that would require a heterogeneous mantle structure as has been suggested previously. While different phase transitions dominate the thermoelastic behavior of bulk oceanic crust compared to depleted mantle or pyrolite, the differences between elasticity profiles predicted for pyrolite and the mechanical mixture are smaller than the differences between seismological 1D models and the synthetic profiles.

We explore inherent limitations in the framework of mantle thermodynamics: Among the equations-of-state a tradeoff exists between accuracy and robustness of extrapolations to high pressures and temperatures. To some degree, all models suffer from uncertainties introduced by fitting a large number of correlated model parameters to measurements of a few physical properties. The sensitivity of the optimization results to the energy calibration of solution models and the availability of phases hosting all chemical components of a bulk composition limit the applicability of databases to certain composition ranges. Looking beyond the present work, we provide suggestions on how thermodynamics of mantle mineralogy can advance the study of Earth's interior, by directly predicting geophysical observables rather than relying on the inversion and interpretation of seismic properties alone.

Zusammenfassung

In dieser Arbeit stellen wir ein neu entwickeltes Softwarepaket vor, das Phasengleichgewichte und Thermodynamik in Multikomponentensystemen durch Minimierung der Gibbs-Energie auswertet und wendet es auf die Petrologie des Erdmantels an. Der Code EoS ist vielseitig in Bezug auf die Formulierung der Zustandsgleichung und Lösungseigenschaften. Er erlaubt die Berechnung von Eigenschaften einzelner Phasen, Lösungsphasen und Aggregaten mehrerer Phasen. Im Moment enthält er drei Zustandsgleichungsformulierungen, die in der Hochdruckmineralogie und Petrologie verbreitet Anwendung finden: Die Modelle Kalorisch-Murnaghan, Kalorisch-Modifiziert-Tait und Birch-Murnaghan-Mie-Debye-Grüneisen, zusammen mit veröffentlichten Datenbanken. Modelle und Datenbanken können transparent ausgetauscht werden, ohne dass eine Veränderung von EoS selbst notwendig wäre, von Code der seine Applikationsprogrammierungsschnittstellen nutzt oder von Benutzerinteraktionen über die Kommandozeile. Aufgrund seines modularen Designs, seiner dokumentierten Programmierschnittstellen und leicht editierbaren Datenbanken in Textform kann das Programm ohne Probleme durch neue Formulierungen der Zustandsgleichung sowie Änderungen oder Erweiterungen der thermodynamischen

Datenbanken ausgebaut werden. Das mitgelieferte Modell für feste Lösungen lässt sich mit jeder Zustandsgleichung für die Lösungskomponenten kombinieren. Der Code wird unter einer freien Softwarelizenz verteilt und findet sich auf dem beiliegenden optischen Datenträger und seiner Projektwebseite (<https://bitbucket.org/chust/eos>).

Der Minimierungscode für Gibbs-Energie, mit dem stabile Phasenzusammensetzungen ermittelt werden, nutzt sowohl Techniken der linearen Programmierung als auch der nicht-linearen Optimierung. Lösungsphasen mit variabler Zusammensetzung werden während der Berechnungen durch mehrere Pseudokomponenten repräsentiert, die jeweils eine feste Zusammensetzung haben, so dass das Problem der Auswahl stabiler Phasen auf ein lineares Optimierungsproblem reduziert wird. Die Darstellung in Pseudokomponenten erlaubt die Verwendung der Simplex-Methode um das energetische Optimum effizient zu finden. Die Zusammensetzungen der Pseudokomponenten werden durch nicht-lineare Optimierung bestimmt, was einen iterativen Lösungsprozess erfordert, der zwischen beiden Optimierungsschritten hin und her wechselt um die Lösung zu verfeinern. Der gesamte Optimierungsprozess ist unabhängig von den Zustandsgleichungen implementiert und kann auf jede Datenbank oder Teilauswahl von Phasen angewendet werden. Wir haben den physikalischen Modellcode in F# implementiert, einer Sprache, die Aspekte der objektorientierten und funktionalen Programmierung kombiniert. Die Struktur der physikalischen Theorie eignet sich gut für eine objektorientierte Umsetzung, während viele der Implementationsdetails mit einem funktionalen Ansatz elegant formuliert werden können. Compilerunterstützung für physikalische Einheiten hilft dabei, eine korrekte Implementation sicherzustellen ohne zusätzliche Laufzeitkosten zu verursachen. Wir haben die Zustandsgleichungen und diverse numerische Algorithmen selbst implementiert, zum Beispiel Nullstellensuche und nicht-lineare Optimierung. Für lauffzeitkritische Operationen, zum Beispiel Kommunikation zwischen parallelen Prozessen und lineare Optimierung, die von einer Implementation in maschinenspezifischem Code profitieren, greifen wir auf externe Bibliotheken zurück.

Wir zeigen die Anwendung des Programms, indem wir physikalische Eigenschaften von Phasen und Phasenzusammensetzungen des Erdmantels reproduzieren und mit bereits veröffentlichten Arbeiten und experimentellen Daten vergleichen. Wir steigern sukzessive die Komplexität der Anwendungsfälle, ausgehend von elastischen und thermischen Eigenschaften einzelner Phasen, über das Verhalten von Lösungsphasen und Phasengleichgewichtsberechnungen für vereinfachte Zusammensetzungen bis hin zu Sechs-Komponenten-Zusammensetzungen. Wir analysieren die Phasenbeziehungen und physikalischen Eigenschaften im Erdmantel unter Verwendung reduzierter Pyrolitzusammensetzungen in den Systemen MgO-SiO_2 , FeO-MgO-SiO_2 , CaO-FeO-MgO-SiO_2 , $\text{FeO-MgO-Al}_2\text{O}_3\text{-SiO}_2$, $\text{CaO-FeO-MgO-Al}_2\text{O}_3\text{-SiO}_2$, und $\text{Na}_2\text{O-CaO-FeO-MgO-Al}_2\text{O}_3\text{-SiO}_2$. Zusätzlich betrachten wir Modelle für die Zusammensetzung von ozeanischer Kruste (ohne flüchtige Bestandteile) und verarmtem Mantel, sowie eine Mischung dieser zwei Lithologien, die manchmal als alternatives Modell für die Petrologie des Mantels verwendet wird (mechanische Mischung). Die komplexen chemischen Systeme erlauben es, die Verteilung der chemischen Nebenkomponten auf die stabilen Phasen zu verfolgen und zu sehen, ob sie zum Auftreten neuer Phasen führen oder die Stabilitätsfelder bestehender Phasen vergrößern. Zum

Beispiel treten die Klinopyroxene erst mit der Zugabe von Ca auf und die Stabilitätsfelder von Granat und Akimotoit vergrößern sich signifikant mit der Zugabe von Al und mit steigendem Silikatgehalt.

Selbstkonsistent berechnete thermophysikalische Eigenschaften für einen homogenen pyrolitischen Mantel und die mechanische Mischung zeigen keine erkennbaren Unterschiede, die eine heterogene Mantelstruktur erfordern würden, wie es manche Studien nahegelegt haben. Obwohl das thermoelastische Verhalten der ozeanischen Kruste und des verarmten Mantels oder Pyrolits von unterschiedlichen Phasenübergängen bestimmt wird, sind die Unterschiede zwischen den berechneten elastischen Profilen für Pyrolit und die mechanische Mischung geringer als die Unterschiede zwischen seismologischen 1D-Modellen und den synthetischen Profilen.

Wir diskutieren inhärente Beschränkungen im Rahmen der Mantelthermodynamik: Kompromisse bestehen zwischen der Genauigkeit und einem robusten Extrapolationsverhalten zu hohem Druck und hoher Temperatur verschiedener Formulierungen der Zustandsgleichung. In einem gewissen Umfang sind alle Modelle von Unsicherheiten betroffen, die bei der Anpassung einer großen Zahl korrelierter Modellparameter an Messwerte weniger physikalischer Eigenschaften entstehen. Die Empfindlichkeit des Optimierungsergebnisses für die energetische Kalibrierung des Lösungsmodells und die Verfügbarkeit von Phasen, welche alle chemischen Komponenten der Gesamtzusammensetzung enthalten, beschränken den Anwendungsbereich der Datenbanken auf bestimmte Zusammensetzungsbereiche. Über die vorliegende Arbeit hinaus geben wir Anregungen, wie die Thermodynamik der Mantelmineralogie die Untersuchung des Erdinneren voranbringen könnte, indem sie direkte Vorhersagen von geophysikalischen Beobachtungen erlaubt statt ausschließlich von der Inversion und Interpretation seismischer Eigenschaften abhängig zu sein.

Contents

1	Introduction	9
1.1	Chemical Thermodynamics	10
1.2	Applications to the Earth's Structure	11
2	Thermodynamic Models	13
2.1	The Caloric–Murnaghan Model	15
2.2	The Caloric–Modified-Tait Model	18
2.3	The Birch-Murnaghan–Mie-Debye-Grüneisen Model	19
2.4	Shear Modulus	23
2.5	Order-Disorder Transition	23
2.6	Solution Phases	24
2.7	Multiphase Aggregates	26
3	Software Implementation	29
3.1	Code Design	30
3.2	Language Choice	31
3.3	Numerical Details	32
3.4	Performance Measurements	35
4	Application of Thermodynamic Models	37
4.1	Mineral Properties	37
4.1.1	Volumetric Properties	37
4.1.2	Caloric Properties	39
4.1.3	Gibbs Energy	40
4.2	Phase Diagrams	43
4.2.1	Phase Equilibria Involving Stoichiometric Phases	43
4.2.2	Configurational and Excess Mixing Properties	43
4.2.3	Phase Equilibria Involving Solid Solutions	48
4.3	Elastic Properties	51
4.3.1	Elasticity of Garnets	51
4.3.2	Elasticity of MgSiO ₃ Phases	52
5	Phase Equilibria in the Mantle	55
5.1	Pyrolite Assemblages	55
5.1.1	MS System	58
5.1.2	FMS System	59
5.1.3	CFMS System	60

5.1.4	FMAS System	62
5.1.5	CFMAS System	64
5.1.6	NCFMAS System	66
5.2	Element Partitioning in Pyrolite	67
5.3	Petrology of Slab Lithologies	71
5.3.1	Phase Relations in Depleted Mantle	74
5.3.2	Phase Relations in Bulk Oceanic Crust	75
6	Thermochemical Properties of the Mantle	79
6.1	Adiabatic Temperatures	79
6.1.1	Isentrope in Pyrolite Mantle	79
6.1.2	Isentropes in Slab Lithologies	81
6.2	Seismic Properties	82
6.2.1	Density and Elasticity Profiles of Individual Lithologies	82
6.2.2	Homogeneous vs. Mechanically Mixed Mantle	85
7	Current Limitations and Future Developments	87
7.1	Coverage, Consistency and Accuracy of Thermodynamic Models	87
7.2	Consequences for Geophysical Applications	89
7.2.1	Geodynamic Equation-of-State	90
7.2.2	Forward Seismic Models	91
A	Database Differences	93
B	Tables	95
	Acknowledgements	107
	Bibliography	109

Chapter 1

Introduction

The study of the Earth is almost as old as mankind itself. Understanding how the planet we all call our home works is of natural interest to everyone to some degree. It also poses fundamental challenges to our mind because processes at the planetary scale span large distances and time intervals compared to what we are used to in everyday life – and in the other extreme, delving into the details of materials found in the Earth requires the study of processes on microscopic length and time scales. To make these challenges manageable, scientists use theories and models of reality that can be manipulated at a human scale while trying to describe processes at a geologic or microscopic scale.

Thermodynamics is a branch of physics of particular interest in this respect, because it is based on statistical theory and abstracts details of behaviour at the atomic scale, yielding descriptions of processes at a more macroscopic scale. Thermodynamics also links readily quantifiable properties, such as thermal energy, with more abstract concepts such as the structure of matter and its changes at certain environmental conditions. It is therefore relevant to many aspects in the evolution of the Earth and its present behaviour, but a complete picture usually requires multi-disciplinary approaches: Accretion of a planet from particles and rocks can only be understood using notions of heat budget and phase transformations under the influence of pressure or temperature changes, together with orbital mechanics and kinetic energy estimates. What mineral types can be found at different depths in a terrestrial planet depends on the energetics of phase transformations as well as on chemistry and crystal structures. How material is transported or segregated by flow in the Earth's mantle or core depends on buoyancies, friction coefficients and heat transport properties as well as on radioactive heat generation, fluid mechanics, and chemical compatibility of available components.

Computers have become increasingly essential in handling the complex quantitative models we build in the geosciences. Simulation software can serve as a virtual laboratory performing numerical experiments at large or small scales that are not readily accessible to real experiments. Numerical algorithms allow computational approaches to problems that would be prohibitively time-consuming to tackle with manual analysis. With the increasing degree of dependence on software to model the studied problem domains in the geosciences, the correctness, robustness and reproducibility of computational results becomes more critical.

1.1 Chemical Thermodynamics

Knowledge of stable phase assemblages and their material properties is a prerequisite in diverse areas of chemistry, material sciences and also geosciences. Examples include the study of chemistry in liquids [e.g., McDonald and Floudas, 1995], material properties of various kinds of solids [e.g., Lee and Meyer, 1986, Schmid-Fetzer and Gröbner, 2001], but also engineering topics such as rocket engine design [e.g., McBride et al., 2002], or applications to petrology [e.g., de Capitani and Brown, 1987]. Strategies to determine phase stability and to compute the material properties rely on thermodynamic models and use various mathematical methods such as linear or non-linear optimization [e.g., Bale et al., 2002, Chang et al., 2004, Connolly, 2005, Dantzig, 1963, Eriksson and Rosen, 1973] or non-linear equation solvers [e.g., Lukas et al., 2007, Powell et al., 1998]. Models rely on thermodynamic datasets, obtained through assessment of experimental data or first principles calculations, to describe the behavior of materials [e.g., Ansara et al., 1998, Bale et al., 2009, Bale and Eriksson, 1990, Kroupa, 2013, McBride et al., 2002, Shang et al., 2008, Stixrude and Lithgow-Bertelloni, 2005b, 2011, Wang et al., 2013] and they share the fundamental principle that phase stability criteria are specified in terms of a thermodynamic potential. Pressure P , temperature T , and bulk composition x often form the most convenient choice of independent variables, with Gibbs energy being the corresponding potential. The stable phase assemblage is then obtained by minimizing Gibbs energy of the system [e.g., Lukas et al., 2007, Schmid-Fetzer and Gröbner, 2001, Stowe, 2007, White et al., 1958].

In a very limited number of cases, conditions of chemical equilibrium between some phases can be determined analytically, e.g., by matching the chemical potentials of coexisting binary solutions [Lukas et al., 1977, Powell et al., 1998, Wen and Nekvasil, 1994]. Alternatively, Gibbs energy can be minimized with linear algebraic algorithms [Connolly and Petrini, 2002, Eriksson and Hack, 1990].

The functional form of Gibbs energy also includes sufficient information to derive all other state variables of the system and its phases, including properties such as the density or the bulk modulus. A thermodynamic model for mineral phases and aggregates provides a natural framework to analyze the dependence of these thermomechanical properties on P , T and x and to determine their relationships consistently. Combined with the possibility to compute equilibrium phase assemblages, macroscopic thermodynamics offers a comprehensive solution for modeling the nature and properties of materials, interpolation between experimental results or extrapolation to conditions that may not be readily accessible in experiments. A thermodynamic model can also be used to predict conditions to explore in the laboratory, for example the modeled location of phase boundaries, or thermoelastic parameters may be compared to experimental results, thus facilitating both design and evaluation of experiments. However, care is required to maintain internal consistency of the formulation when different physical models are combined into a thermodynamic potential, otherwise derived properties become dependent on integration paths or differentiation order [Brosh et al., 2007].

1.2 Applications to the Earth's Structure

In solid Earth sciences, knowledge of stable phase assemblages and their material properties is an important link between petrology, seismology and geodynamics. It is, among others, relevant for the interpretation of seismic wave speed variations imaged by tomography [e.g., Cobden et al., 2008, Matas et al., 2007, Schuberth et al., 2009a] or for linking thermoelastic and geodynamic models based on mantle convection [e.g., Christensen and Yuen, 1985, Ita and King, 1994, 1998, Nakagawa et al., 2009].

Our understanding of the Earth's structure and composition is based on indirect observations of very different phenomena: The behaviour of seismic wave propagation at a global scale shows that large spherical shells inside the Earth can be distinguished by the discontinuities of elastic properties between them [e.g., Dziewonski and Anderson, 1981, Ritsema et al., 2011]. Other hand, the bulk composition of the Earth can be constrained by cosmochemical or geochemical observations. To first order, the abundance of chemical elements in the Earth is thought to be similar to that of the entire solar system, and by extension of solar nebulae, that can be characterized by spectroscopic methods [e.g., Asplund et al., 2009, Palme and O'Neill, 2016]. The composition of chondritic meteorites also provides information about the chemical components that were present during the aggregation stage of the planet [e.g., McDonough and Sun, 1995, Palme, 1988]. On the present Earth, magmas and igneous rocks may be studied to infer information about the source material from which they formed; in particular, the composition of mid-oceanic ridge basalts provides valuable information on the composition of the mantle [e.g., Palme and O'Neill, 2016, Workman and Hart, 2005].

Mineral physics is required to interpret these sources of information on a common basis. The link between chemical phase transitions and seismologically observable discontinuities has been studied extensively [e.g., Ahrens, 1973, Anderson, 1970, Burdick and Anderson, 1975]. An important part of any such study is the computation of elastic properties for a given mineral assemblage and an equation of state for its constituent minerals. The approaches used to determine the phase assemblages of interest, where experiments are not readily possible, have evolved from assessments for selected bulk compositions and phases [e.g., Akaogi et al., 1987, Saxena and Eriksson, 1983, Wood and Holloway, 1984] towards more generally applicable tools to compute phase diagrams for different bulk compositions and sets of phases [e.g., Fabrichnaya, 1995, Matas, 1999].

In the first comprehensive study combining thermodynamic theory to predict phase stability fields and seismological evidence, Ita and Stixrude [1992] have examined the influence of bulk chemistry and phase transitions on the seismic observables in the Earth's mantle, noting a particular sensitivity of v_s to the chemistry of the mantle and varying degrees of agreement between their model and observations of seismic velocities in the upper and lower mantle. The Birch-Murnaghan-Mie-Debye-Grüneisen equation-of-state introduced by this study forms the basis for further work by Stixrude and Lithgow-Bertelloni [2005b, 2011]. Nakagawa et al. [2009] have first used this thermodynamic framework in conjunction with mantle convection simulations to examine the implications for seismic anomalies in the Earth's mantle.

Chemia et al. [2015], Ita and King [1998] and Maierová et al. [2012], for example, have studied the effects of bulk chemistry, phase transitions and transport properties on the structure of subduction zones. The geometry of subduction zones consisting of chemically distinct layers makes them particularly interesting to explore the influence of bulk chemistry variations and the interaction of regions with different thermoelastic parameter regimes. Connolly and Kerrick [2002] and Chemia et al. [2015] also address the presence of volatiles and their loss through metamorphic reactions, which in turn determines volcanic degassing in arc magmatism [Zellmer et al., 2014].

Komabayashi [2014] has modeled the behavior of iron and iron–oxygen liquids under high pressures and studied the implications for the elastic properties of the Earth’s core and its oxygen content, that may also be relevant for the interpretation of seismic low-velocity anomalies at the core mantle boundary [Garnero et al., 1993, Tanaka, 2007]. However, the equation-of-state applied in that study separates thermal and elastic energy contributions in a problematic way, resulting in thermoelastic parameters that are not thermodynamically self-consistent [Brosh et al., 2007].

Several automated approaches exist to perform phase equilibria calculations applicable within the context of geosciences. Software like THERMOCALC [Powell et al., 1998] and SOLV CALC [Wen and Nekvasil, 1994] find equilibrium assemblages using analytical solutions for special thermodynamic systems. General Gibbs energy minimization approaches are applied in the widely used petrological and geochemical software packages MELTS [e.g., Asimow and Ghiorso, 1998, Ghiorso, 1994, Ghiorso and Sack, 1995], PERPLE_X [Connolly, 2005] or THERIAK [e.g., de Capitani and Petrakakis, 2010].

In this thesis, we present a new simulation package and phase equilibrium solver, EoS, which is designed to independently implement various thermodynamic formulations, to test their internal consistency and to facilitate the construction of new model combinations or extensions. It has no implicit temperature and pressure limitations and can be applied to all conditions for which the thermodynamic database in use has been calibrated. We compare the properties of simple phases and solutions predicted using the Caloric–Murnaghan (Section 2.1), Caloric–Modified-Tait (Section 2.2) and Birch–Murnaghan–Mie–Debye–Grüneisen (Section 2.3) formulations with each other and with experimental data.

We take an approach similar to PERPLE_X or THERIAK, where the mathematical formulation of Gibbs energy minimization is essentially a linear programming problem, complicated by the presence of solution phases, which introduce non-linearity. In terms of computational speed, such algorithms scale well to tens of phases [Spielman and Teng, 2001]; only the processing of the non-linear behavior of individual solutions can negatively affect the performance.

Using bulk chemistry models with varying numbers of chemical oxide components and tracing the budget of minor chemical components, we explore the influence of each component on the presence and stability of phases in the stable assemblage and the partitioning of components between coexisting phases. We also extract information such as potential temperatures and thermoelastic properties such as seismic velocities for stable mantle phase assemblages and discuss implications of our results in comparison to the existing work on seismic velocity profiles and mantle convection.

Chapter 2

Thermodynamic Models

Thermodynamic properties of pure, stoichiometric substances are related to reference conditions, usually $T_0 = 298.15$ K and $P_0 = 10^5$ Pa, i.e., ambient conditions. Calculating Gibbs energy of a pure phase at P and T of interest requires a theoretical or empirical physical model, i.e., an equation-of-state [e.g., Connolly, 2009, Poirier, 2000]. Conventionally, most models use two additive energy contributions, which are computed along two alternative integration path segments (Figure 2.1):

- (i). isobaric heating to T at P_0 (caloric contribution), followed by isothermal compression to P at constant T (elastic contribution):

$$G(P, T) = G_0 + [G(P_0, T)]_{T_0}^T + [G(P, T)]_{P_0}^P, \quad (2.1)$$

or

- (ii). isothermal compression to P at T_0 (elastic contribution), followed by isochoric heating to T at constant $V = V(P, T_0)$ (thermal contribution):

$$G(P, T) = G_0 + [G(P, T_0)]_{P_0}^P + [G(V, T)]_{T_0}^T, \quad (2.2)$$

where the thermal contribution to Gibbs energy (G) is obtained through the relation to Helmholtz energy (A):

$$G(V, T) = A(V, T) + P(V, T) \cdot V. \quad (2.3)$$

In caloric models of type (i), the temperature effect on volume and compressibility is typically incorporated through phenomenological models using thermal expansivity and/or isobaric heat capacity [e.g., Fabrichnaya et al., 2004, Holland and Powell, 1998, Matas, 1999], fitted to experimental data. Their functional form, often polynomials, remains empirical, which results in poor extrapolation behavior to low and high T . In assessing a thermodynamic model applicable to the Earth's upper mantle and transition zone, Holland and Powell [2011] and Holland et al. [2013] adopted the polynomial caloric approximation, combined with the modified Tait equation-of-state, to calibrate more than 250 mineral phases and melt species.

By contrast, the thermal contribution at constant volume in models of type (ii) is well suited for an analytical treatment based on statistical mechanics, such as in the

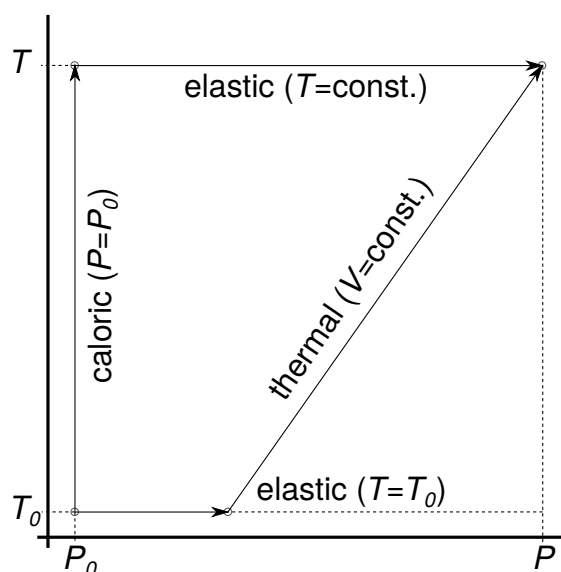


Figure 2.1: Integration path segments in P - T space used in the physical models implemented in the EoS software. Starting at reference conditions (P_0, T_0) , the computation of Gibbs energy of a phase may follow either isobaric heating at P_0 (caloric) and then isothermal compression at T (elastic) or isothermal compression at T_0 (elastic) and then isochoric heating (thermal), keeping the volume fixed.

Einstein or Debye model [e.g., Poirier, 2000]. As volume directly influences the behavior of lattice vibrations, computing the thermal contribution to G at constant volume is convenient in this context. The approach achieves acceptable extrapolation behavior and obeys to theoretical limits, at the expense of accurate reproduction of experimental data. Ita and Stixrude [1992] have introduced a physical model of type (ii) based on the Birch-Murnaghan–Mie-Debye-Grüneisen theory that has subsequently been refined by Stixrude and Lithgow-Bertelloni [2005b, 2011]. This model, combined with its thermodynamic databases for many mantle phases, has been used widely in geophysical studies of mantle structure [e.g., Cammarano et al., 2011, Cobden et al., 2008, 2009, Davies et al., 2012, Nakagawa et al., 2009, Schuberth et al., 2012, 2015].

Details of the model formulations by Fabrichnaya et al. [2004] (Caloric–Murnaghan), Holland et al. [2013] (Caloric–Modified-Tait) and Stixrude and Lithgow-Bertelloni [2005b, 2011] (Birch-Murnaghan–Mie-Debye-Grüneisen) are presented in Section 2.1 through 2.4. The EoS software implements these three models to calculate Gibbs energy of condensed phases at elevated pressure and temperature.

Thermodynamic properties of minerals with a second-order phase transition (e.g. α -quartz– β -quartz or stishovite– CaCl_2 -structured SiO_2) or with changes in element ordering between multiple crystallographic sites (e.g. feldspar or spinel) are treated with order-disorder theory. Carpenter et al. [1994] and Holland and Powell [1998] introduced the Landau tricritical theory to mineral physics applications. There, the standard thermodynamic properties refer to a completely disordered phase (G_{dis}) and the Landau contribution (G_{L}), which accounts for progressive ordering with decreasing temperature, is added to obtain a value for the partially ordered phase (G_{ord}):

$$G_{\text{ord}}(P, T) = G_{\text{dis}}(P, T) + G_{\text{L}}(P, T). \quad (2.4)$$

The treatment of G_L is discussed further in Section 2.5.

Numerous minerals of geological and geophysical interest have variable chemical composition and are described as solutions. Their thermodynamic properties consist of a linear combination of endmember properties (mixing), configurational (ideal) and excess (non-ideal) mixing contributions [e.g., Ganguly, 2008, Hillert and Staffansson, 1970] as follows:

$$G = \sum_i x_i G_i - T S_{\text{cf}} + G_{\text{ex}}, \quad (2.5)$$

where i refers to the solution endmembers and G_i is their standard Gibbs energy. S_{cf} represents the configurational entropy of the solution and G_{ex} is the excess Gibbs energy of mixing. The treatment of configurational and excess contributions to Gibbs energy in solutions is detailed in Section 2.6.

Thermodynamic and other properties of mineral assemblages or multiphase aggregates are computed as linear combinations with appropriate weights. Different properties (extensive vs. elastic) require different weights, as discussed in detail in Section 2.7.

2.1 The Caloric–Murnaghan Model

The model follows a P - T path from the reference conditions that combines isobaric heating at reference P , formulated using an empirical heat capacity approximation, and high- T compression, based on the Murnaghan equation-of-state [Murnaghan, 1944] (Figure 2.1). This approach has been applied by Holland and Powell [1998], Matas [1999], Fabrichnaya et al. [2004] and Piazzoni et al. [2007]. The dataflow is illustrated in Figure 2.2.

The molar Gibbs energy of a phase at P and T of interest consists of the following contributions:

$$G(P, T) = H_0 + [H(P_0, T)]_{T_0}^T - T (S_0 + [S(P_0, T)]_{T_0}^T) + [G(P, T)]_{P_0}^P, \quad (2.6)$$

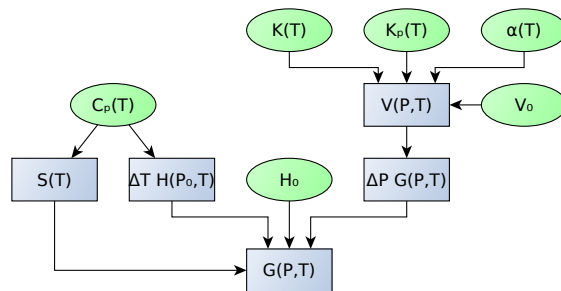


Figure 2.2: Data flow in the Caloric–Murnaghan model for the computation of Gibbs energy used by Fabrichnaya et al. [2004]. Gibbs energy G is assembled from an elastic part $\Delta P G(P, T) = [G(P, T)]_{P_0}^P$, following the Murnaghan formalism, and a thermal part $\Delta T H(P, T) = [H(P, T)]_{T_0}^T$, based on a polynomial representation of the heat capacity. Model parameters (taken from a database of phases at runtime) are enclosed in ellipses and shaded green while the computational steps of the model code are represented by rectangular boxes shaded blue; model parameters that are functions of T are polynomials in T . Abbreviations for physical parameters used in the flow chart are listed in Table B.1.

where subscript 0 indicates a quantity at reference conditions (P_0, T_0) . The molar caloric enthalpy $H(P_0, T)$ and the entropy contribution at reference pressure $S(P_0, T)$ are evaluated using the isobaric heat capacity C_P :

$$[H(P_0, T)]_{T_0}^T = \int_{T_0}^T C_P(T) dT, \quad (2.7)$$

and

$$[S(P_0, T)]_{T_0}^T = \int_{T_0}^T \frac{C_P(T)}{T} dT, \quad (2.8)$$

where

$$C_P(T) = \sum_i c_i T^{p_i}. \quad (2.9)$$

The number and values of coefficients and exponents in Equation (2.9) are generally variable and chosen empirically [Bale et al., 2002, Fabrichnaya et al., 2004, Holland and Powell, 1998]. The implementation in EoS allows for the specification of arbitrary polynomials, which are differentiated and integrated analytically. For instance, Fabrichnaya et al. [2004] and Holland and Powell [1998, 2011] use seven and four parameters, respectively, with positive and negative integer and rational exponents.

The contribution to G from compression at elevated T is computed as the volume-work integral

$$[G(P, T)]_{P_0}^P = \int_{P_0}^P V(P, T) dP, \quad (2.10)$$

with molar volume V . In the model of Fabrichnaya et al. [2004], it is described by the second-order Murnaghan equation-of-state:

$$V(P, T) = V(P_0, T) \left(1 + \frac{\partial_P K(T) P}{K(T)} \right)^{-\frac{1}{\partial_P K(T)}}, \quad (2.11)$$

where K is the isothermal bulk modulus and $\partial_P K$ its pressure derivative.¹

The volume and bulk modulus of the phase at reference pressure and elevated temperature are frequently evaluated by semi-empirical functions. For the T -dependence of volume and the thermal expansivity α , EoS uses

$$V(P_0, T) = V_0 e^{\int_{T_0}^T \alpha(T) dT}, \quad (2.12)$$

$$\alpha(T) = \sum_j a_j T^{p_j}, \quad (2.13)$$

¹Throughout the presentation of models, we use the notation ∂_X to denote a partial derivative with respect to X and we apply the convention that differential operators take precedence over the reference state indicator, i.e., $\partial_{P,T} K_0 = (\partial_P \partial_T K)(P_0, T_0)$ represents the P - T -cross derivative of the isothermal bulk modulus, evaluated at the reference point (P_0, T_0) .

which is, e.g., compatible with the formulation by [Fabrichnaya et al. \[2004\]](#):

$$\alpha(T) = a_1 + a_2T + a_3T^{-1} + a_4T^{-2}. \quad (2.14)$$

The isothermal bulk modulus K of the phase is described as a linear or polynomial function of T . In this case, the formulation in EoS accounts for the direct T -dependence of K and $\partial_P K$ and an implicit entropy dependence of $\partial_P K$ [[Poirier, 2000](#)]:

$$K(T) = K_0 + \partial_T K_0(T - T_0), \quad (2.15)$$

$$\partial_P K(T) = \partial_P K_0 + \partial_{P,T} K_0(T - T_0)(\ln T - \ln T_0), \quad (2.16)$$

which is, e.g., compatible with the parameterization used by [Piazzoni et al. \[2007\]](#) or [Matas \[1999\]](#).

Alternatively, K at P_0 is expressed in terms of isothermal compressibility β :

$$K(T) = \frac{1}{\beta(T)}, \quad (2.17)$$

$$\beta(T) = \sum_k b_k T^{pk}, \quad (2.18)$$

which is, in turn, compatible with the parameterization used by [Fabrichnaya et al. \[2004\]](#).

While the polynomial approximations of C_P and K can produce very accurate results in the T -range of calibration, they extrapolate poorly and their functional form does not guarantee physically sensible behavior under extreme conditions.

Any other thermodynamic property of a particular phase is obtained by differentiating the leading potential function and using standard thermodynamic identities. Entropy of the phase, for example, is calculated as follows:

$$S(P, T) = -\partial_T G(P, T) \quad (2.19)$$

$$= S(P_0, T) + T\partial_T S(P_0, T) - \partial_T [H(P_0, T)]_{T_0}^T - \partial_T [G(P, T)]_{P_0}^P$$

$$= S(P_0, T) + T\partial_T S(P_0, T) - C_P(T) - \int_{P_0}^P \partial_T V(P, T) dP$$

$$= S_0 + \int_{T_0}^T \frac{C_P(T)}{T} dT - \int_{P_0}^P \alpha(T) V(P, T) dP. \quad (2.20)$$

Density can be computed directly through its relationship to V :

$$\rho(P, T) = \frac{M}{V(P, T)}, \quad (2.21)$$

where M is the molar mass of the phase of interest.

Compressibility can (also) be expressed as

$$\beta(P, T) = -\frac{1}{V(P, T)} \partial_P V(P, T) = (K(T) + \partial_P K(T)P)^{-1} \quad (2.22)$$

for the second order equation-of-state introduced in Equation (2.11).

2.2 The Caloric-Modified-Tait Model

This model is conceptually similar to the Caloric-Murnaghan model, but employs a different P - V equation-of-state [Holland and Powell, 2011, Holland et al., 2013]. For an overview of the dataflow see Figure 2.3.

In analogy to the Caloric-Murnaghan model, Gibbs energy is computed by T -integration over C_P at P_0 and P -integration over V at elevated T to obtain Gibbs energy (Equations (2.6), (2.7) and (2.10)). To obtain $V(P, T)$, the modified Tait equation is used in Holland and Powell [2011]:

$$V(P, T) = V_0(1 - a(1 - (1 + b(P - P_{\text{th}}(T))))^{-c}), \quad (2.23)$$

where P_{th} is thermal pressure and a, b, c depend on compressibility parameters:

$$a = \frac{1 + \partial_P K_0}{1 + \partial_P K_0 + K_0 \partial_P^2 K_0}, \quad (2.24)$$

$$b = \frac{\partial_P K_0}{K_0} - \frac{\partial_P^2 K_0}{1 + \partial_P K_0}, \quad (2.25)$$

$$c = \frac{1 + \partial_P K_0 + K_0 \partial_P^2 K_0}{\partial_P K_0^2 + \partial_P K_0 - K_0 \partial_P^2 K_0}. \quad (2.26)$$

Substituting Equation (2.23) into (2.10) yields

$$[G(P, T)]_{P_0}^P = PV_0 \left(1 - a + a \frac{(1 - bP_{\text{th}}(T))^{1-c} - (1 + b(P - P_{\text{th}}(T)))^{1-c}}{b(c-1)P} \right). \quad (2.27)$$

The thermal pressure used by Holland and Powell [2011] is inspired by the Einstein lattice vibration model and includes an approximate Einstein temperature θ_E :

$$P_{\text{th}}(T) = \alpha_0 K_0 \frac{\theta_E}{\xi(T_0)} \left(\frac{1}{e^{\frac{\theta_E}{T}} - 1} - \frac{1}{e^{\frac{\theta_E}{T_0}} - 1} \right), \quad (2.28)$$

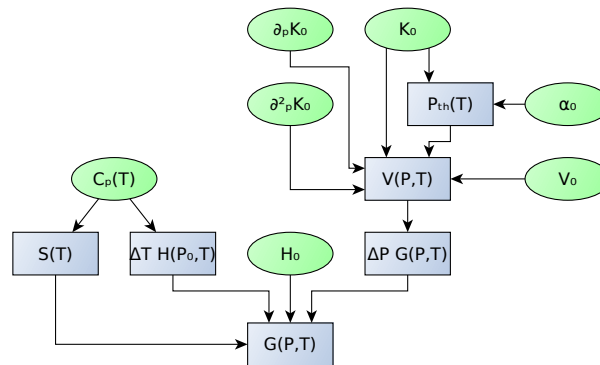


Figure 2.3: Data flow in the Caloric-Modified-Tait model for the computation of Gibbs energy used by Holland et al. [2013]. Gibbs energy G is assembled from an elastic part $\Delta P G(P, T) = [G(P, T)]_{P_0}^P$, following the Tait formalism, and a thermal part $\Delta T H(P, T) = [H(P, T)]_{T_0}^T$, based on a polynomial representation of the heat capacity. Model parameters (taken from a database of phases at runtime) are enclosed in ellipses and shaded green while the computational steps of the model code are represented by rectangular boxes shaded blue; model parameters that are functions of T are polynomials in T . Abbreviations for physical parameters used in the flow chart are listed in Table B.1.

with

$$\xi(T) = \frac{\left(\frac{\theta_E}{T}\right)^2 e^{\frac{\theta_E}{T}}}{\left(e^{\frac{\theta_E}{T}} - 1\right)^2}, \quad (2.29)$$

$$\theta_E = \frac{10636.0 \text{ K}}{\frac{S_0}{N \text{ Jmol}^{-1} \text{ K}^{-1}} + 6.44}. \quad (2.30)$$

The Einstein temperature θ_E depends on the entropy of the reference state S_0 and the number of atoms per formula unit N .

By differentiating $V(P, T)$ (Equation (2.23)) we obtain α and β of a phase:

$$\alpha(P, T) = \frac{\alpha_0 K_0 \theta_E}{\xi(T_0)} \cdot \frac{abc(1 + b(P - P_{\text{th}}(T)))^{-c-1} e^{\frac{\theta_E}{T}} \frac{\theta_E}{T^2}}{(1 - a(1 - (1 + b(P - P_{\text{th}}(T)))^{-c})) \left(e^{\frac{\theta_E}{T}} - 1\right)^2}, \quad (2.31)$$

$$\beta(P, T) = \frac{1}{K_0} \cdot \left((1 + b(P - P_{\text{th}}))(a + (1 - a)(1 + b(P - P_{\text{th}}))^c)\right)^{-1}. \quad (2.32)$$

Any other thermodynamic property is obtained by differentiation of the Gibbs potential at P, T and by application of thermodynamic identities as illustrated in Equation (2.20) for entropy.

2.3 The Birch-Murnaghan-Mie-Debye-Grüneisen Model

Here, the thermodynamic potential is computed along an integration path that combines isothermal compression at T_0 up to the elastic pressure P_{el} , followed by isochoric heating to the P and T of interest (Figure 2.1). The model formulation is based on [Stixrude and Lithgow-Bertelloni \[2005b, 2011\]](#) and is compatible with data sets in these publications. For an overview of the dataflow see Figure 2.4.

The expression for Gibbs energy of a phase at elevated T and P consists of individual contributions to Helmholtz energy A and a conversion term accounting for the change of conditions from constant- V to constant- P :

$$G(P, T) = A_0 - [A(f, T_0)]_{f(V_0)}^{f(V)} - [A(f_1, T)]_{T_0}^T + P V(P, T), \quad (f_1 = f(P, T)). \quad (2.33)$$

The Birch-Murnaghan equation-of-state [[Birch, 1947](#)] is applied to expand P_{el} and V as polynomials in the finite strain parameter f :

$$f(V) = \frac{1}{2} \left(\left(\frac{V}{V_0} \right)^{-\frac{2}{3}} - 1 \right) \iff V(f) = V_0 (2f + 1)^{-\frac{3}{2}}, \quad (2.34)$$

$$P(f, T) = P_{\text{el}}(f) + P_{\text{th}}(f, T), \quad (2.35)$$

$$P_{\text{el}}(f) = 3K_0 (2f + 1)^{\frac{5}{2}} \left(f + \frac{3}{2} (\partial_P K_0 - 4) f^2 \right). \quad (2.36)$$

To obtain $f(P, T)$ and consequently $V(f(P, T))$, the model implementation in EOS inverts Equation (2.35) numerically for f at constant T . Once f is determined, the

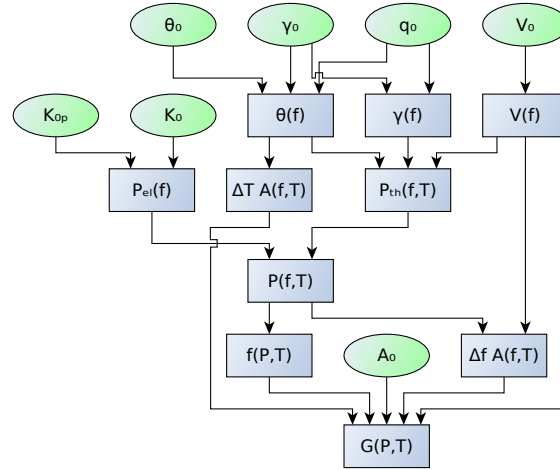


Figure 2.4: Data flow in the Birch-Murnaghan-Mie-Debye-Grüneisen model for the computation of Gibbs energy used by [Stixrude and Lithgow-Bertelloni \[2011\]](#). Gibbs energy G is assembled from an elastic part $\Delta f A(f, T) = [A(f, T)]_{f(V_0)}^{f(V)}$, following the Birch-Murnaghan formalism, and a thermal part $\Delta T A(f, T) = [A(f, T)]_{T_0}^T$, based on the Debye model. Model parameters (taken from a database of phases at runtime) are enclosed in ellipses and shaded green while the computational steps of the model code are represented by rectangular boxes shaded blue. Abbreviations for physical parameters used in the flow chart are listed in Table B.1.

isothermal contribution to Helmholtz energy can be computed as

$$[A(f, T_0)]_{f(V_0)}^{f(V)} = \int_{V_0}^{V(f)} P(f(V), T_0) dV \quad (2.37)$$

$$= \int_{f(V_0)}^f P_{el}(f) \partial_f V(f) df \quad (2.38)$$

$$= -\frac{9}{2} K_0 V_0 (f^2 + (\partial_P K_0 - 4) f^3). \quad (2.39)$$

Thermal effects, on the other hand, are derived from a lattice vibration model based on [Debye \[1912\]](#), from which expressions for the thermal contribution to Helmholtz energy $[A(f, T)]_{T_0}^T$, thermal pressure P_{th} and entropy S can be derived [[Poirier, 2000](#)]. These can be transformed from constant- V to constant- P conditions

[Ita and Stixrude, 1992, Stixrude and Lithgow-Bertelloni, 2005b, 2011]:

$$[A(f, T)]_{T_0}^T = \int_{T_0}^T S(V(f), T) dT \quad (2.40)$$

$$= -NR \left[T \left(3 \ln(1 - e^{-x(f, T)}) + \frac{9}{8} x(f, T) - D_3(x(f, T)) \right) \right]_{T_0}^T, \quad (2.41)$$

$$P_{\text{th}}(f, T) = 3NR [TD_3(x(f, T))]_{T_0}^T \frac{\gamma(f)}{V(f)}, \quad (2.42)$$

$$S(P, T) = 4NRD_3(x(f(P, T), T)) - 3NR \ln(1 - e^{-x(f(P, T), T)}) + \int_0^T V(P, T) \frac{\alpha(P, T)^2}{\beta(P, T)} dT, \quad (2.43)$$

with

$$\theta_D(f) = \theta_{D,0} \sqrt{1 + 6\gamma_0 f + \frac{1}{2} g_0 f^2}, \quad (2.44)$$

$$x(f, T) = \frac{\theta_D(f)}{T}, \quad (2.45)$$

$$\gamma(f) = \frac{(6\gamma_0 + g_0 f)(2f + 1)}{6 + 36\gamma_0 f + 3g_0 f^2}, \quad (2.46)$$

$$g_0 = 36\gamma_0^2 - 12\gamma_0 - 18q_0\gamma_0, \quad (2.47)$$

where θ_D is the Debye temperature, γ the Grüneisen parameter and $q := \frac{d\gamma}{d \log V}$.

The integral in Equation (2.40) is replaced using the third-order Debye function, which appears in Equations (2.41) – (2.43):

$$D_3(x) = \frac{3}{x^3} \int_0^x \frac{t^3}{e^t - 1} dt. \quad (2.48)$$

For the numerical approximation used to evaluate the Debye integral in (2.48) see Section 3.3.

Similarly, C_P can be derived from S by differentiating Equation (2.43):

$$C_P(P, T) = T \partial_T S(P, T) \quad (2.49)$$

$$\begin{aligned} &= C_V(f(P, T), T) + V(P, T) T \frac{\alpha(P, T)^2}{\beta(P, T)} \\ &= 3NR \left(4D_3(x(f(P, T), T)) - \frac{3x(f(P, T), T)}{e^{x(f(P, T), T)} - 1} \right) \\ &+ V(P, T) T \frac{\alpha(P, T)^2}{\beta(P, T)}. \end{aligned} \quad (2.50)$$

For the isochoric heat capacity C_V , the model shows the following behavior in the high- T limit:

$$\lim_{T \rightarrow \infty} x(f(P, T), T) = 0, \quad (2.51)$$

$$\lim_{x \rightarrow 0} D_3(x) = 1, \quad (2.52)$$

$$e^x - 1 \approx x \quad (x \ll 1) \quad (2.53)$$

$$\implies \lim_{T \rightarrow \infty} C_V(P, T) = 3NR, \quad (2.54)$$

consistent with the law of Dulong-Petit. On the other hand, as T approaches zero one obtains

$$\lim_{T \rightarrow 0} x(f(P, T), T) = \infty, \quad (2.55)$$

$$\lim_{x \rightarrow \infty} D_3(x) = 0 \quad (2.56)$$

$$\implies \lim_{T \rightarrow 0} C_V(P, T) = 0, \quad (2.57)$$

in agreement with the third law of thermodynamics. The high- and low- T limits guarantee that the model behaves in a physically sensible way at any T , even when extrapolating beyond the conditions for which model parameters have originally been fitted.

Derivative volumetric properties can be computed using standard thermodynamic relationships:

$$\alpha(P, T) = \frac{1}{V(P, T)} \partial_T V(P, T), \quad (2.58)$$

$$\beta(P, T) = -\frac{1}{V(P, T)} \partial_P V(P, T). \quad (2.59)$$

Finally, the adiabatic bulk modulus κ can be derived from the Gibbs potential:

$$\begin{aligned} \kappa(f, T) &= \frac{\partial_P G}{\frac{(\partial_{T,P} G)^2}{\partial_T^2 G} - \partial_P^2 G} \quad (2.60) \\ &= (2f + 1)^{5/2} K_0 \\ &\quad \cdot \left(1 + \left((3\partial_P K_0 - 5)f + \frac{27}{2}(\partial_P K_0 - 4)f^2 \right) \right) \\ &\quad + \frac{\gamma(f)(\gamma(f) + 1 - q(f))}{V(f)} [E(f, T)]_{T_0}^T \\ &\quad - \frac{\gamma(f)^2}{V(f)} [TC_V(f, T)]_{T_0}^T, \quad (2.61) \end{aligned}$$

with

$$[E(f, T)]_{T_0}^T = 3NR[TD_3(x)]_{T_0}^T, \quad (2.62)$$

$$q(f) = 2 \left(\gamma(f) - \frac{1}{3} \right) - \frac{g_0(2f + 1)}{3(6\gamma_0 + g_0f)}, \quad (2.63)$$

where $[E(f, T)]_{T_0}^T$ represents the thermal internal energy derived from the Debye model [Ashcroft and Mermin, 1976].

2.4 Shear Modulus

A shear modulus μ can be formulated consistently with the Birch-Murnaghan–Mie-Debye-Grüneisen model [Stixrude and Lithgow-Bertelloni, 2005b], although the thermodynamic theory of the model does not provide information about shear deformation directly, as it accounts for isotropic deformation only. The computation of μ requires some additional model parameters:

$$\begin{aligned} \mu(f, T) = & (2f + 1)^{5/2} \mu_0 \\ & + (2f + 1)^{5/2} f (3K_0 \mu_{P,0} - 5\mu_0) \\ & + (2f + 1)^{5/2} f^2 \left(6K_0 \mu_{P,0} - 24K_0 - 14\mu_0 + \frac{9}{2} K_0 \partial_P K_0 \right) \\ & - \eta_S \frac{[E(f, T)]_{T_0}^T}{V(f)}, \end{aligned} \quad (2.64)$$

The shear modulus at reference condition is μ_0 and its pressure derivative $\mu_{P,0}$. The shear strain derivative η_S of the Grüneisen parameter γ has to be estimated independently.

2.5 Order-Disorder Transition

Thermodynamic properties of minerals with a second-order phase transition or with changes in element ordering between multiple crystallographic sites can be treated with the Landau tricritical theory [e.g., Carpenter et al., 1994, Holland and Powell, 1998]. There, standard thermodynamic properties refer to a completely disordered phase (G_{dis}) and a Landau contribution G_L , which accounts for progressive ordering with decreasing T , is added to obtain a value for the partially ordered phase (G_{ord}):

$$G_{\text{ord}}(P, T) = G_{\text{dis}}(P, T) + G_L(P, T). \quad (2.65)$$

The Landau ordering contribution is applied at temperature below the order-disorder transition $T_C(P)$, defined by the transition temperature at reference pressure $T_{C,0}$ and the Clapeyron slope of the phase transition boundary as:

$$T_C(P) = T_{C,0} + \frac{V_{L,\text{max}}}{S_{L,\text{max}}} P, \quad (2.66)$$

where $V_{L,\text{max}}$ is the maximum volume of disorder and $S_{L,\text{max}}$ is the maximum entropy of disorder. At $T < T_C(P)$, the magnitude of ordering is defined by the order parameter Q :

$$Q(P, T) = \sqrt[4]{1 - \frac{T}{T_C(P)}}, \quad (2.67)$$

which leads to

$$G_L(P, T) = S_{L,\text{max}} \left((T - T_C(P)) Q(P, T)^2 + \frac{1}{3} T_{C,0} Q(P, T)^6 \right). \quad (2.68)$$

The magnitude of the Landau contribution to all thermodynamic properties decreases as Q decreases with increasing temperature; at $T = T_C(P)$, $Q = 0$ and G_L vanishes. It is set to zero at $T > T_C(P)$.

Representative thermodynamic properties of the partially ordered phase are obtained by differentiating of Gibbs potential from Equation (2.65):

$$\begin{aligned} V_{\text{ord}}(P, T) &= \partial_P G(P, T) \\ &= V_{\text{dis}}(P, T) \end{aligned} \quad (2.69)$$

$$- V_{L,\text{max}} Q(P, T)^2 \left(1 + \frac{1}{2} \frac{T}{T_C(P)} \left(1 - \frac{T_{C,0}}{T_C(P)} \right) \right), \quad (2.70)$$

$$\begin{aligned} S_{\text{ord}}(P, T) &= -\partial_T G(P, T) \\ &= S_{\text{dis}}(P, T) \end{aligned} \quad (2.71)$$

$$- S_{L,\text{max}} Q(P, T)^2 \left(1 - \frac{1}{2} \left(1 - \frac{T_{C,0}}{T_C(P)} \right) \right), \quad (2.72)$$

$$\begin{aligned} C_{P,\text{ord}}(P, T) &= -T \partial_T^2 G(P, T) \\ &= C_{P,\text{dis}}(P, T) \end{aligned} \quad (2.73)$$

$$- \frac{1}{2} S_{L,\text{max}} Q(P, T)^{-2} \frac{T}{T_C(P)} \left(1 - \frac{1}{2} \left(1 - \frac{T_{C,0}}{T_C(P)} \right) \right). \quad (2.74)$$

The Landau model of ordering can generally be applied to any thermodynamic model for pure phases. In the database by [Stixrude and Lithgow-Bertelloni \[2011\]](#) that is distributed with EoS, the Landau model is combined with the Birch-Murnaghan-Mie-Debye-Grüneisen equation-of-state.

2.6 Solution Phases

The thermodynamic properties of solution phases consist of a linear combination of endmember properties (mixture), configurational (ideal) and excess (non-ideal) mixing contributions [e.g., [Ganguly, 2008](#), [Hillert and Staffansson, 1970](#)]:

$$G = \sum_i x_i G_i - T S_{\text{cf}} + G_{\text{ex}}, \quad (2.75)$$

$$S = \sum_i x_i S_i + S_{\text{cf}}, \quad (2.76)$$

where i indexes the solution endmembers; G_i and S_i are the standard Gibbs energy and entropy of the i -th endmember, S_{cf} represents the configurational entropy of the solution and G_{ex} is the excess Gibbs energy of mixing. For solutions with linearly independent endmembers, mole fractions are uniquely defined by the bulk solution composition. All solutions treated here are expressed in the linearly independent composition space.

The configurational entropy in the Bragg-Williams approximation is assumed to be statistically random, with mixing of elements or element groups on one or more independent sites that correspond to specific positions in the crystal lattice [[Ganguly,](#)

2008, Hillert and Staffansson, 1970]. The entropy contributions from the individual mixing sites are mutually independent and additive, leading to:

$$S_{\text{cf}} = -R \sum_{s,k} m_s x_{s,k} \ln x_{s,k}, \quad (2.77)$$

where m_s represents the multiplicity of site s and $x_{s,k}$ is the mole fraction of constituent k on site s . The fractions $x_{s,k}$ in Equation (2.77) can be determined from the endmember mole fractions x_i in Equation (2.75) and the site occupancy $N_{i,s,k}$ in formula units of the endmembers:

$$x_{s,k} = \frac{\sum_i N_{i,s,k} x_i}{\sum_{i,k} N_{i,s,k} x_i}, \quad (2.78)$$

for any site s and constituent k .

The excess contribution to Gibbs energy of solution has been conventionally expressed by polynomial expansions in terms of endmember or constituent mole fractions [e.g., Helffrich and Wood, 1989, Muggianu et al., 1975, Mukhopadhyay et al., 1993], which incorporate several composition schemes for expansion into multicomponent space [Pelton, 2001, Toop, 1965]. For geological applications, the Kohler-Toop scheme has been widely accepted.

The most basic approach is a binary symmetric interaction model; with equal number of atoms of the endmembers and negligible differences in ion sizes, the excess energy can be written as

$$G_{\text{ex}}^{(\text{binary})} = \sum_{i<j} x_i x_j W_{i,j}, \quad (2.79)$$

where $W_{i,j}$ is the binary interaction energy between the endmembers i and j . EOS adopts the slightly more complex asymmetric van Laar formulation [Holland and Powell, 2003, Powell, 1974, Stixrude and Lithgow-Bertelloni, 2011], which expands upon the simple two-component case by transforming binary interaction energies into multicomponent space, taking the number of atoms per formula unit of each endmember into account and adding the concept of size parameters:

$$G_{\text{ex}} = \sum_{i<j} \underbrace{\frac{(x_i d_i N_i)(x_j d_j N_j)}{(\sum_k x_k d_k N_k)^2}}_{=:Y_{i,j}} \cdot 2 \cdot \underbrace{\frac{\sum_k x_k d_k}{d_i + d_j}}_{=:B_{i,j}} \cdot W_{i,j}, \quad (2.80)$$

where d_i represents a non-dimensional size parameter for the solution component i and the number of atoms per formula unit N_i of endmember i ; k ranges over the solution endmembers.

The renormalized interaction energy $B_{i,j}$ in Equation (2.80) reduces to $W_{i,j}$ when all size parameters are identical ($d_i = d_j$ for all i, j). This corresponds to the symmetric, regular Margules model, consistent with the energy change due to nearest neighbor energetic interactions [e.g., Stixrude and Lithgow-Bertelloni, 2011]. The renormalized product of constituent fractions $Y_{i,j}$ in Equation (2.80) reduces to $x_i x_j$ when

all size parameters are the same and all solution endmembers have the same number of atoms in a formula unit ($N_i = N_j$ for all i, j). With $Y_{i,j} = x_i x_j$ and $B_{i,j} = W_{i,j}$, Equation (2.80) reduces to Equation (2.79) for a binary solution.

Intensive material properties of the solution are evaluated as weighted averages of the endmember properties. For example, the molar mass and molar volume of the solution are computed as

$$M = \sum_i x_i M_i, \quad (2.81)$$

$$V = \sum_i x_i V_i. \quad (2.82)$$

Densities and volume derivatives are then found as:

$$\rho = \frac{M}{V}, \quad (2.83)$$

$$\alpha = \frac{\sum_i x_i V_i \alpha_i}{V}, \quad (2.84)$$

$$\beta = \frac{\sum_i x_i V_i \beta_i}{V}. \quad (2.85)$$

An excess volume contribution would have to be added to Equation (2.82) in case of P -dependent interaction energies in Equation (2.80).

The elastic moduli of the solution are computed as Voigt-Reuss-Hill averages of the endmember properties [Hill, 1963]. Given that the endmembers mix on the atomic level and do not act as separate elastic resistors, we weight the modulus averages by mole fractions, consistent with other intensive properties:

$$\kappa = \frac{1}{2} \left(\frac{\sum_i x_i V_i \kappa_i}{V} + \left(\frac{\sum_i x_i V_i \kappa_i^{-1}}{V} \right)^{-1} \right), \quad (2.86)$$

where κ_i is the adiabatic bulk modulus of constituent i . An equivalent expression is applied to the calculation of the shear modulus.

2.7 Multiphase Aggregates

Thermodynamic and other properties of mineral assemblages or multiphase aggregates are computed as linear combinations weighted by *mole amounts* of their constituents, which follows naturally for extensive properties, or by *volume fractions*, which applies to elastic properties that depend on the space occupied by different constituents. This leads to a similar mathematical structure as that used for the computation of solution properties. However, the weighting factors for solutions are generally *mole fractions* and no additional configurational entropy and excess energy terms apply to multiphase aggregates. The mass and volume of the multiphase

aggregate, expressed as extensive properties, become:

$$M_{\text{tot}} = \sum_i X_i M_i, \quad (2.87)$$

$$V_{\text{tot}} = \sum_i X_i V_i, \quad (2.88)$$

and consequently

$$\rho = \frac{M_{\text{tot}}}{V_{\text{tot}}}, \quad (2.89)$$

where i ranges over the phases in the aggregate, X_i is the mole amount, M_i the mass, and V_i the volume of constituent i .

Elastic moduli of the multiphase aggregate are computed as Voigt-Reuss-Hill averages of the single-phase properties [Hill, 1963]. However, the moduli of individual phases are weighted by *volume fractions* rather than *mole fractions* to account for the distribution of pressure over potentially different types of mineral grains exhibiting different surface areas:

$$\kappa = \frac{1}{2} \left(\frac{\sum_i X_i V_i \kappa_i}{V_{\text{tot}}} + \left(\frac{\sum_i X_i V_i \kappa_i^{-1}}{V_{\text{tot}}} \right)^{-1} \right), \quad (2.90)$$

where κ_i is the adiabatic bulk modulus of the i -th constituent. We use an equivalent expression for the calculation of the aggregate shear modulus.

Chapter 3

Software Implementation

EOS is a software package that performs calculations of phase equilibria and associated material properties, individually or for a multiphase aggregate. This scope of functionality is similar to other multicomponent Gibbs energy minimizers such as PERPLE_X [Connolly, 2005], THERIAK [de Capitani and Petrakakis, 2010] or HEPHESTO [Stixrude and Lithgow-Bertelloni, 2005b, 2011]. We have built EOS in a modular way to make it easily extendable to various equation-of-state formulations or more complex mixing models. In contrast to many of the other software packages, EOS is distributed freely, both as source code and in executable form. The code can be found on the accompanying optical disc or accessed and downloaded from the project website (<https://bitbucket.org/chust/eos>), where extensive documentation and examples are included. In particular, material that allows for a direct reproduction of all Figures presented in this work is provided.

The central task of a phase equilibrium computation is the solution to the optimization problem defined by minimizing Gibbs energy of a multiphase assemblage, whose identity is not known *a-priori*. The total Gibbs energy of all candidate phases forms a linear objective function that is minimized. We use the LP_SOLVE library (<http://lpsolve.sourceforge.net/5.5>) to solve this algebraic problem. The library has been embedded in the EOS package and customized for safe memory management.

The optimization process implemented in EOS consists of three steps:

- (i). the Gibbs energies of all candidate phases are computed using their equations-of-state; solid solutions are represented by one or more candidates with constant composition. This step uses thermodynamic parameters from a configurable database file;
- (ii). linear optimization selects a set of phases with minimal Gibbs energy, subject to the constraint of bulk composition. The number of phases corresponds to the number of system components, as required by the phase rule for two degrees of freedom (P, T);
- (iii). non-linear optimization attempts to improve the solution compositions.

Steps (i) through (iii) are repeated until no further improvement for the current phase assemblage and its composition can be found. After a stable phase assem-

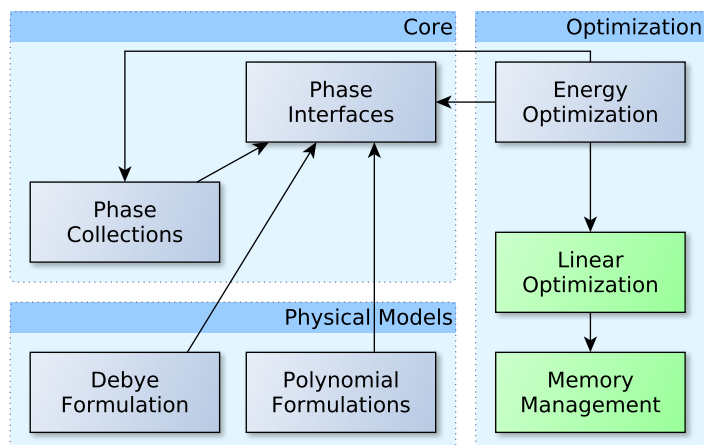


Figure 3.1: Module structure of the EoS software library. The diagram shows functional units as boxes and direct dependencies as arrows. Blue boxes represent functionality implemented in the F# language, while green boxes represent code written in the programming language C.

blage has been determined, aggregate material properties may be computed, which in turn rely on single-phase properties.

The implementation of EoS contains three main areas of functionality (Figure 3.1):

- (i). the core of EoS implements the basic infrastructure to manage a collection of phases, provides uniform access to all kinds of phases and offers generic implementations of functionality applicable to any physical model;
- (ii). the thermodynamic models described in Chapter 2 are implemented as independent modules, but with common, uniform interfaces as defined by the core;
- (iii). the Gibbs energy optimizer forms a separate module that extends collections of phases with functionality to compute a stable assemblage.

3.1 Code Design

All thermodynamic state functions can be derived by differentiating the thermodynamic potential, thus most material properties have closed analytical and self-consistent expressions. This facilitates modular implementation, as the thermodynamic model is an implementation detail that is required to compute values of the desired properties, but the nature of their independent and dependent variables, their general functional form and set of possible computations are known *a-priori*, from general thermodynamic identities. It has the advantage that common capabilities of different implementations are controlled by the same commands, making EoS extensible to additional models without the need to change existing interface or code assembly. In EoS we have clearly separated interfaces and model implementations, following the structure of the thermodynamic equations (Figure 3.2).

The principal advantage of such an approach is that little knowledge of the physical model is required from the user in order to compute individual properties. For

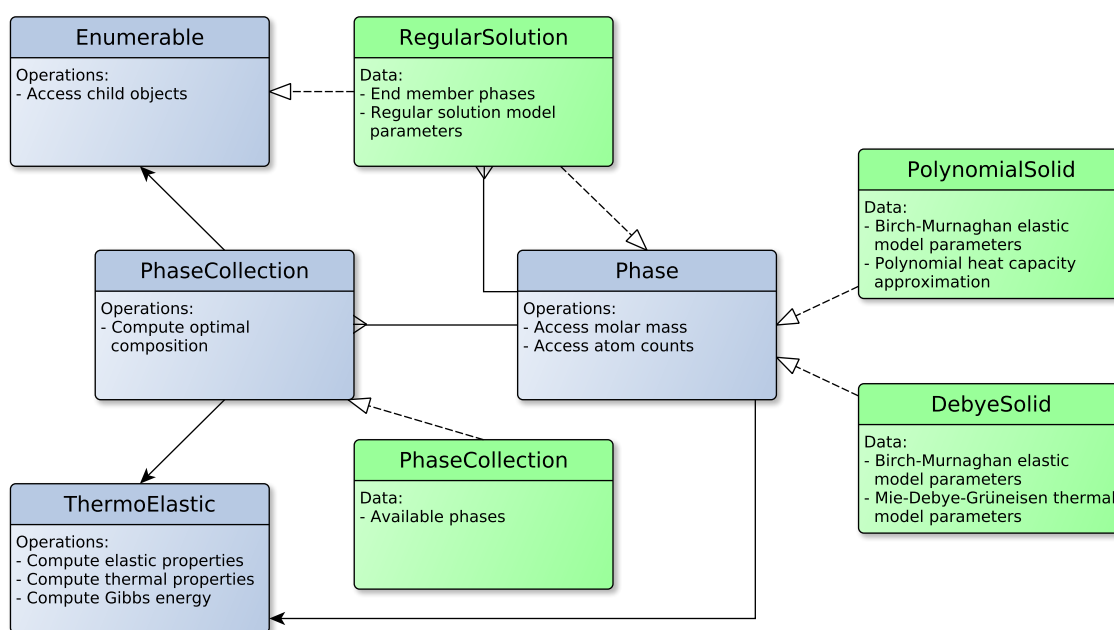


Figure 3.2: Interface structure of the EOS software library. The diagram shows programming interfaces and their relations: Boxes with blue background represent interfaces to common functionality while boxes with green background represent implementations of these interfaces. Solid arrows link interfaces to “parents”, i.e., more general interfaces whose functionality is implied by the more specific ones. Dashed arrows link implementations to their supported interfaces. Solid lines with an arrow head at the start represent aggregation relationships.

example, density is computed the same way for any object, whether it is a single stoichiometric phase, a solution or a polycrystalline aggregate. The operations that compute thermoelastic properties can all be accessed through the ThermoElastic interface. Most of its methods take three arguments representing pressure, temperature and composition. The composition argument may be left unspecified for single stoichiometric phases but is used to specify relative amounts of endmembers in a solution or total amounts of phases in an aggregate.

The ThermoElastic interface is extended by Phase and PhaseCollection, which provide access to the chemical composition information of a phase and to the optimizer functionality, respectively. A PhaseCollection also acts as a container of Phase objects that can be iterated over and indexed. The different equations-of-state implemented in EOS are all accessed through the Phase interface. Instances of the RegularSolution model act as containers of their endmember Phase objects similar to the way a PhaseCollection provides access to its constituents.

3.2 Language Choice

The EOS software package is largely implemented in the programming language F# (<http://fsharp.org/>). The type system of F# specifies physical units of quantities manipulated within the program, offering the guarantee that the code will compile free of unit errors. The code generated by the compiler runs on the CLR virtual ma-

chine (<https://docs.microsoft.com/en-us/dotnet/standard/clr>) with automatic memory management and is portable to different operating systems (<http://www.mono-project.com/>). The language F# can be used as an interpreter, so programming interfaces offered by EoS can easily be scripted or used interactively for small calculations. At the same time, EoS includes a set of command line programs that handle common computation tasks, as documented in the distribution of the code.

Some performance critical parts of EoS are implemented using C code: The library `LP_SOLVE` benefits from architecture-specific optimizations of arithmetic code, and certain interfaces to native system functionality – like MPI – require interaction with platform specific code in any case.

We have implemented a number of unit tests in EoS to verify its functionality, internal consistency and physically sensible behavior of its components. For each thermodynamic model implemented, the tests check, for instance, that the molar volume of a substance decreases with pressure, and verifies that fundamental thermodynamic identities such as $V = \partial_P G$ hold numerically. The automated tests also include comparisons of key parameters to experimental data. However, no quantitative assessment of the results and their accuracy is performed.

3.3 Numerical Details

Non-analytical solutions to the equations-of-state are found numerically in the EoS software. The code uses interval bisection, which allows error estimation and refinement of the result to high accuracy. The initial interval (minimum and maximum value) is prescribed to cover a wide range of physically sensible volumes.

The computation of some thermodynamic state functions, e.g., $V(P, T) = \partial_P G(P, T)$ and $S(P, T) = -\partial_T G(P, T)$, is performed numerically when non-analytical expressions are involved. We perform numerical differentiation using an adaptive scheme that combines a second-order approximation with higher orders to obtain both a value of the derivative and an error estimate. For two-sided derivatives we combine second- and fourth-order schemes, for one-sided derivatives (for instance, at the lower temperature limit) we combine second- and third-order schemes. The step length in numerical differentiation is reduced exponentially until a desired accuracy has been achieved or a minimum step length to prevent rounding errors has been reached. In general, the desired accuracy is at least two orders of magnitude lower than the derivative value. For the numerical differentiation of G by P to obtain V , the desired accuracy is set to $10^{-8} \text{ m}^3 \text{ mol}^{-1}$ and the minimum step length to 10^5 Pa , for example.

Approximations to the Debye integral are calculated using Chebyshev polynomials and half-analytical expressions that depend on the magnitude of the argument $x = \theta_D/T$ in Equation (2.45). Other numerically evaluated integrals are computed with an adaptive Gauss-Kronrod scheme, which combines seven- and fifteen-point quadrature rules in order to obtain the integral value and its error estimate simultaneously. The integration interval is progressively split such that the error estimate for each segment becomes lower than a desired threshold, with a lower limit on the segment length set to restrict the effect of rounding errors. The maximum and minimum

step length are estimated as

$$\Delta x_{\max} = \frac{x_{\max} - x_{\min}}{2} \quad (3.1)$$

and

$$\Delta x_{\min} = \sqrt{\frac{\Delta I}{\Delta x_{\max}}} \Delta x_{\max}, \quad (3.2)$$

where x_{\max} and x_{\min} are the integration boundaries and ΔI is the desired maximum error per segment. For example, we use the maximum error per segment $\Delta I = 1 \text{ J mol}^{-1}$ when integrating Equation (2.10).

The search for the equilibrium phase assemblage is treated as an optimization problem in EoS. The Gibbs energy of the system consisting of all candidate phases forms a linear objective function,

$$G = \sum_i^{\text{phases}} (n_i G_i), \quad (3.3)$$

where n_i is the (positive) number of moles of phase i . At given P and T , the phase rule requires that the number of phases that have non-zero amounts corresponds to the number of system components. The objective function is minimized with one free variable (n_i) at a time, subject to bulk composition constraints. The mass balance for each chemical component of the system provides a constraint that can be represented as an equality or inequality relation. In the latter case, the phase set hosts smaller amounts of the chemical component than available, and this situation arises where part of the composition space is not covered by any phase.

Our implementation uses a bundled version of the LP_SOLVE library to optimize the objective function, i.e., the total Gibbs energy of a phase assemblage, under mass-balance constraints. The algorithm scales the linear optimization problem to numerically convenient value ranges, which makes the solution independent of any multipliers in mass-balance constraints, i.e., independent of the choice of the chemical formula size (e.g., MgSiO_3 and $\text{Mg}_4\text{Si}_4\text{O}_{12}$ are equivalent). Combinations of phases that can represent the bulk composition are selected, and the energetically most favorable set is determined. Simultaneously, EoS locates the optimal composition of solution phases as a non-linear optimization problem. The initial selection uses the endmembers of the solid solutions and, in a non-linear optimization task, the solution composition is modified with the steepest-descent method. The composition space of the solid solution is discretized into hypothetical intermediate phases (pseudocompounds), and their compositions are modified until a local minimum is attained. The new candidates are added to the list of plausible phases before a new iteration step of the linear optimization is performed. The size of composition steps for the steepest-descent method search can be adapted, the default value is 0.4 mol%.

The LP_SOLVE library employs the simplex method to find a minimum on the Gibbs energy hyperplane, iterating through the nodes of the polytope consisting of all vectors of modal phase amounts satisfying the linear inequalities representing mass balance of chemical components. Each such node corresponds to a feasible, but

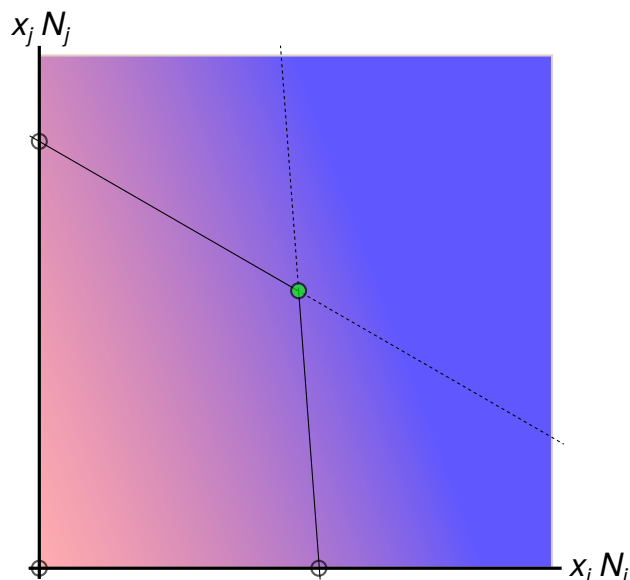


Figure 3.3: Conceptual example of the simplex optimization algorithm in two dimensions. Coordinates are the amounts of candidate phases and lines represent constraints on the molar amounts. The axes themselves represent the constraint of non-negative molar amounts of bulk chemical constituents, while the other lines represent the constraints of bulk composition. Any assemblage that exactly matches the bulk composition will lie on one of those lines and any assemblage using some part of the bulk composition will lie within the polygon (or polytope in higher dimensions) spanned by the constraint lines (or hyperplanes in higher dimensions). In the illustration, Gibbs energy is a linear function represented by the background color (energy values decreasing towards the blue color). Given a linear energy function, it can be shown that the assemblage will lie on one of the vertices where the constraint lines/hyperplanes intersect (circles) and the minimum can be found by walking through the vertices following the gradient of the Gibbs energy. Under the constraint of the example here, the energy minimum is marked by the green circle.

not necessarily optimal solution to the problem. Since the nodes lie on the boundary of the polytope (Figure 3.3), they satisfy at least some mass balance constraints exactly, i.e., in the equality sense. However, in cases where some phases contain very different relative amounts of chemical components than the bulk composition, it is possible that not all mass balance constraints can be satisfied exactly. The algorithm moves between neighboring nodes by reducing the modal amount of one phase while increasing that of another at the same time, such that the objective value does not increase in any step [Dantzig, 1963]. A simplified two-dimensional example of this procedure is illustrated in Figure 3.3.

LP_SOLVE offers a variety of configuration options controlling the initial scaling of the (primal) input problem, the setup of the (dual) equivalent problem [Lemke, 1954], where the mathematical roles of candidate phase energies and mass bounds are reversed, and the iterative improvement of the solution. We choose automatic scaling of the minimization problem not only to make the solution independent of any multipliers in the mass balance constraints, but also to bring all matrix entries close to unity, which greatly improves the numerical stability of the iterative solution process. The options related to the dual problem are at their default settings; they allow rearrangements of the initial problem to improve the feasibility of the initial dual solution candidate and accuracy monitoring during the iterative solution process. LP_SOLVE

Table 3.1: Timing measurements for calculations performed with EoS on one core of an Intel N3540 CPU at 2.16 GHz using the Birch-Murnaghan–Mie-Debye-Grüneisen equation-of-state (Section 2.3). Each computation type has been run many times and aggregate results are reported.

Calculation	Real Time s / 100 samples
Gibbs energy, simple phase / endmember	0.10
Gibbs energy, binary solution representative	0.15
Gibbs energy, ternary solution representative	0.17
Optimum assemblage, two simple phases	0.18
Optimum assemblage, two binary solution phases	10.89
Optimum assemblage, two ternary solution phases	217.04
Optimum assemblage, 21 phases, in total ≥ 46 pseudocompounds	5944.67

may switch between the regular and dual problem formulation to accelerate convergence or break cycles [e.g., Benichou et al., 1977, Lemke, 1954]. The pivoting options determine how replacement phases in the candidate assemblage are chosen: By default, the DEVEX pricing developed by Harris [1973] is used, as it offers a reasonable compromise between speed and accuracy, but an exact steepest edge selection is configured as a fallback in case the solver runs into a cycle of vertices. Both pricing strategies try to select the lowest-energy neighboring vertex, in case the current one is not optimal already: DEVEX pricing does so approximately, based on the objective function coefficients and column norm estimates, while true steepest edge selection requires the computation of gradients, hence it is slower [e.g., Benichou et al., 1977, Forrest and Goldfarb, 1992].

As the dimension of the optimization problem corresponds to the number of available candidate phases, the computational complexity of the algebraic operations needed to solve the problem can be reduced by excluding phases known not to occur in the result. EoS allows the user to manually configure the set of candidate phases used for an optimization, but does not exclude any phases *a-priori*. This may be problematic especially for phases whose Gibbs energy cannot be extrapolated reliably to the P, T of the optimization problem. However, deciding to exclude a phase from a computation requires expert knowledge about its stability.

3.4 Performance Measurements

The performance characteristics of the phase equilibrium solution process are dominated by the linear programming problem. Table 3.1 shows timing measurements for equation-of-state calculations and optimum assemblage computations. The cost of the equation-of-state computations increases noticeably from simple phases to solutions, as every endmember equation-of-state has to be computed in addition to a small overhead added by the solution model.

The solution of a single linear optimization problem is usually quite fast, which is demonstrated by the small overhead caused by LP_SOLVE relative to the time needed to compute the Gibbs energy for fixed composition candidate phases. However, computing phase equilibria involving solutions is considerably more complex: In addition

to multiple equation-of-state evaluations per phase, many linear programming problems have to be solved until both the optimal solution compositions and the optimal amounts of phases are found. The main factor for the computational cost of a complex phase equilibrium problem is the number of solution endmembers, which determines both the number of candidate pseudocompounds and the number of non-linear optimization steps.

Chapter 4

Application of Thermodynamic Models

4.1 Mineral Properties

In the following Sections, we explore volumetric, caloric and energetic properties of representative silicate phases over a wide P - T range using the thermodynamic datasets by [Stixrude and Lithgow-Bertelloni \[2011\]](#) for the Birch-Murnaghan–Mie-Debye–Grüneisen model and [Holland et al. \[2013\]](#) for the Caloric–Modified-Tait model. In the following discussion, we have retained all thermodynamic parameters as calibrated in the original studies [[Holland et al., 2013](#), [Stixrude and Lithgow-Bertelloni, 2011](#)] in order to preserve the integrity of each dataset [[Connolly, 2009](#)].

4.1.1 Volumetric Properties

We have computed molar volumes of forsterite (Mg_2SiO_4) and bridgmanite (MgSiO_3) over a wide P - T range using the thermodynamic models by [Stixrude and Lithgow-Bertelloni \[2011\]](#), [Holland et al. \[2013\]](#) and [Fabrighnaya et al. \[2004\]](#). Isothermal compression at 300 K and isobaric thermal expansion (Figure 4.1) show very similar behavior in all three models close to ambient conditions, but progressively diverge at higher P or T . Both the Birch-Murnaghan–Mie-Debye–Grüneisen model and the Caloric–Modified-Tait model have similar expressions for compression (*cf.* Section 2.3 and 2.2), and results for $V(P, T_0)$ are essentially identical (Figure 4.1). By contrast, the volume expression for the Caloric–Murnaghan model has a different structure and the calibration leads to a noticeably different P -dependence in volume for both phases; at higher P , larger volumes are computed by the model and calibration of [Fabrighnaya et al. \[2004\]](#).

The T -dependence of molar volume of forsterite and bridgmanite at 1 bar (Figure 4.1) reflects the fact that both caloric models [[Fabrighnaya et al., 2004](#), [Holland et al., 2013](#)] use the same heat-capacity-based formulation of thermal energies (Equation (2.7)). Both models exhibit similarly shaped V - T curves with some offset caused by differences in the parameter sets. The Birch-Murnaghan–Mie-Debye–Grüneisen model differs from the other two models in its treatment of Helmholtz

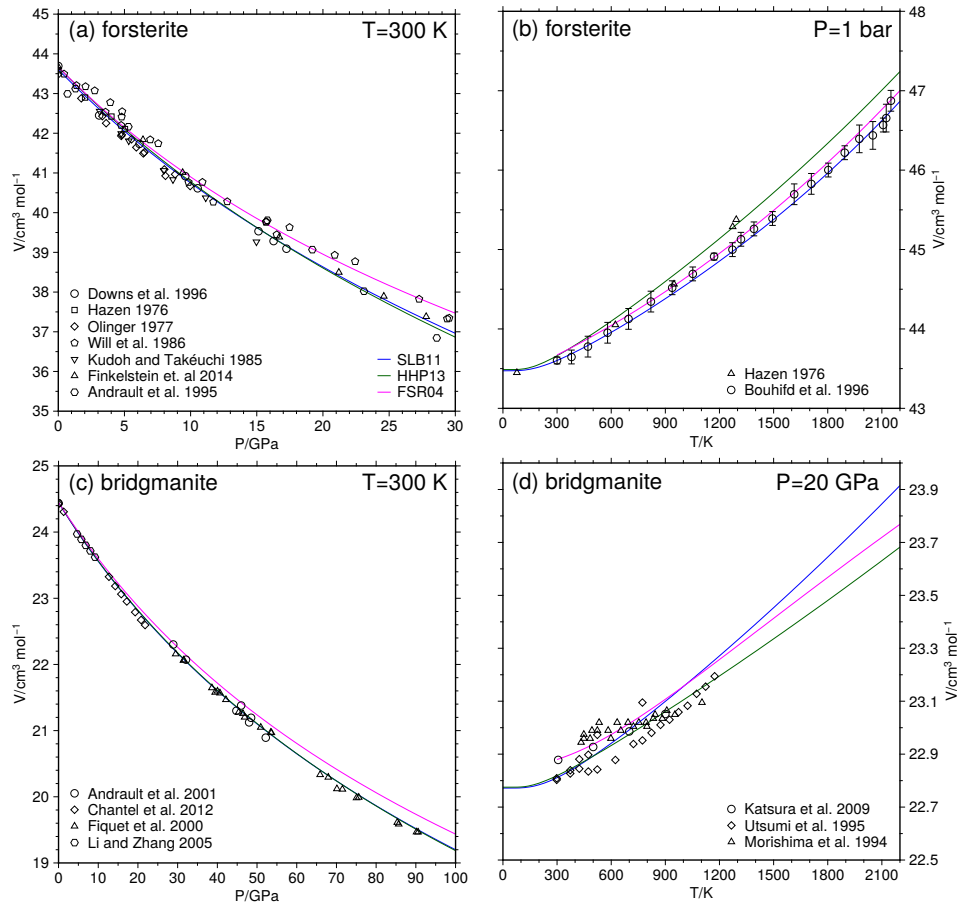


Figure 4.1: Molar volumes for forsterite (Mg_2SiO_4) (a, b) and bridgmanite (MgSiO_3) (c, d), computed with the EoS software using the model parameters from Stixrude and Lithgow-Bertelloni [2011] (blue lines), Holland et al. [2013] (green lines) and Fabrichnaya et al. [2004] (magenta lines), as a function of P (a, c) and T (b, d). In panel (a), symbols show experimental data from Hazen [1976] (squares), Olinger [1977] (diamonds), Kudoh and Takeuchi [1985] (inverse triangles), Will et al. [1986] (pentagons), Andraut et al. [1995] (hexagons), Downs et al. [1996] (circles) and Finkelstein et al. [2014] (triangles). In panel (b), symbols show experimental values reported by Hazen [1976] (triangles) and Bouhifd et al. [1996] (circles with error bars). In panel (c), symbols show experimental data from Fiquet et al. [2000] (triangles), Andraut et al. [2001] (circles), Li and Zhang [2005] (hexagons) and Chantel et al. [2012] (diamonds). In panel (d), symbols show experimental measurements between 19 GPa and 21 GPa by Morishima et al. [1994] (triangles), Utsumi et al. [1995] (diamonds) and Katsura et al. [2009] (circles).

energy contribution between ambient and elevated T , hence it shows physically different thermal expansion behavior. For bridgmanite, the calibration by Stixrude and Lithgow-Bertelloni [2011] exhibits a stronger volume expansion than the other two models, and agrees better with the trend of experimental data at higher T , especially those of Utsumi et al. [1995].

Overall, the volumetric properties predicted by the different formulations show how fundamental differences in capturing experimental data and fitting strategies affect specific parameterizations rather than the inability of the physical theory and functional form of the equation-of-state to represent material properties.

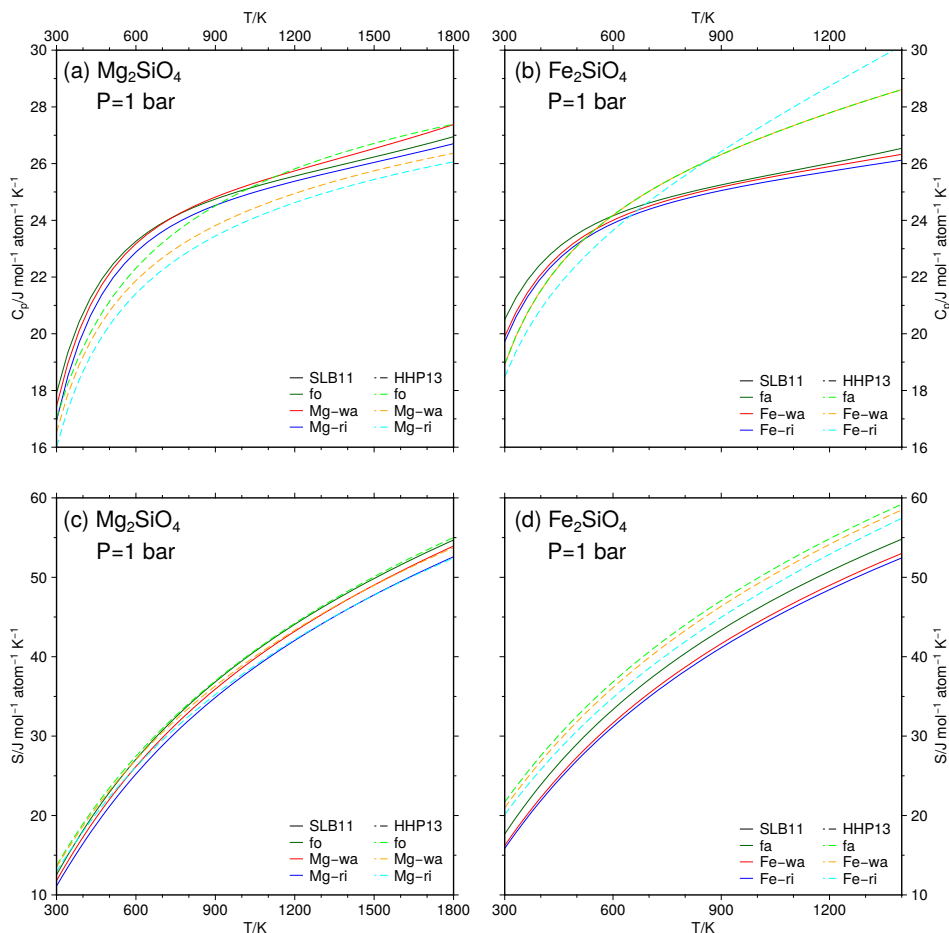


Figure 4.2: Thermal properties of olivine polymorphs at ambient P computed with EoS using the model parameters from [Stixrude and Lithgow-Bertelloni \[2011\]](#) (solid lines) and [Holland et al. \[2013\]](#) (dashed lines) as a function of T . Panels (a) and (b) show heat capacity per mole of atoms, panels (c) and (d) entropy per mole of atoms. Panels (a) and (c) contain the properties of the Mg_2SiO_4 -polymorphs forsterite (green), Mg-wadsleyite (red) and Mg-ringwoodite (blue). Panels (b) and (d) show the properties of the Fe_2SiO_4 -polymorphs fayalite (green), Fe-wadsleyite (red) and Fe-ringwoodite (blue). The T -scale differs for the Mg_2SiO_4 and Fe_2SiO_4 -polymorphs.

4.1.2 Caloric Properties

The principally different formulations of heat capacity in the caloric model vs. the Debye model propagate to entropy and Gibbs energy. The polynomial formulation by [Holland et al. \[2013\]](#) shows a significantly shallower slope at low T and a steeper increase at high T than the Debye model as parameterized by [Stixrude and Lithgow-Bertelloni \[2011\]](#) (Figure 4.2). The experimental data for forsterite and fayalite that extend to 1700 K and 800 K [[Robie and Hemingway, 1995](#), [Robie et al., 1982](#), [Watanabe, 1982](#)], respectively, are more closely reproduced by the calibration of [Holland et al. \[2013\]](#) (Figure 4.3). For the Fe_2SiO_4 polymorphs, differences between the models of [Holland et al. \[2013\]](#) and [Stixrude and Lithgow-Bertelloni \[2011\]](#) are even more pronounced, and become greater with increasing T .

Owing to the physically correct limiting behavior of the Debye model for isochoric heat capacity, the continued step increase in C_P in the polynomial model by [Holland et al. \[2013\]](#) appears unphysical. This is supported by the fact that the

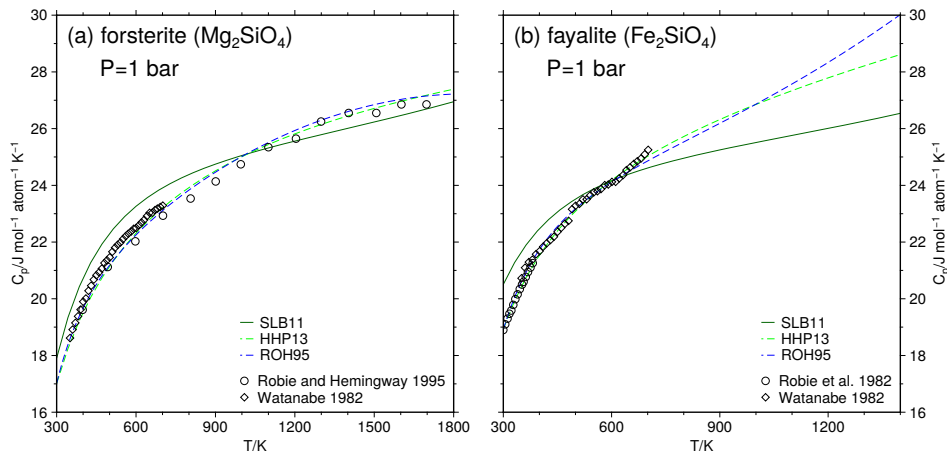


Figure 4.3: Heat capacity per mole of atoms for forsterite (a) and fayalite (b) at ambient P as functions of T , computed with EoS using the model parameters from [Stixrude and Lithgow-Bertelloni \[2011\]](#) (green solid lines) and [Holland et al. \[2013\]](#) (green dashed lines). The polynomial heat capacity approximations by [Robie and Hemingway \[1995\]](#) are included for comparison (blue dashed lines). Experimental data by [Robie and Hemingway \[1995\]](#) (black circles) and [Watanabe \[1982\]](#) (black diamonds) for forsterite and by [Robie et al. \[1982\]](#) (black circles) and [Watanabe \[1982\]](#) (black diamonds) for fayalite are included. The T -scale differs for panels (a) and (b).

isochoric heat capacity of fayalite exceeds the Dulong-Petit limit for insulators ($\sim 25 \text{ J K}^{-1} \text{ mol}^{-1} \text{ atom}^{-1}$) by $\sim 3 \text{ J K}^{-1} \text{ mol}^{-1} \text{ atom}^{-1}$ in [Holland et al. \[2013\]](#).

The nature of the Debye approximation used in the model of [Stixrude and Lithgow-Bertelloni \[2011\]](#) prevents a more accurate heat capacity fit for many phases as seen for olivine and fayalite at lower temperatures (Figure 4.3). The Debye model assumes that heat is stored entirely in the form of acoustic lattice vibrations that have a linear dispersion curve, and this leaves a single parameter, the Debye temperature θ_D to capture the phonon spectrum (*cf.* Section 2.3).

The deviations in C_P for the Mg_2SiO_4 polymorphs are less significant when integrated to entropy (Figure 4.2), and both the Caloric-Modified-Tait and Birch-Murnaghan-Mie-Debye-Grüneisen models describe the entropy of forsterite [[Robie and Hemingway, 1995](#)] equally well. For the Fe_2SiO_4 polymorphs heat capacities of fayalite and Fe-wadsleyite are degenerate in the model by [Holland et al. \[2013\]](#) (Figure 4.3), but the difference in entropy at T_0 results in larger entropy for fayalite, consistent with the model of [Stixrude and Lithgow-Bertelloni \[2011\]](#). However, entropies predicted for both fayalite and Fe-wadsleyite by the model of [Holland et al. \[2013\]](#) remain significantly larger than those of [Stixrude and Lithgow-Bertelloni \[2011\]](#) (Figure 4.2).

4.1.3 Gibbs Energy

Values and uncertainties of volumetric and caloric properties propagate through integration into the Gibbs energy of a phase (Equations (2.6), (2.7), (2.8), (2.10), (2.27), (2.33), (2.37) and (2.40)) that is essential for an accurate calculation of phase equilibria. Individual uncertainties are partially reduced due to inherent correlations in thermodynamic properties resulting from a large number of degrees of freedom, and therefore depend on the approach used in the construction of a specific thermody-

namic dataset. We illustrate these features by comparing the difference between Gibbs energy of the models and assessments by [Stixrude and Lithgow-Bertelloni \[2011\]](#) and [Holland et al. \[2013\]](#) from ambient conditions to 3000 K and 26 GPa for the Mg_2SiO_4 and Fe_2SiO_4 polymorphs (Figure 4.4).

For the Mg_2SiO_4 phases, the differences in Gibbs energy (ΔG) of forsterite, wadsleyite and ringwoodite between the databases of [Stixrude and Lithgow-Bertelloni \[2011\]](#) and [Holland et al. \[2013\]](#) do not exceed $1 \text{ kJ mol}^{-1} \text{ atom}^{-1}$ in general, over the whole P - T range considered (Figure 4.4). This is comparable to the nominal accuracy of internally consistent thermodynamic datasets. In particular, ΔG remains negligible ($< 0.2 \text{ kJ mol}^{-1} \text{ atom}^{-1}$) during compression to 26 GPa at ambient T (Figure 4.4). This indicates that the performance of the Modified-Tait and Birch-Murnaghan equations-of-state is essentially identical for the purpose of phase equilibrium calculations. By contrast, during heating at ambient P , ΔG either systematically increases or reaches a broad maximum between 1000 and 2000 K. This behavior is related to functional differences in the heat capacity models (empirical polynomial vs. Debye treatment) and illustrates persistent discrepancies in the caloric characterization of condensed phases at moderate and high T .

Insufficient or discrepant calibrations of compression or caloric properties tend to govern ΔG pattern in P - T space in a linear manner, as illustrated for the Fe_2SiO_4 polymorphs (Figure 4.4). In all three cases, the Gibbs energy difference is dominated by T dependence: it increases nearly linearly with T and reaches values of $\sim 15 \text{ kJ mol}^{-1} \text{ atom}^{-1} \text{ K}^{-1}$ at 3000 K. The steep, nearly linear increase of ΔG reflects the fact that the entropies of the Fe_2SiO_4 polymorphs in the models and assessments of [Stixrude and Lithgow-Bertelloni \[2011\]](#) and [Holland et al. \[2013\]](#) differ substantially (Figure 4.2). The similar magnitude of uncertainties for all polymorphs indicates that this deficiency does not primarily affect the phase equilibria in the one-component system Fe_2SiO_4 , but plays a significant role in the Mg_2SiO_4 - Fe_2SiO_4 solution or any more complex systems at high T as will be discussed in Section 4.2.3. Similar to the Mg_2SiO_4 polymorphs, the Gibbs energy differences for the Fe_2SiO_4 phases do not exceed $0.5 \text{ kJ mol}^{-1} \text{ atom}^{-1}$ during isothermal compression to 26 GPa.

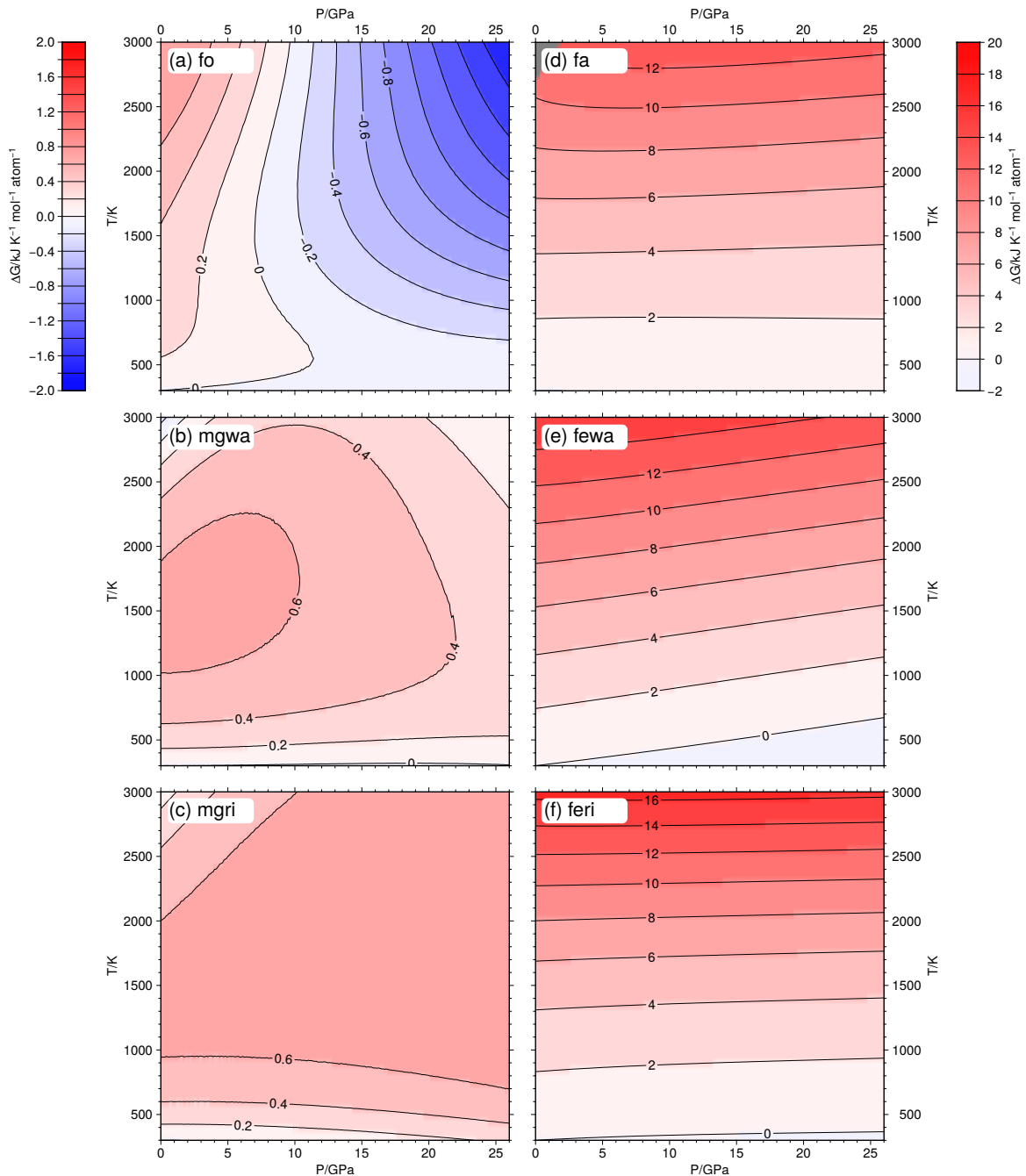


Figure 4.4: Differences of Gibbs energies computed using the parameter set of [Stixrude and Lithgow-Bertelloni \[2011\]](#) relative to those computed using parameters from [Holland et al. \[2013\]](#) as a function of P and T . Differences have been normalized to zero at ambient pressure and temperature. Panels (a), (b) and (c) show results for the Mg_2SiO_4 polymorphs forsterite, Mg-wadsleyite and Mg-ringwoodite. Panels (d), (e) and (f) show results for the Fe_2SiO_4 polymorphs fayalite, Fe-wadsleyite and Fe-ringwoodite.

4.2 Phase Diagrams

4.2.1 Phase Equilibria Involving Stoichiometric Phases

Thermodynamic models for pure stoichiometric phases can be used directly to compute phase diagrams for a given bulk composition. All phase diagrams presented here use fixed grid steps for their free variables. Pressure-temperature phase diagrams for the MgSiO_3 composition computed with the models of [Stixrude and Lithgow-Bertelloni \[2011\]](#) and [Holland et al. \[2013\]](#) are largely compatible with experimental data (Figure 4.5) and previous thermodynamic assessments [[Gasparik, 2003](#)]. Each thermodynamic model and its parameter set yields discrepancies in a different P - T range, but no systematic differences or problems in phase diagram topology are apparent. As such, both thermodynamic formulations [[Holland et al., 2013](#), [Stixrude and Lithgow-Bertelloni, 2011](#)] seem equally appropriate for computing phase diagrams. Differences stem primarily from the thermodynamic assessment of individual phases.

The model of [Stixrude and Lithgow-Bertelloni \[2011\]](#) fails to produce the clinoenstatite stability field at $P < 7 \text{ GPa}$ and $T < 1000 \text{ K}$ (Figure 4.5), although the phase is present in the database (Table B.2); the model of [Holland et al. \[2013\]](#), by contrast, reproduces the clinoenstatite stability field in the assessment by [Gasparik \[2003\]](#) well (Figure 4.5). At higher pressures, the models differ significantly in the extent of the akimotoite stability field. Akimotoite stability is virtually absent in the model by [Holland et al. \[2013\]](#), the model by [Stixrude and Lithgow-Bertelloni \[2011\]](#) reproduces experimental data [[Ishii et al., 2011](#), [Sawamoto, 1987](#)] reasonably well, and the thermodynamic assessment of [Gasparik \[2003\]](#) appears to overestimate experimental constraints on akimotoite stability (Figure 4.5).

Predictions of phase equilibria to pressures of the Earth's lower mantle are possible with the database of [Stixrude and Lithgow-Bertelloni \[2011\]](#) only, as [Holland et al. \[2013\]](#) have assessed their model only for $P < 34 \text{ GPa}$. At $P > 95 \text{ GPa}$, the model of [Stixrude and Lithgow-Bertelloni \[2011\]](#) predicts the bridgmanite-post-perovskite transition (Figure 4.5), in good agreement with experimental results [e.g., [Tateno et al., 2009](#)].

The pressure-temperature phase diagram for SiO_2 computed with the model of [Stixrude and Lithgow-Bertelloni \[2011\]](#) is in good agreement with the experimental data points along the $\alpha - \beta$ quartz phase boundary (Figure 4.6). This demonstrates good performance of the Landau model (Section 2.5) fitted to this phase transition. For the quartz-coesite transition on the other hand, the model prediction is less accurate, likely because the model assessment of [Stixrude and Lithgow-Bertelloni \[2011\]](#) does not focus on stability fields of pure SiO_2 phases without the presence of additional chemical components.

4.2.2 Configurational and Excess Mixing Properties

EoS uses the Bragg-Williams approximation to random distribution of atoms and their groups to compute the configurational entropy of solution phases (Section 2.6). Contributions to S_{cf} from independent mixing sites are additive and proportional to

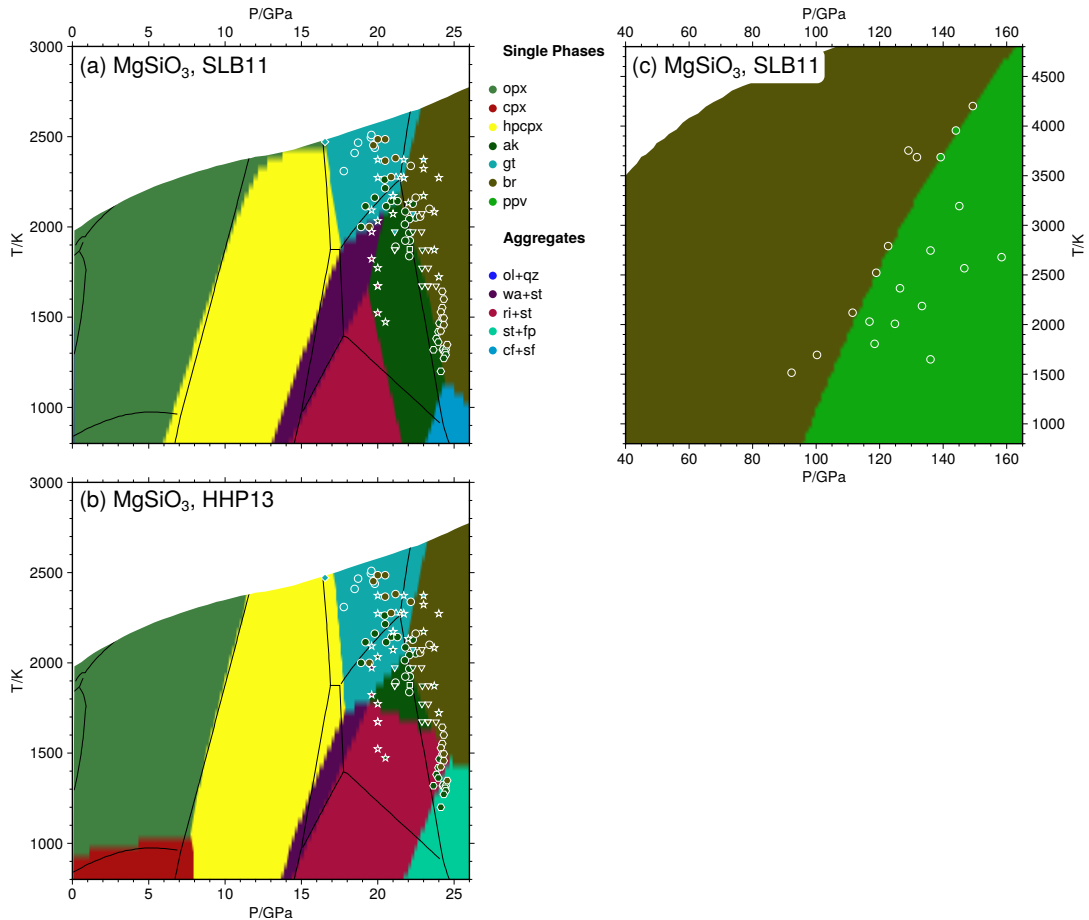


Figure 4.5: Stable polymorphs of phases with bulk composition MgSiO_3 at high P and T , predicted by EoS using the Birch-Murnaghan–Mie-Debye–Grüneisen model with the database of [Stixrude and Lithgow-Bertelloni \[2011\]](#) (a, c) and the Caloric–Modified-Tait model with parameters from [Holland et al. \[2013\]](#) (b). Results are computed with 0.1 GPa and 50 K grid spacing. Phase assemblages are color coded according to the legend (for abbreviations see Table B.2). Symbols show experimental data from several sources for stable phases using the corresponding color: In panels (a) and (b) by [Presnall et al. \[1998\]](#) (diamonds), [Chudinovskikh and Boehler \[2001\]](#) (circles), [Hirose et al. \[2001\]](#) (triangles), [Ono et al. \[2001\]](#) (hexagons), [Fei et al. \[2004\]](#) (squares), [Ishii et al. \[2011\]](#) (inverse triangles) and [Sawamoto \[1987\]](#) (stars); in panel (c) by [Tateno et al. \[2009\]](#) (circles). Solid lines are phase boundaries reported in [Gasparik \[2003\]](#).

the multiplicity of each site. The formulation of configurational properties becomes non-unique when partial ordering on one or more crystallochemical sites is considered. To implement ordering schemes, we introduce the following notation of nested parentheses for use in EoS: the first (outer) level $(\dots)_n$ designates a mixing site and the associated subscript n represents the mixing multiplicity (suppressed notation implies a multiplicity of one). The element amounts on a site are allowed to become fractional numbers. A second (inner) level of parentheses $((\dots))_n$ encloses groups of atoms that are considered to be a single entity for the purpose of configurational entropy calculations.

As an example, we consider the clinopyroxene solution between the enstatite $\text{Mg}_2\text{Si}_2\text{O}_6$ (en), diopside $\text{CaMgSi}_2\text{O}_6$ (di) and Ca-tschermak $\text{CaAl}_2\text{SiO}_6$ (cats) endmembers. The solid solution consists of three mixing sites – M2, M1 and T with the mixing

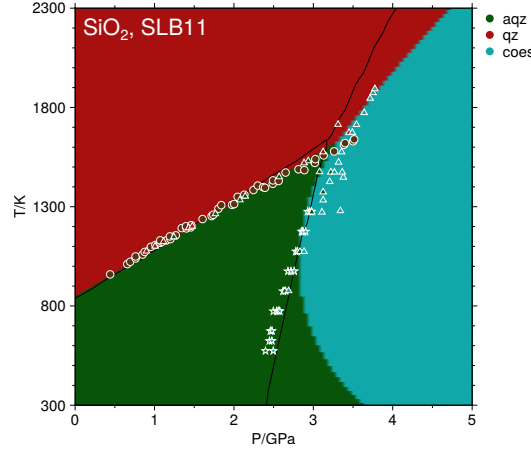


Figure 4.6: Stable phases with with bulk composition SiO_2 at low P and T , predicted by EoS using the Birch-Murnaghan–Mie-Debye-Grüneisen model and Landau model with the database of [Stixrude and Lithgow-Bertelloni \[2011\]](#). Results are computed with 0.05 GPa and 5 K grid spacing. Phases are color coded according to the legend (for abbreviations see [Table B.2](#)). Symbols show experimental data from several sources for stable phases using the corresponding color: [Bohlen and Boettcher \[1982\]](#) (stars), [Cohen and Klement \[1967\]](#) (circles, aqz-qz boundary) and [Mirwald and Massonne \[1980\]](#) (triangles). Solid lines are phase boundaries reported in [Gasparik \[2003\]](#).

multiplicities of one, one and two, respectively – per six-oxygen formula unit [[Putnis, 1992](#)].

Figure 4.7(a) shows the configurational entropy of Mg-Ca mixing along the enstatite–diopside binary join on the M2 site; the result is symmetric, reaching the entropy maximum where both atom species are mixed in equal parts:

$$S_{\text{cpx}} = -R \cdot (x \ln x + (1 - x) \ln(1 - x)), \quad (4.1)$$

with x the mole fraction of diopside.

The behavior along the diopside–Ca-tschermak binary join is more complex. Figure 4.7(b) compares various scenarios for Al-Si distribution on the tetrahedral site of clinopyroxene found in the literature [[Cohen, 1986](#), [Gasparik, 1984](#), [Vinograd, 2001](#)]:

- (i). Random mixing of Mg and Al on the M1 octahedral site and of Al and Si on the tetrahedral site with mixing multiplicity $n = 2$, represented by the solution formula $\text{Ca}(\text{Mg,Al})(\text{Al,Si})_2\text{O}_6$. The configurational entropy of the diopside–Ca-tschermak solid solution becomes:

$$S_{\text{cpx}} = -R \cdot \left(x \ln x + (1 - x) \ln(1 - x) + 2 \frac{x}{2} \ln \frac{x}{2} + 2 \left(1 - \frac{x}{2} \right) \ln \left(1 - \frac{x}{2} \right) \right), \quad (4.2)$$

where x is the mole fraction of Ca-tschermak. The configurational contribution to the Ca-tschermak endmember resulting from Al-Si disorder is

$$S_{\text{cats}} = -R \cdot 2 \cdot \left(\frac{1}{2} \ln \frac{1}{2} + \frac{1}{2} \ln \frac{1}{2} \right) \approx 11.53 \text{ J K}^{-1} \text{ mol}^{-1}. \quad (4.3)$$

- (ii). Random mixing of Mg and Al on the M1 octahedral site and ordering of Al and Si on the tetrahedral sites, subject to the Al-avoidance principle [[Loewenstein,](#)

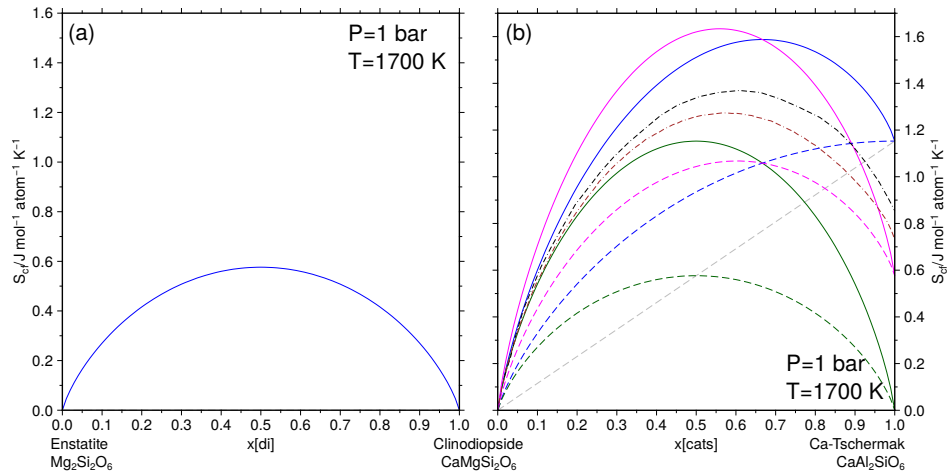


Figure 4.7: Entropy of solution per mole of atoms (a) between enstatite ($\text{Mg}_2\text{Si}_2\text{O}_6$) and clinodiopside ($\text{CaMgSi}_2\text{O}_6$) and (b) between clinodiopside ($\text{CaMgSi}_2\text{O}_6$) and Ca-tschermak ($\text{CaAl}_2\text{SiO}_6$): In panel (a), the solid blue line represents configurational entropy; in panel (b), the solid blue, green and magenta lines represent mixing entropies for ionic models with two or three effective mixing sites, the dashed colored lines represent charge-coupled models with one or two effective mixing sites. The dashed gray line represents a linear combination of endmember entropies with internal disorder. The solid blue and dashed gray entropy curves are computed using the structure $(\text{Ca})(\text{Mg})(\text{Si})_2\text{O}_6$ for clinodiopside and $(\text{Ca})(\text{Al})(\text{Al}_{\frac{1}{2}}\text{Si}_{\frac{1}{2}})_2\text{O}_6$ for Ca-tschermak, while the solid green curve results from a structure $(\text{Ca})(\text{Mg})(\text{Si})\text{SiO}_6$ for clinodiopside and $(\text{Ca})(\text{Al})(\text{Al})\text{SiO}_6$ for Ca-tschermak. The solid magenta curve is computed using the structure $(\text{Ca})(\text{Mg})(\text{Si})(\text{Si})\text{O}_6$ for clinodiopside and $(\text{Ca})(\text{Al})(\text{Al}_{\frac{1}{2}}\text{Si}_{\frac{1}{2}})(\text{Al}_{\frac{1}{2}}\text{Si}_{\frac{1}{2}})\text{O}_6$ for Ca-tschermak. The dashed colored curves use structures analogous to those for the solid curves, but omitting the Mg-Al mixing terms. The two dash-dotted curves represent configuration entropy models by Vinograd [2001] (brown) and Cohen [1986] (black).

1954]. This requirement is analogous to formally splitting the tetrahedral sites into T2, hosting Si and Al, and T1, occupied by Si only. This element allocation is represented by the solution formula $\text{Ca}(\text{Mg},\text{Al})(\text{Al},\text{Si})\text{SiO}_6$. The configurational entropy of the diopside–Ca-tschermak solution is then defined as:

$$S_{\text{cpX}} = -R \cdot (x \ln x + (1-x) \ln(1-x) + x \ln x + (1-x) \ln(1-x)). \quad (4.4)$$

There is no configurational contribution to the entropy of Ca-tschermak in this model as all sites are occupied by one element only. The results of this scenario, however, contradicts previous experimental measurements and thermodynamic assessments [Cohen, 1986, Gasparik, 1984, Vinograd, 2001]. Intermediate configurational entropy of the Ca-tschermak endmember can be obtained by adopting partial order in the tetrahedral site or by charge coupling between the tetrahedral and octahedral sites.

- (iii). The Al-avoidance rule for the tetrahedral site is partially taken into account partially by assuming Al-Si avoidance on the T1 site and the Al-Si disorder on the T2 site. This situation corresponds to alternation of chains with disordered and partially ordered aluminosilicate tetrahedra, respectively, and is expressed by the solution formula $\text{Ca}(\text{Mg},\text{Al})(\text{Si},\text{Al})(\text{Si}_{\frac{1}{2}}\text{Al}_{\frac{1}{2}})\text{Si}_{\frac{1}{2}}\text{O}_6$; the site allocation for the Ca-tschermak endmember becomes $\text{Ca}(\text{Al})(\text{Al}_{\frac{1}{2}}\text{Si}_{\frac{1}{2}})(\text{Al})_{\frac{1}{2}}\text{Si}_{\frac{1}{2}}\text{O}_6$. The element fractions on the T2 site are related to the mole fraction of Ca-tschermak by $x_{\text{Al},\text{T}2} = \frac{x}{2}$

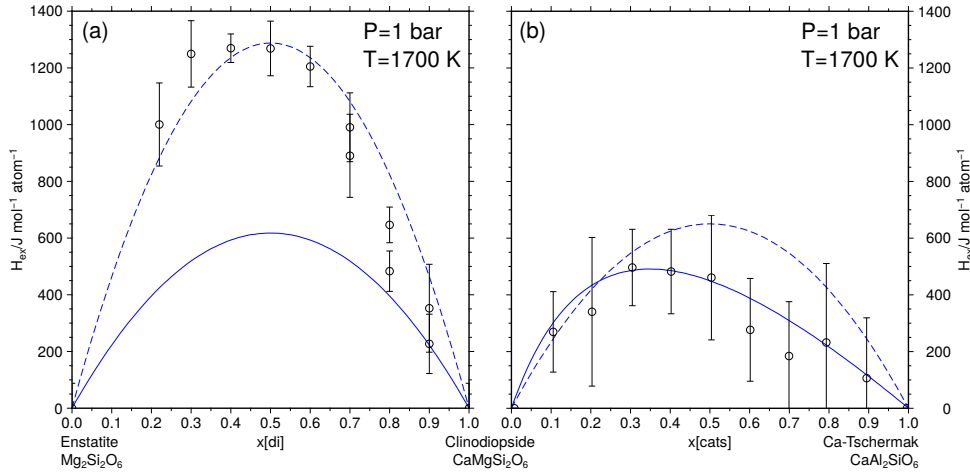


Figure 4.8: Excess enthalpy of solution per mole of atoms (a) between enstatite ($\text{Mg}_2\text{Si}_2\text{O}_6$) and clinodiopside ($\text{CaMgSi}_2\text{O}_6$) and (b) between clinodiopside ($\text{CaMgSi}_2\text{O}_6$) and Ca-tschermak ($\text{CaAl}_2\text{SiO}_6$). In panel (a) the solid blue line shows the computed values using model parameters from [Stixrude and Lithgow-Bertelloni \[2011\]](#) with an interaction parameter $W_{\text{en,di}} = 2.47 \text{ kJ mol}^{-1} \text{ atom}^{-1}$, the dashed blue line represents a modified parameter set with $W_{\text{en,di}} = 5.15 \text{ kJ mol}^{-1} \text{ atom}^{-1}$, following [Fei et al. \[1986\]](#). Circles and error bars show experimental data by [Newton et al. \[1979\]](#). In panel (b) the solid blue line represents computed values using the model parameters from [Stixrude and Lithgow-Bertelloni \[2011\]](#) with size parameters $d_{\text{di}} = 1, d_{\text{cats}} = 3.5$, which results in the maximum H_{ex} at $x_{\text{cats}} \approx 0.28$; the dashed blue line shows computed values for a symmetric parameter set with $d_{\text{di}} = d_{\text{cats}} = 1$, with the maximum H_{ex} at $x_{\text{cats}} = 0.5$. Circles and error bars show experimental data by [Benisek et al. \[2007\]](#).

and $x_{\text{Si,T2}} = 1 - \frac{x}{2}$. The configurational entropy of the diopside–Ca-tschermak solution is then calculated as:

$$S_{\text{cpx}} = -R \cdot \left(x \ln x + (1-x) \ln(1-x) + \frac{1}{2}(x \ln x + (1-x) \ln(1-x)) + \frac{1}{2} \left(\frac{x}{2} \ln \frac{x}{2} + \left(1 - \frac{x}{2}\right) \ln \left(1 - \frac{x}{2}\right) \right) \right). \quad (4.5)$$

Consequently, the Ca-tschermak entropy is

$$S_{\text{cats}} = -R \cdot \left(\frac{1}{2} \ln \frac{1}{2} + \frac{1}{2} \ln \frac{1}{2} \right) \approx 5.76 \text{ J K}^{-1} \text{ mol}^{-1}. \quad (4.6)$$

In all three models, the requirement of local charge balance may further reduce the configurational entropy because the Mg–Al distribution in the octahedral site depends on the Al–Si distribution in the tetrahedral site(s). The charge balance constraint does not affect S_{cf} of Ca-tschermak, but it decreases by $5.76 \text{ J K}^{-1} \text{ mol}^{-1}$ at the center of the binary join (Figure 4.7, dashed curves).

These considerations illustrate that simple Bragg–Williams models offer a sufficient range of versatility to reproduce simulation results or experimental data. In particular the ionic disordered case (scenario (i)) is within the error interval of [Cohen \[1986\]](#).

Excess mixing of solution phases is described by binary interaction terms, $W_{i,j}$ in Equation (2.79), and can acquire compositional asymmetry through the size parameters for individual endmembers d_i in Equation (2.80). The application of this

formalism is illustrated in the clinoenstatite-diopside solid solution (Figure 4.8), formulated symmetrically with $W_{\text{cen,di}} = 2.47 \text{ kJ mol}^{-1} \text{ atom}^{-1}$ in the database of [Stixrude and Lithgow-Bertelloni \[2011\]](#) (Figure 4.8), which poorly represents the experimental data of [Newton et al. \[1979\]](#). A larger symmetric interaction energy, $W_{\text{cen,di}} = 5.15 \text{ kJ mol}^{-1} \text{ atom}^{-1}$, based on an average of asymmetric interaction energies of [Fei et al. \[1986\]](#) provides a significantly improved fit to the experimental data. Using the latter, larger symmetric interaction energy based on [Fei et al. \[1986\]](#), leads to $H_{\text{ex}} \approx 1.3 \text{ kJ mol}^{-1} \text{ atom}^{-1}$, which is comparable in magnitude to the configurational Gibbs energy of $\sim 1.0 \text{ kJ mol}^{-1} \text{ atom}^{-1}$ (at 1700 K) that stems from $-TS_{\text{cf}}$ term in Equation (2.75).

The experimental data for the diopside-Ca-tschermak solid solution show significantly greater asymmetry [[Benisek et al., 2007](#)] and this feature has been fit with different size parameters for the endmembers in the model by [Stixrude and Lithgow-Bertelloni \[2011\]](#) (Figure 4.8). In this case, symmetric models are inadequate to describe excess mixing properties.

4.2.3 Phase Equilibria Involving Solid Solutions

We illustrate two principal binary phase diagrams as a function of P (at constant T): Mg_2SiO_4 - Fe_2SiO_4 (Figure 4.9) and $\text{Mg}_2\text{Si}_2\text{O}_6$ - $\text{CaMgSi}_2\text{O}_6$ (Figure 4.10), which have different degrees of complexity in their mixing properties.

For the Mg_2SiO_4 - Fe_2SiO_4 phase diagram we employ endmember thermodynamic properties from the models of [Stixrude and Lithgow-Bertelloni \[2011\]](#), [Xu et al. \[2008\]](#) and [Holland et al. \[2013\]](#), combined with the mixing properties of olivine, wadsleyite, ringwoodite, ferropericlase and bridgmanite (Mg- and Fe-bridgmanite). All phase diagrams are qualitatively similar (Figure 4.9) and reproduce the sequence of olivine, wadsleyite and ringwoodite solid solutions with increasing P , followed by a breakdown of $(\text{Mg,Fe})_2\text{SiO}_4$ to bridgmanite and ferropericlase at $x_{\text{Fe}} < 0.6$.

For Mg_2SiO_4 , the experimentally observed sequence and pressures of phase transitions are better reproduced by [Holland et al. \[2013\]](#), but the ringwoodite breakdown is predicted to occur at significantly larger P (24.2 GPa vs. 21.7 – 23.6 GPa from experiments [[Fei et al., 2004](#), [Irifune et al., 1998](#), [Ito and Takahashi, 1989](#), [Katsura et al., 2003](#)]). Both parametrizations of the Birch-Murnaghan–Mie-Debye–Grüneisen model [[Stixrude and Lithgow-Bertelloni, 2011](#), [Xu et al., 2008](#)] yield better results in that respect, and provide a reasonable description of the Mg_2SiO_4 polymorphic transitions (within 1 GPa).

For Fe_2SiO_4 , significant differences exist for the high- P transitions between the different models. Experimentally, fayalite transforms to Fe-ringwoodite, followed by a dissociation reaction to stishovite and wüstite [[Katsura et al., 2003](#), [Yagi et al., 1987](#)]. These transitions are correctly predicted by the models of [Xu et al. \[2008\]](#) and [Stixrude and Lithgow-Bertelloni \[2011\]](#) within 0.5 GPa from experimental values (Figure 4.9). By contrast, the assessment of [Holland et al. \[2013\]](#) predicts a narrow stability range of Fe-wadsleyite (6.2 – 6.3 GPa).

In contrast to the database by [Holland et al. \[2013\]](#), Fe-wadsleyite is considered too unstable with the parameters of [Xu et al. \[2008\]](#), with the metastable fayalite-Fe-wadsleyite transition predicted at 12.2 GPa, in contrast to 6.6 GPa for the database

of [Stixrude and Lithgow-Bertelloni \[2011\]](#) or 8.3 GPa in the assessment by [Gasparik \[2003\]](#).

As the invariant endmember transitions expand into divariant fields of two-phase coexistence, significant differences between model results of the Birch-Murnaghan-Mie-Debye-Grüneisen parametrizations [[Stixrude and Lithgow-Bertelloni, 2011](#), [Xu et al., 2008](#)] and [Holland et al. \[2013\]](#) arise due to the assessment of Fe-wadsleyite.

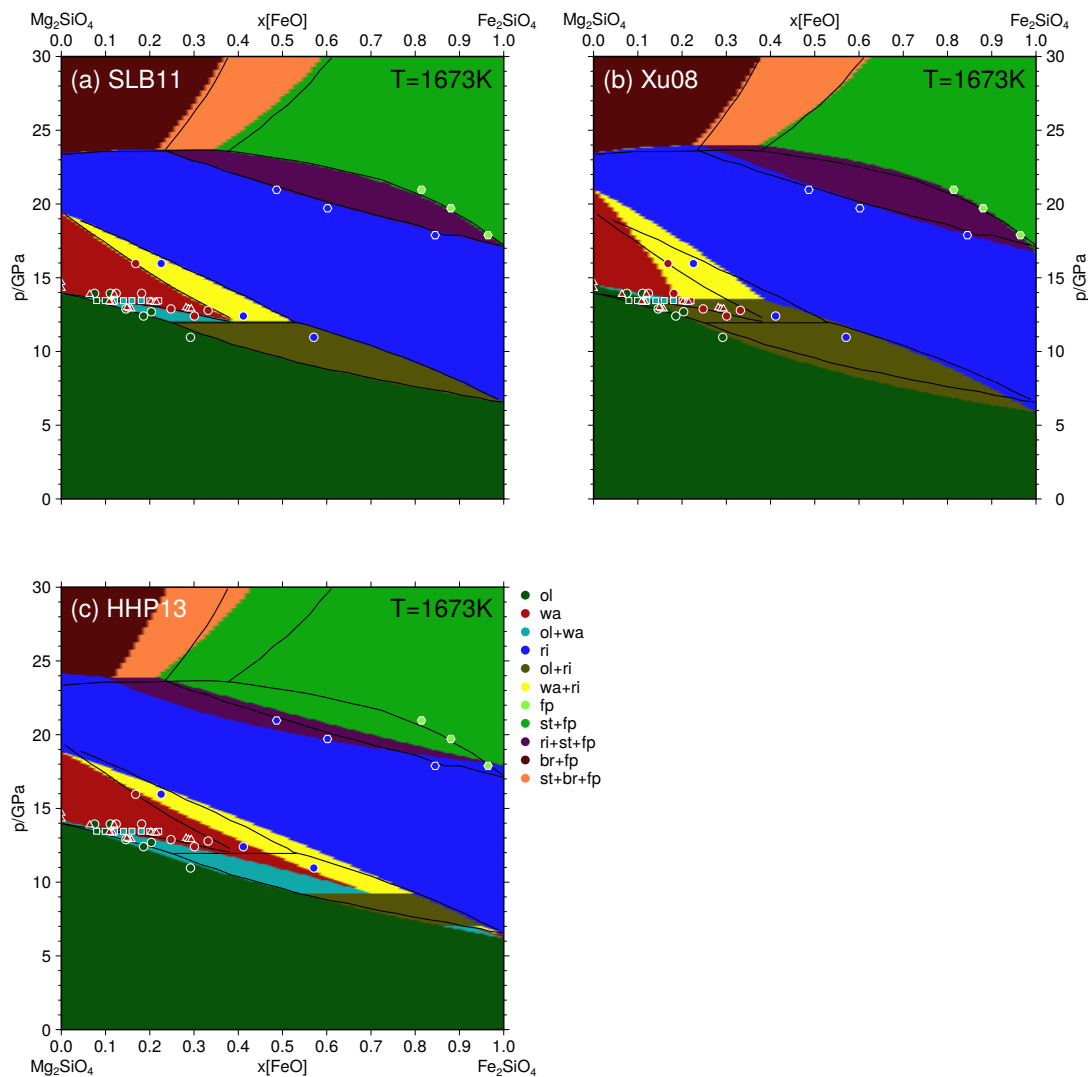


Figure 4.9: Stable phase assemblages along the compositional join $\text{Mg}_2\text{SiO}_4\text{-Fe}_2\text{SiO}_4$ at $T = 1673\text{ K}$ computed using EOS in comparison to experimental data of stable phases. Results are computed with 0.1 GPa and 1 mol% grid spacing. In panel (a) the thermodynamic model parameters from [Stixrude and Lithgow-Bertelloni \[2011\]](#) are used, while panel (b) is computed using parameters from [Xu et al. \[2008\]](#), both with the Birch-Murnaghan-Mie-Debye-Grüneisen model. Panel (c) is computed with the Caloric-Modified-Tait model using parameters from [Holland et al. \[2013\]](#). In all panels, the phase stability fields are color-coded according to the legend (for abbreviations see Table B.2), and solid lines show calculated phase boundaries reported in [Stixrude and Lithgow-Bertelloni \[2011\]](#). The symbols show experimental data of stable phases using the same color, taken from [Matsuzaka et al. \[2000\]](#) (hexagons), [Frost \[2003a\]](#) (circles) and [Fei and Bertka \[1999\]](#) (squares). The triangles show experimentally determined points at the boundary of the olivine and wadsleyite coexistence region from [Fei and Bertka \[1999\]](#).

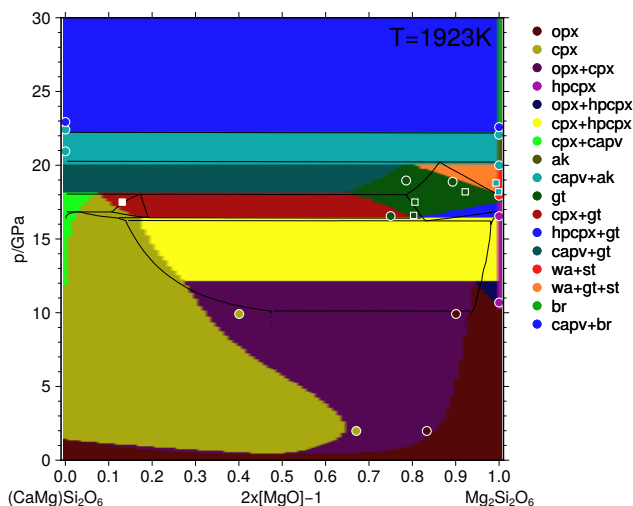


Figure 4.10: Stable phases along the diopside-enstatite $((\text{CaMg})\text{Si}_2\text{O}_6)\text{-Mg}_2\text{Si}_2\text{O}_6$ join at $T=1923\text{ K}$ computed using EoS and the thermodynamic parameters from [Stixrude and Lithgow-Bertelloni \[2011\]](#) with 0.1 GPa and $1\text{ mol}\%$ grid spacing. The phase stability fields are color-coded according to the legend (for abbreviations see [Table B.2](#)). Circles show experimental data for the assemblage in matching colors, compiled in [Stixrude and Lithgow-Bertelloni \[2011\]](#). Squares show experimental data from [Gasparik \[1990a\]](#), the white square indicates the CM phase. Solid lines are phase boundaries reported in [Gasparik \[2003\]](#), dotted lines are extrapolated from that assessment.

The stability of Fe-wadsleyite is directly responsible for the prediction of small coexistence regions of olivine and wadsleyite as well as wadsleyite and ringwoodite at the Fe-rich side of the phase diagram in the model of [Holland et al. \[2013\]](#), and a contraction of the olivine and ringwoodite coexistence region at $x_{\text{Fe}} = 0.55 - 0.95$ ([Figure 4.9](#)). Experimentally, this coexistence region is much broader, starting from $x_{\text{Fe}} > 0.12$ or 0.20 at the expense of wadsleyite-bearing assemblages [e.g., [Katsura and Ito, 1989](#)].

At higher P , the stability field of stishovite appears to be overestimated by all models, but most significantly by the [Holland et al. \[2013\]](#) dataset, shifting the bridgmanite stability to lower x_{Fe} and substantially decreasing the stability range of the assemblage ringwoodite, stishovite and ferropericlase ([Figure 4.9](#)), below the experimentally observed x_{Fe} values [[Ito and Takahashi, 1989](#)].

Major differences between the two assessments of the Birch-Murnaghan-Mie-Debye-Grüneisen models [[Stixrude and Lithgow-Bertelloni, 2011](#), [Xu et al., 2008](#)] are observed in a decrease of the olivine and ringwoodite stability field, with x_{Fe} shifting from 0.15 [[Xu et al., 2008](#)] to 0.30 [[Stixrude and Lithgow-Bertelloni, 2011](#)] between the two databases. Similar to the problems of the database by [Holland et al. \[2013\]](#) to reproduce the olivine and ringwoodite stability field in the phase diagram, the large extent of this coexistence region in the assessment by [Xu et al. \[2008\]](#) can be traced to the Fe-wadsleyite parametrization, as outlined above.

The system $\text{Mg}_2\text{Si}_2\text{O}_6\text{-CaMgSi}_2\text{O}_6$ provides an example with complex, reciprocal solution models and pseudo-binary mineral stabilities (e.g., garnet). Using the database by [Stixrude and Lithgow-Bertelloni \[2011\]](#), the pyroxene endmembers are predicted stable up to 16 GPa at $T = 1923\text{ K}$ ([Figure 4.10](#)). For enstatite, phases occur according to the MgSiO_3 phase diagram ([Figure 4.5](#)). On the diopside side, Ca-perovskite forms at $P > 12\text{ GPa}$ and high Ca-concentrations. Above 18 GPa it extends

to a wide composition range, consistent with the assessment by Gasparik [2003] and experimental data on diopside [Akaogi et al., 2004, Canil, 1994]. In addition, garnet is predicted to be stable between 16 and 20 GPa and $x_{Ca} \leq 0.80$, over a slightly larger composition range than in the assessment by Gasparik [2003], probably due to the fact that the CM phase described by Gasparik [1990a,b] is not included in the assessment of Stixrude and Lithgow-Bertelloni [2011]. Above 20 GPa, garnet transforms to akimotoite (20 GPa) and then to bridgmanite (22 GPa), consistent with the thermodynamic assessment of the system [Gasparik, 2003] and experiments by Akaogi et al. [2004] on diopside.

4.3 Elastic Properties

Density and elastic moduli are among the most important physical properties for applications in geodynamics and seismology. For pure phases, including endmembers of the solid solutions, analytical expressions are used in EoS, similar to other studies [Cottaar et al., 2014], and for solid solutions and polyphase aggregates we use volume weighted mixing rules (*cf.* Sections 2.6 and 2.7).

4.3.1 Elasticity of Garnets

We illustrate the application of the thermoelastic model of Stixrude and Lithgow-Bertelloni [2011] for density and elastic properties (shear and bulk modulus) in three garnet binary solutions that play a central role through the upper mantle and the transition zone [e.g., Ishii et al., 2011, Ita and Stixrude, 1992] (Figures 5.1, 5.8 and 5.11): $Mg_3Al_2Si_3O_{12}$ - $Fe_3Al_2Si_3O_{12}$ (pyrope-almandine), $Mg_3Al_2Si_3O_{12}$ - $Ca_3Al_2Si_3O_{12}$ (pyrope-grossular) and $Mg_3Al_2Si_3O_{12}$ - $Mg_4Si_4O_{12}$ (pyrope-majorite). The agreement of density with data from ambient to high pressures is very good overall (Figure 4.11).

Elastic moduli of the garnet binaries at elevated pressures show significantly larger scatter around the values computed with the database of Stixrude and Lithgow-Bertelloni [2011] (Figure 4.11), most prominently along the pyrope-majorite join with a large number of experimental studies. Experimental measurements for pyrope by Gwanmesia et al. [2006], Zou et al. [2012] and Chantel [2012] show significantly differing P -dependence for both the shear and bulk modulus. In addition, the reference values of the bulk and shear moduli at ambient pressure vary between the experiments of Gwanmesia et al. [2006], Sinogeikin and Bass [2002a] and Chantel [2012] by as much as 10 GPa and 6 GPa, respectively. Across the solution, moduli of most studies [Liu et al., 2015, Pamato et al., 2016, Sinogeikin and Bass, 2002a] agree reasonably well with the model predictions of Stixrude and Lithgow-Bertelloni [2011], while values of Chantel [2012] are significantly lower and those of Gwanmesia et al. [2009] significantly larger.

Although these discrepancies likely stem from uncertainties in the experimental data, it is possible – in principle – that the elastic parameters show non-linear dependence that is not captured by the quasi-linear formulation of elasticity in the mixing model (Equation (2.86)). In order to accommodate non-linear behavior, the model formulation would need to be modified. However, the possibility of non-linear elastic

behavior across a solid solution remains an open question, even at ambient conditions for a well studied system such as grossular-andradite [Lacivita et al., 2014, O'Neill et al., 1989].

4.3.2 Elasticity of MgSiO_3 Phases

In addition, we compute the elastic properties for the stable assemblage with MgSiO_3 composition as a function of P at room T (Figure 4.12). When the system is predicted to consist of a single phase, i.e., enstatite at $P < 11$ GPa and bridgmanite at $P > 32$ GPa, the model results agree well with experimental data [Jackson et al., 2007, Kung et al., 2004, Murakami et al., 2007]. In the intermediate pressure range, two phases are predicted to coexist: stishovite and ringwoodite at $P = 11 - 22$ GPa

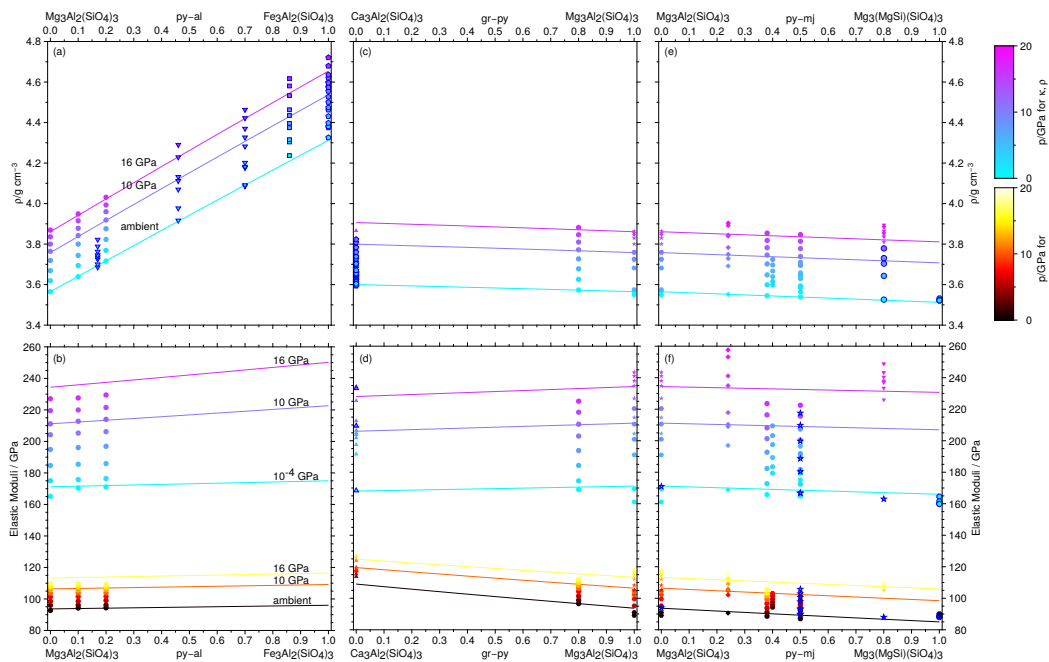


Figure 4.11: Compositional dependence of elastic properties in garnet binary solutions computed with EOS using model parameters from Stixrude and Lithgow-Bertelloni [2011] at room T . Panels (a) and (b) contain properties along the pyrope-almandine join; panels (c) and (d) for the grossular-pyrope join; panels (e) and (f) for the pyrope-Mg-majorite join. Panels (a, c, e) show densities, panels (b, d, f) elastic moduli. The properties have been computed at three different pressures (1 bar, 10 GPa, 16 GPa) and both experimental data and computed curves are color-coded by pressure (blue to magenta colors are used for the bulk moduli and densities, dark red to light yellow colors for the shear moduli). Experimental data are shown using symbols. In the pyrope-almandine system (a, b): Chantel [2012] (circles), Huang and Chen [2014] (inverse triangles with outline), Fan et al. [2009] (squares with outline), and Zhang et al. [1999] (pentagons with outline). In the grossular-pyrope system (c, d): Kono et al. [2010] (triangles), Gréaux et al. [2011] (triangles with outline), Zhang et al. [1999] (pentagons with outline), Pavese et al. [2001] (hexagons with outline), Gwanmesia et al. [2006] (hexagons), Chantel [2012] (circles), and Zou et al. [2012] (stars). In the pyrope-Mg-majorite system (e, f): Gwanmesia et al. [2006] (hexagons), Zou et al. [2012] (stars), Sinogeikin and Bass [2002a,b] (stars with outline), Pamato et al. [2016] (diamonds), Chantel [2012] (circles), Gwanmesia et al. [2009] (octagons), Liu et al. [2015] (inverse triangles), Morishima et al. [1999] (circles with outline), and Gwanmesia et al. [1998] (octagons with outline). To avoid confusion, data from Chantel [2012] for pure pyrope are only shown in panels (a) and (b).

[*cf.* Jiang et al., 2009, Shieh and Duffy, 2002, Sinogeikin et al., 2003], and stishovite and periclase at $P = 22 - 32$ GPa [*cf.* Murakami et al., 2009, Zha et al., 2000]. Voigt-Reuss-Hill averages of experimental elastic moduli agree well with predictions from the thermodynamic model by Stixrude and Lithgow-Bertelloni [2011].

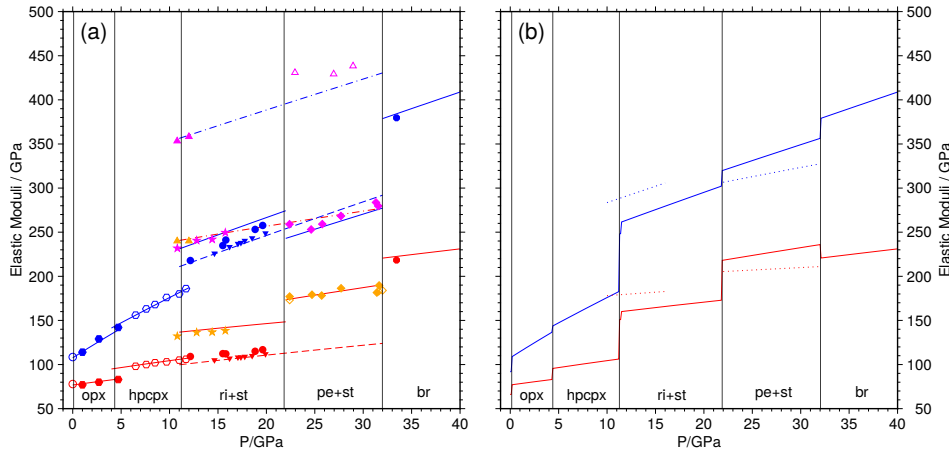


Figure 4.12: Bulk (blue) and shear moduli (red) of single phases (a) and the stable assemblage with MgSiO_3 bulk composition (b) at room T , computed with the EoS software using the model parameters from Stixrude and Lithgow-Bertelloni [2011]. Annotations at the bottom indicate the stable phase assemblages in the pressure ranges delimited by vertical lines (*cf.* Figure 4.5; for abbreviations see Table B.2). In panel (a) lines show computed single phase properties. Between 11 GPa and 22 GPa, the solid lines show computed elastic moduli of ringwoodite, between 22 GPa and 32 GPa they show the properties of periclase; between 11 GPa and 22 GPa, the dash-dotted lines show the moduli of stishovite and the dashed lines those of Mg-majorite. Symbols show experimental data for orthoenstatite by Kung et al. [2004] (filled hexagons) and by Jackson et al. [2007] (empty circles), for high-pressure clinoenstatite by Kung et al. [2004] (empty hexagons), for ringwoodite by Sinogeikin et al. [2003] (filled stars), for periclase by Zha et al. [2000] (filled diamonds) and by Murakami et al. [2009] (empty diamonds), for stishovite by Shieh and Duffy [2002] (empty triangles) and by Jiang et al. [2009] (filled triangles), for bridgmanite by Murakami et al. [2007] (filled octagons), for Mg-majorite by Pamato et al. [2016] (filled circles) and for $\text{mj}_{80}\text{py}_{20}$ by Liu et al. [2015] (inverse triangles). Data points for single phases that do not represent the entire stable assemblage are colored in magenta (bulk moduli) and orange (shear moduli). In panel (b) the solid lines show the computed properties of the stable phase assemblages, the dotted lines show Voigt-Reuss-Hill averages of interpolated experimental moduli for the computed stable phase assemblages.

The assemblages stable at room temperature do not contain garnet, as the majorite endmember in the system MgSiO_3 only becomes stable at higher temperatures (Figure 4.5). Nevertheless, garnets play a critical role in the upper mantle and the transition zone of the mantle (*cf.* Chapter 5), and majorite data and results are included in Figure 4.12. For majorite, the predictions based on the model of Stixrude and Lithgow-Bertelloni [2011] agree well with experimental data by Liu et al. [2015] and Pamato et al. [2016] (*cf.* Figure 4.11).

Chapter 5

Phase Equilibria in the Mantle

5.1 Pyrolite Assemblages

Pyrolite [McDonough and Sun, 1995, Palme and O'Neill, 2016, Workman and Hart, 2005] provides a uniform chemical model for the Earth's mantle that approximates its mineralogical state, rheology and dynamics [Akaogi, 2007, Frost, 2008, Schubert et al., 2009b, Weidner, 1985]. With a silica mole fraction, $x(\text{SiO}_2) \sim 0.4$ (Table 5.1), the phase assemblages are governed by the coexistence of Mg_2SiO_4 - and MgSiO_3 -based minerals at upper mantle conditions [Frost, 2008], replaced by perovskite- and oxide-dominated assemblages in the lower mantle [Irifune and Tsuchiya, 2015]. For geophysical applications, the pyrolite bulk composition has typically been reduced to a six-component system $\text{Na}_2\text{O}-\text{CaO}-\text{FeO}-\text{MgO}-\text{Al}_2\text{O}_3-\text{SiO}_2$ (Table 5.1), comprising $\sim 99 \text{ mol}\%$ of the mantle geochemical estimate. While Cr_2O_3 is more abundant than Na_2O in the pyrolite models by McDonough and Sun [1995] and Workman and Hart [2005], the inclusion of a monovalent – rather than another trivalent – cation in the composition is important in terms of mineralogy. With the EOS code, and using the thermodynamic database of Stixrude and Lithgow-Bertelloni [2011], we explore the sensitivity of phase relations to chemical composition by sequentially increasing the number of components from the binary $\text{MgO}-\text{SiO}_2$ (MS) to the six-component $\text{Na}_2\text{O}-\text{CaO}-\text{FeO}-\text{MgO}-\text{Al}_2\text{O}_3-\text{SiO}_2$ (NCFMAS) system (Table 5.1). We evaluate phase assemblages, phase proportions (Figure 5.1) and chemical composition along isentropes with a potential temperature of 1600 K as a proxy for the mantle geotherm (*cf.* Section 6.1) and present complete phase diagrams for the MS, FMS, CFMS, FMAS, CFMAS and NCFMAS systems (Figures 5.2-5.7). Where the isentropes pass through a small number of grid cells on either side of a phase boundary, the composition curves can occasionally exhibit oscillations (e.g., Figure 5.1 around 18 GPa).

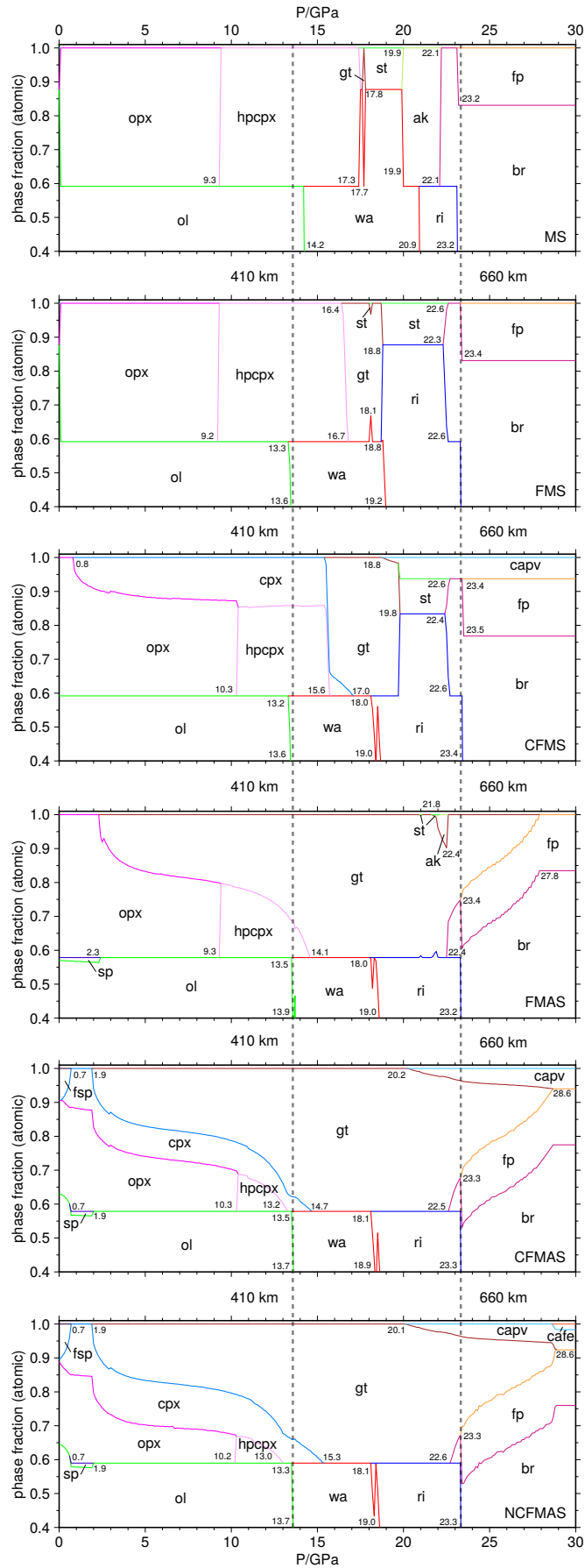


Figure 5.1: Phase fractions for the reduced pyrolite compositions (Table 5.1), for MS, FMS, CFMS, FMAS, CFMAS and NCFMAS systems (top to bottom) along 1600 K isentropes, computed with the thermodynamic database of [Stixrude and Lithgow-Bertelloni \[2011\]](#). Stable phases are indicated with the abbreviations of Table B.2. The phase fraction fields start at 0.4, with the remaining portion occupied by the phase at the bottom of each panel. Numbers in the panels indicate phase transition pressures (GPa). For divariant and multi-variant phase transitions, the onset and completion of a phase transition is indicated. Numbers at the bottom of each panel indicate the completion of the phase transition, representing phase fraction 0.0 (rather than 0.4 as the location suggests). Pressures of the 410 km and 660 km discontinuities are indicated by vertical dashed lines.

Table 5.1: Chemical bulk compositions used in the computation of phase assemblages. Different lithologies are for the differentiated slab, dry bulk oceanic crust (BOC) and dry harzburgite for the depleted mantle (DM) [[Chemia et al., 2015](#)]. For the primitive mantle, pyrolite from [Workman and Hart \[2005\]](#), is reduced to a five component system (NCFMAS). For further reduced compositions, Na₂O is removed and the composition renormalized (CFMAS). For the FMAS composition, the CaO component is distributed to the other divalent oxides MgO and FeO, maintaining their ratio. For the other four component system CFMS, trivalent Al₂O₃ is replaced by an equal amount of SiO₂ and the divalent oxides MgO, FeO and CaO, again maintaining the ratios among the latter. For the FMS system, the CaO component of CFMS is distributed between MgO and FeO such that their ratio remains the same. For the MS system, FeO is completely replaced by MgO.

Component	BOC	DM	NCFMAS	CFMAS	CFMS	FMAS	FMS	MS
	mol%	mol%	mol%	mol%	mol%	mol%	mol%	mol%
MgO	15.11	56.17	49.85	49.91	50.85	52.52	53.52	60.14
FeO	6.59	5.71	6.17	6.18	6.29	6.51	6.62	—
CaO	14.39	0.99	2.94	2.94	3.00	—	—	—
Al ₂ O ₃	10.39	0.59	2.22	2.22	—	2.22	—	—
Na ₂ O	1.76	0.00	0.11	—	—	—	—	—
SiO ₂	51.76	36.54	38.71	38.75	39.86	38.75	39.86	39.86

5.1.1 MS System

For the Mg_2SiO_4 component in the MS system, the model of [Stixrude and Lithgow-Bertelloni \[2011\]](#) predicts phase transitions from olivine to wadsleyite and from wadsleyite to ringwoodite with positive Clapeyron slopes (Figures 5.1 and 5.2). Ringwoodite breaks down to a lower mantle phase assemblage of bridgmanite and periclase with a negative Clapeyron slope. The predictions on phase transition locations and Clapeyron slopes are in good quantitative agreement with experiments [[Akaogi, 2007](#), [Inoue et al., 2006](#), [Ishii et al., 2011](#), [Katsura et al., 2004](#), [Morishima et al., 1994](#), [Suzuki et al., 2000](#)]. For the pyroxene-based, MgSiO_3 -dominated assemblages, the phase diagram shown in Figure 4.5 implies that, along the isentrope, orthoenstatite transforms to high-pressure clinoenstatite (Figure 5.2). After intersecting the majorite stability field (Figure 4.5), high-pressure clinopyroxene dissociates to wadsleyite and stishovite, and these subsequently recombine to form akimotoite. The transition of akimotoite to bridgmanite is lower by ~ 1 GPa than the ringwoodite formation (Fig-

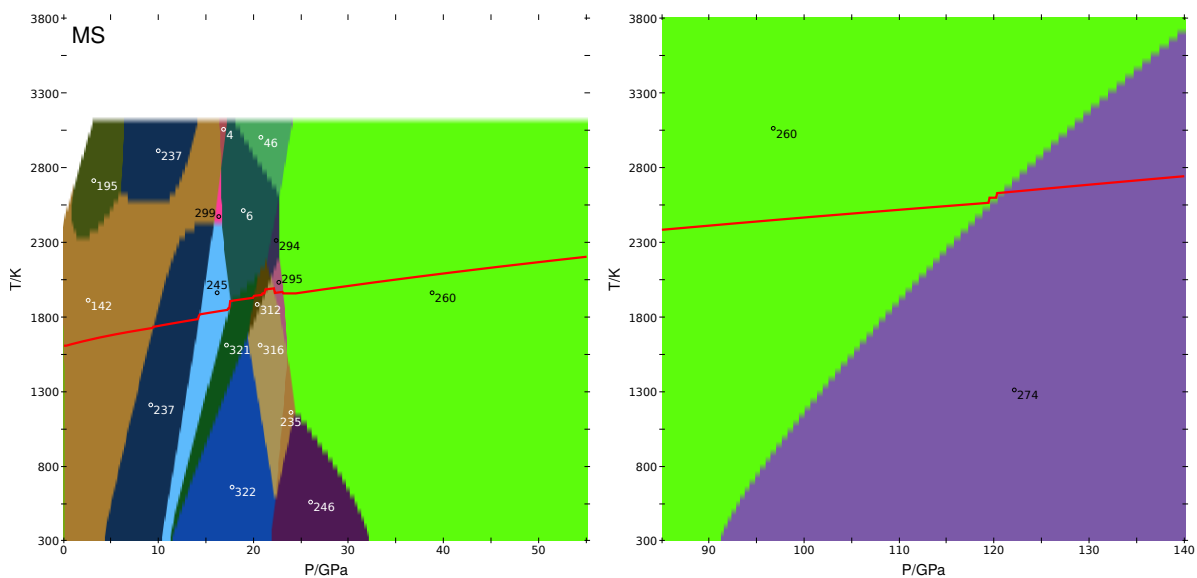


Figure 5.2: Phase diagrams computed with EoS using the model parameters from [Stixrude and Lithgow-Bertelloni \[2011\]](#) for MS composition (Table 5.1) as a function of P and T with 0.1 GPa and 50 K grid spacing. Panel (a) shows the P -range 0 – 55 GPa (surface to lower mantle), panel (b) the P -range 85 – 140 GPa (lowermost mantle). An isentrope computed with predicted material properties, starting with 1600 K at 0 GPa, is shown on top of the phase diagrams as a red line. Numbered stability fields (Table B.3; for abbreviations, see Table B.2) contain the following phase assemblages for the low- P region (panel a): (142) ol+opx, (237) ol+hpcpx, (245) wa+hpcpx, (321) wa+st, (322) ri+st, (316) ri+ak, (235) ak+fp, (246) st+fp, (260) br+fp, (195) ol+cpx, (4) ol+gt, (299) wa+opx (6) wa+gt, (46) gt+fp, (312) wa+ak, (294) wa+br, (295) ri+br. Critical phase transitions for Mg_2SiO_4 along the isentrope are ol \rightarrow wa (237 \rightarrow 245 at 14.3 GPa and 1710 K), wa \rightarrow ri (312 \rightarrow 316; 21.2 GPa, 1950 K) and the breakdown ri \rightarrow br+pc (295 \rightarrow 260; 23.2 GPa, 1940 K). In the MgSiO_3 -based system the following transitions occur along the isentrope: opx \rightarrow hpcpx (142 \rightarrow 237; 9.4 GPa, 1720 K), a dissociation hpcpx \rightarrow wa+st (245 \rightarrow 321; 17.6 GPa, 1860 K), the recombination wa+st \rightarrow ak (321 \rightarrow 312; 20.0 GPa, 1920 K) and ak \rightarrow br (316 \rightarrow 295; 22.3 GPa, 1980 K). In the high- P region (panel b) the following phase assemblages occur: (260) br+fp, (274) ppv+fp, with the transition along the mantle isentrope occurring at 120.6 GPa and 2630 K.

ure 5.1). At higher T , majorite garnet transforms to bridgmanite directly with a positive Clapeyron slope, as also determined in experiments [e.g., Ishii et al., 2011].

At lowermost mantle pressures, bridgmanite is replaced by post-perovskite with a steep positive Clapeyron slope as already shown in Figure 4.5.

5.1.2 FMS System

With the addition of more chemical components, (i) new phases and their stability fields occur, (ii) new endmembers are introduced and form mineral solutions whose stability fields generally expand, and/or (iii) the variance of mineral assemblages increases, resulting in binary or higher-order phase loops which allow the coexistence of phases previously separated by sharp boundaries. For a molar ratio $\text{Fe}/(\text{Fe}+\text{Mg})$

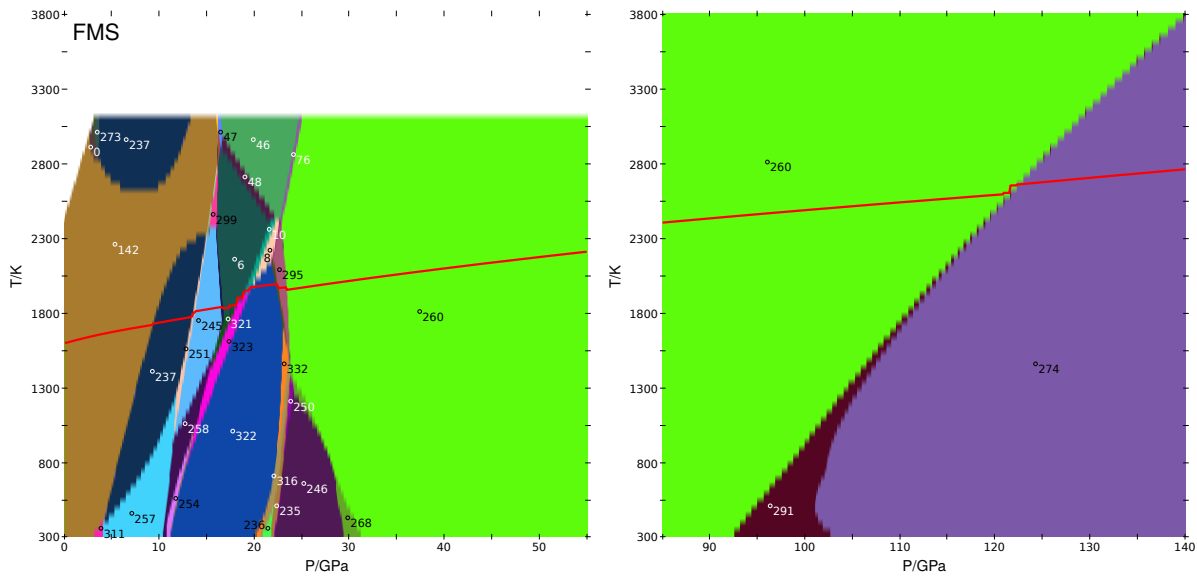


Figure 5.3: Phase diagrams computed with EoS using model parameters from [Stixrude and Lithgow-Bertelloni \[2011\]](#) for FMS composition (Table 5.1) as a function of P and T with 0.1 GPa and 50 K grid spacing. Panel (a) shows the P -range 0 – 55 GPa (surface to lower mantle), panel (b) shows the P -range 85 – 140 GPa (lowermost mantle). An isentrope computed with predicted material properties, starting with 1600 K at 0 GPa is shown on top of the phase diagrams as a red line. Numbered stability fields (Table B.3; for abbreviations, see Table B.2) contain the following phase assemblages for the low- P region (panel a): (0) ol+opx+cpx, (6) wa+gt, (8) ri+gt, (10) wa+ri+gt, (46) gt+fp, (47) ol+gt+fp, (48) wa+gt+fp, (76) gt+br+fp, (142) ol+opx, (235) ak+fp, (236) ri+ak+fp, (237) ol+hpcpx, (245) wa+hpcpx, (246) st+fp, (251) ol+wa+hpcpx, (254) ri+hpcpx, (257) ol+ri+hpcpx, (258) wa+ri+hpcpx, (260) br+fp, (268) st+br+fp, (273) ol+cpx+hpcpx, (295) ri+br, (299) wa+opx, (311) ol+ri+opx, (316) ri+ak, (321) wa+st, (322) ri+st, (323) wa+ri+st, (332) ri+ak+st. Important phase transitions for the Mg_2SiO_4 -based minerals along the isentrope are ol \rightarrow wa (237 \rightarrow 245 at 13.4 GPa and 1780 K), wa \rightarrow ri (6 \rightarrow (10) \rightarrow 322 at 19.1 GPa and 1930 K), ri \rightarrow br+pc (322 \rightarrow (295) \rightarrow 260 at 23.5 GPa and 1940 K). Phase fields given in parentheses indicate coexistence regions; in those cases, P and T refer to conditions at the center of the intersection between isentrope and coexistence region. In the MgSiO_3 -based system, relevant phase transitions along the isentrope are opx \rightarrow hpcpx (142 \rightarrow 237 at 9.4 GPa and 1710 K), and hpcpx \rightarrow wa + st (245 \rightarrow 321 at 17.9 GPa and 1840 K). In the high- P region (panel b) the following phase assemblages occur: (260) br+fp, (274) ppv+fp, (291) br+ppv+fp. The isentrope crosses the br \rightarrow ppv phase boundary (260 \rightarrow 274) at 122.3 GPa and 2650 K.

= 0.11 in bulk pyrolite and the reduced compositions (Table 5.1), the binary phase field between olivine and wadsleyite in the FMS system is predicted to be narrow along the isentrope, and the phase transition shifts to slightly lower pressure relative to the MS system (Figures 4.9 and 5.1). By contrast, the coexistence region between wadsleyite and ringwoodite is in the range of $\sim 1\text{GPa}$, with an overall reduction of the wadsleyite stability field (Figures 5.1, 5.2 and 5.3). Dissociation of ringwoodite occurs through a narrow coexistence region in which ringwoodite and stishovite recombine to form bridgmanite.

For the MgSiO_3 -dominated minerals, the orthopyroxene-high-pressure clinopyroxene transition is not affected by the addition of FeO (Figures 5.1 and 5.3), but high-pressure clinopyroxene transforms to garnet at lower pressure, reflecting a slight increase of the garnet stability field at the expense of akimotoite (Figure 5.8). In the presence of FeO, garnet breaks down to ringwoodite and stishovite, from which bridgmanite forms directly, without intermediate akimotoite stability; this prediction of the model by [Stixrude and Lithgow-Bertelloni \[2011\]](#) is in disagreement with experiments [[Ito and Yamada, 1982](#), [Ohtani et al., 1991](#)] that show a transition from akimotoite to bridgmanite.

In the lowermost mantle, the post-perovskite transition is shifted to slightly higher pressure in the FMS system and occurs nearly univariantly; only for $T < 2000\text{K}$ (Figure 5.3) a significant phase coexistence region opens between bridgmanite and post-perovskite. In the assessment of [Stixrude and Lithgow-Bertelloni \[2011\]](#), the Clapeyron slope of the transition does not change relative to the MS system, although experiments suggest only half the value [[Catalli et al., 2009](#)].

5.1.3 CFMS System

In the four-component system CFMS, with CaO added, clinopyroxene, with endmembers diopside and hedenbergite (Table B.2), occurs as a new phase in the assemblage (Figures 5.1 and 5.4). Clinopyroxene coexists with orthopyroxene, high-pressure clinopyroxene and garnet up to pressures of the transition zone. The incorporation of the Ca-bearing constituents in clinopyroxene significantly reduces the orthopyroxene and high-pressure clinopyroxene stability at low and high pressures, respectively, relative to the FMS system (Figure 5.1). In the thermodynamic database of [Stixrude and Lithgow-Bertelloni \[2011\]](#), clinopyroxene has multiple Ca-bearing endmembers while high-pressure clinopyroxene has none, favoring stability of the former phase. In the lower part of the transition zone, Ca-perovskite appears and becomes the first lower-mantle phase to exsolve from the garnet solid solution (Figures 5.1 and 5.4), as already seen in the diopside-enstatite phase diagram (Figure 4.10) and consistent with a decreasing Ca-solubility in garnet as a function of P [[Saikia et al., 2008](#)].

As there is no Ca-bearing endmember in the bridgmanite and post-perovskite solutions, this transition does not change relative to FMS.

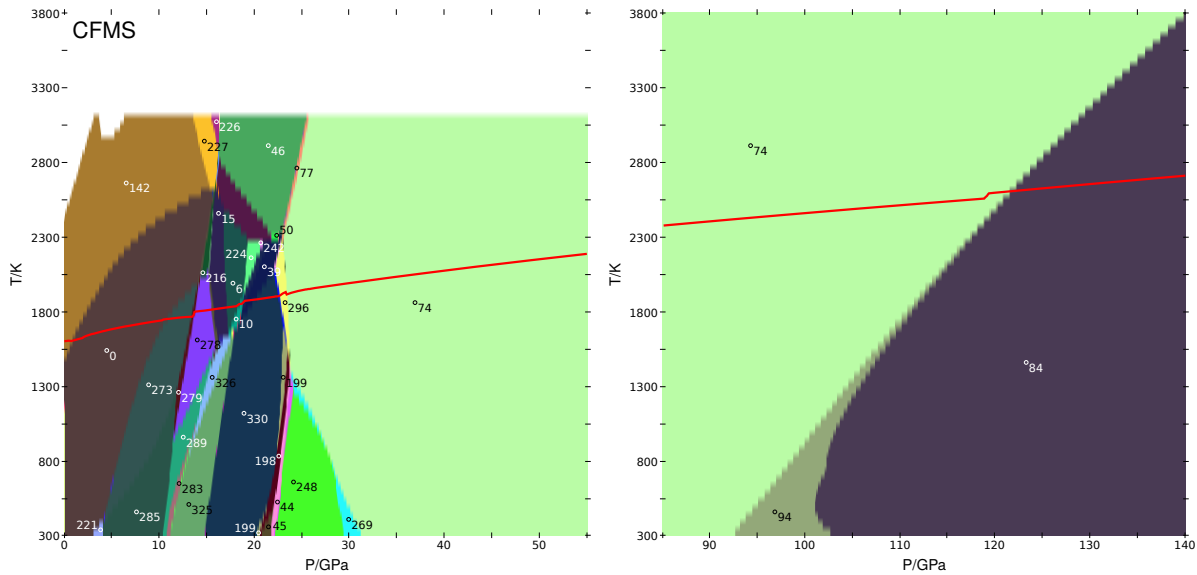


Figure 5.4: Phase diagrams computed with EoS using the parameters from [Stixrude and Lithgow-Bertelloni \[2011\]](#) for CFMS composition (Table 5.1) as a function of P and T with 0.1 GPa and 50 K grid spacing. Panel (a) shows the P -range 0 – 55 GPa (surface to lower mantle), panel (b) shows the P -range 85 – 140 GPa (lowermost mantle). An isentrope computed with predicted material properties for the CFMAS system (Figure 5.6), starting with 1600 K at 0 GPa is shown on top of the phase diagrams as a red line. Numbered stability fields (Table B.3; for abbreviations, see Table B.2) contain the following phase assemblages for the low- P region (panel a): (0) ol+opx+cpx, (6) wa+gt, (10) wa+ri+gt, (15) wa+cpx+gt, (39) ri+capv+gt, (44) capv+ak+fp, (45) ri+capv+ak+fp, (46) gt+fp, (50) ri+gt+fp, (74) capv+br+fp, (77) capv+gt+br+fp, (142) ol+opx, (198) ri+capv+ak, (199) ri+capv+ak+st, (216) wa+opx+cpx, (221) ol+ri+opx+cpx, (224) wa+capv+gt, (226) opx+fp, (227) ol+opx+fp, (242) wa+capv+gt+fp, (248) capv+st+fp, (269) capv+st+br+fp, (273) ol+cpx+hpcpx, (278) wa+cpx+hpcpx, (279) ol+wa+cpx+hpcpx, (283) ri+cpx+hpcpx, (285) ol+ri+cpx+hpcpx, (289) wa+ri+cpx+hpcpx, (296) ri+capv+br, (325) ri+cpx+st, (326) wa+ri+cpx+st, (330) ri+capv+st. Along the isentrope the following transitions occur in the Mg_2SiO_4 -based system: ol \rightarrow wa (273 \rightarrow (279) \rightarrow 278 at 13.6 GPa and 1770 K), wa \rightarrow ri (6 \rightarrow (10) \rightarrow 39 at 18.5 GPa and 1840 K), ri+st \rightarrow br+fp (330 \rightarrow (296) \rightarrow 74 at 22.9 GPa and 1920 K). In the $MgSiO_3$ -based system the following transitions occur: opx \rightarrow cpx+hpcpx (142 \rightarrow (0) \rightarrow 273 between 1.0 GPa and 10.5 GPa, 1600 K and 1730 K), hpcpx \rightarrow gt (278 \rightarrow 15 at 15.6 GPa and 1790 K), cpx \rightarrow gt (15 \rightarrow 6 at 17.0 GPa and 1820 K), gt \rightarrow capv+st (10 \rightarrow (39) \rightarrow 330 between 18.7 GPa and 19.9 GPa, 1860 K and 1870 K). In the high- P region (panel b) the following phase assemblages occur: (74) capv+br+fp, (84) capv+ppv+fp, (94) capv+br+ppv+fp. The isentrope intersects the br \rightarrow ppv phase boundary (74 \rightarrow 84) at 121.8 GPa and 2610 K. Phase fields given in parentheses indicate coexistence regions; in those cases, P and T refer to conditions at the boundaries or the center of the intersection between isentrope and coexistence region.

5.1.4 FMAS System

In the other four-component system considered, FMAS, Al_2O_3 leads to new phases being formed at low P , but tends to become a substituent in ferromagnesian silicates at higher P . $(\text{Mg,Fe})\text{Al}_3\text{O}_4$ spinel occurs as an Al-bearing phase in the mantle assemblage up to 2.5 GPa (Figures 5.1 and 5.5), which agrees well with the location of the spinel-lherzolite to garnet-lherzolite transition in the CMAS system [Klemme and O'Neill, 2000, Ziberna et al., 2013]. Through the addition of pyrope and almandine endmembers (Table B.2), the garnet stability range extends dramatically (Figures 5.1, 5.5 and 5.8) at the expense of high-pressure clinopyroxene (low P) and ringwoodite and stishovite as well as bridgmanite (high P). The fraction of garnet in the phase

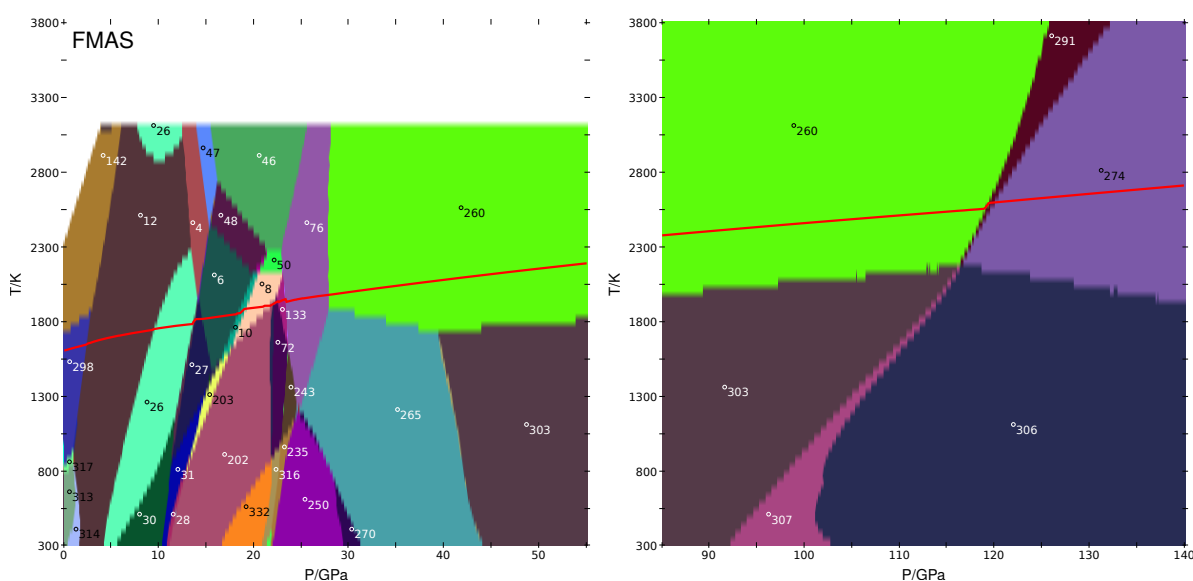


Figure 5.5: Phase diagrams computed with EoS using the model parameters from Stixrude and Lithgow-Bertelloni [2011] for FMAS composition (Table 5.1) as a function of P and T with 0.1 GPa and 50 K grid spacing. Panel (a) shows the P -range 0 – 55 GPa (surface to lower mantle), panel (b) the P -range 85 – 140 GPa (lowermost mantle). An isentrope computed with predicted material properties, starting with 1600 K at 0 GPa, is shown on top of the phase diagrams as a red line. Numbered stability fields (Table B.3; for abbreviations, see Table B.2) contain the following phase assemblages for the low- P region (panel a): (4) ol+gt, (6) wa+gt, (8) ri+gt, (10) wa+ri+gt, (12) ol+opx+gt, (26) ol+hpcpx+gt, (27) wa+hpcpx+gt, (28) ri+hpcpx+gt, (30) ol+ri+hpcpx+gt, (31) wa+ri+hpcpx+gt, (46) gt+fp, (47) ol+gt+fp, (48) wa+gt+fp, (50) ri+gt+fp, (72) ri+ak+gt, (76) gt+br+fp, (133) ri+gt+br, (142) ol+opx, (202) ri+gt+st, (203) wa+ri+gt+st, (235) ak+fp, (243) ak+gt+fp, (250) ak+st+fp, (260) br+fp, (265) ak+br+fp, (270) ak+st+br+fp, (298) sp+ol+opx, (303) br+fp+cf, (313) ol+opx+ky, (314) ol+opx+gt+ky, (316) ri+ak, (317) ol+opx+ak, (332) ri+ak+st. Along the isentrope the following transitions occur in the Mg_2SiO_4 -based system: ol \rightarrow wa (26 \rightarrow 27 at 13.7 GPa and 1790 K), wa \rightarrow ri (6 \rightarrow (10) \rightarrow 8; 18.7 GPa, 1860 K), ri \rightarrow br+fp (8 \rightarrow (133) \rightarrow 76 between 21.7 GPa and 23.3 GPa, 1910 K and 1940 K). In the MgSiO_3 -based system the following transitions occur: sp \rightarrow gt (298 \rightarrow 12; 2.6 GPa, 1640 K), opx \rightarrow hpcpx (12 \rightarrow 26; 9.6 GPa, 1740 K), hpcpx \rightarrow gt (27 \rightarrow 6; 14.6 GPa, 1810 K), gt \rightarrow br+fp (8 \rightarrow (133, 76) \rightarrow 260 between 21.7 GPa and 27.7 GPa, 1910 K and 1970 K). In the high- P region (panel b) the following phase assemblages occur: (260) br+fp, (274) ppv+fp, (291) br+ppv+fp, (303) br+fp+cf, (306) ppv+fp+cf, (307) br+ppv+fp+cf. The isentrope intersects the br \rightarrow ppv phase boundary (260 \rightarrow (291) \rightarrow 274) at 119.6 GPa and 2560 K. Phase fields given in brackets indicate coexistence regions; in those cases, P and T refer to conditions at the boundaries or the center of the intersection between isentrope and coexistence region.

assemblage increases continuously with P as the pyroxene component is consumed (Figure 5.1). Garnet stability extends significantly beyond pressures of the 660 km seismic discontinuity and the ringwoodite breakdown (Figures 5.1, 5.5 and 5.8).

In the lowermost mantle, the addition of Al_2O_3 stabilizes the post-perovskite phase at the expense of bridgmanite (Figure 5.5), moving the transition to slightly lower pressure. Also, the coexistence region of bridgmanite and post-perovskite widens, both at low and high temperature, but it remains relatively narrow in the T -range of 2000 – 2500 K.

5.1.5 CFMAS System

The five-component system CFMAS (Figures 5.1 and 5.6) shows the combined characteristics of the FMAS and CFMS assemblages and their solutions, as well as several

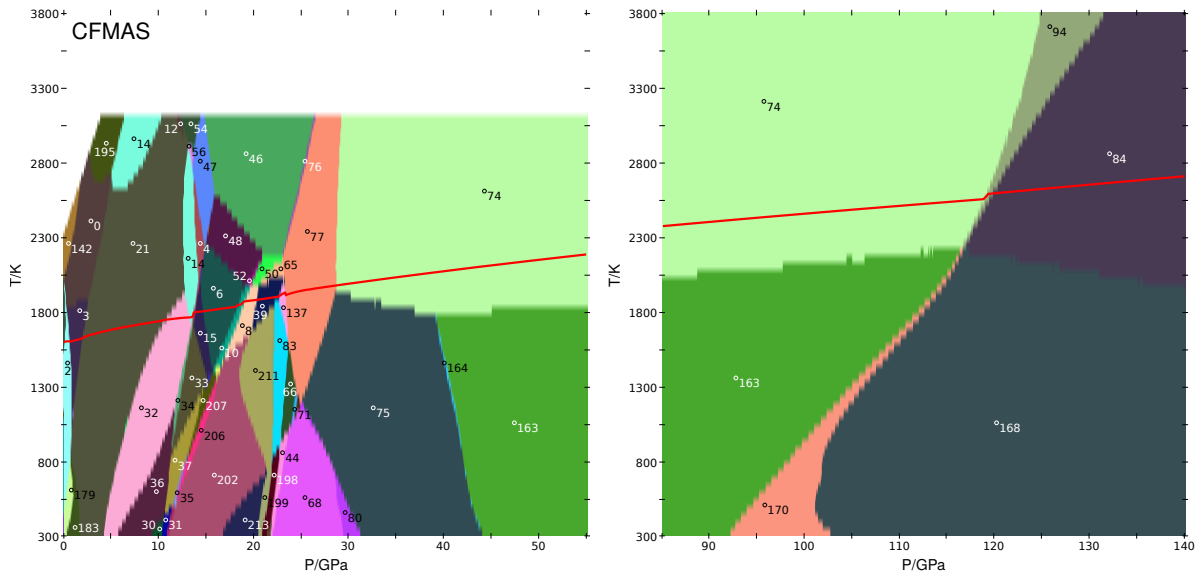


Figure 5.6: Phase diagrams computed with EoS using the parameters from [Stixrude and Lithgow-Bertelloni \[2011\]](#) for CFMAS composition (Table 5.1) as a function of P and T with 0.1 GPa and 50 K grid spacing. Panel (a) shows the P -range 0 – 55 GPa (surface to lower mantle), panel (b) shows the P -range 85 – 140 GPa (lowermost mantle). An isentrope computed with predicted material properties, starting with 1600 K at 0 GPa is shown on top of the phase diagrams as a red line. Numbered stability fields (Table B.3; for abbreviations, see Table B.2) contain the following phase assemblages for the low- P region (panel a): (0) ol+opx+cpx, (2) fsp+ol+opx+cpx, (3) sp+ol+opx+cpx, (4) ol+gt, (6) wa+gt, (8) ri+gt, (10) wa+ri+gt, (12) ol+opx+gt, (14) ol+cpx+gt, (15) wa+cpx+gt, (21) ol+opx+cpx+gt, (30) ol+ri+hpcpx+gt, (31) wa+ri+hpcpx+gt, (32) ol+cpx+hpcpx+gt, (33) wa+cpx+hpcpx+gt, (34) ol+wa+cpx+hpcpx+gt, (35) ri+cpx+hpcpx+gt, (36) ol+ri+cpx+hpcpx+gt, (37) wa+ri+cpx+hpcpx+gt, (39) ri+capv+gt, (44) capv+ak+fp, (46) gt+fp, (47) ol+gt+fp, (48) wa+gt+fp, (50) ri+gt+fp, (52) wa+ri+gt+fp, (54) ol+opx+gt+fp, (56) ol+cpx+gt+fp, (65) ri+capv+gt+fp, (66) capv+ak+gt+fp, (68) capv+ak+st+fp, (71) capv+ak+gt+st+fp, (74) capv+br+fp, (75) capv+ak+br+fp, (76) gt+br+fp, (77) capv+gt+br+fp, (80) capv+ak+st+br+fp, (83) ri+capv+ak+gr+fp, (137) ri+capv+gt+br, (142) ol+opx, (163) capv+br+fp+cf, (164) capv+ak+br+fp+cf, (179) ol+opx+cpx+ky, (183) ol+opx+cpx+gt+ky, (195) ol+cpx, (198) ri+capv+ak, (199) ri+capv+ak+st, (202) ri+gt+st, (206) ri+cpx+gt+st, (207) wa+ri+cpx+gt+st, (211) ri+capv+gt+st, (213) ri+ak+gt+st. Along the isentrope the following transitions occur in the Mg_2SiO_4 -based system: ol \rightarrow wa (14 \rightarrow 15 at 13.7 GPa and 1770 K), wa \rightarrow ri (6 \rightarrow (10) \rightarrow 8 at 18.7 GPa and 1850 K), ri \rightarrow br+fp (137 \rightarrow 77 at 23.4 GPa and 1930 K). In the MgSiO_3 -based system the following transitions occur: fsp \rightarrow sp (2 \rightarrow 3 at 0.7 GPa and 1600 K), sp \rightarrow gt (3 \rightarrow 21 at 1.9 GPa and 1630 K), opx+cpx \rightarrow cpx+hpcpx+gt (3 \rightarrow (21) \rightarrow 32 between 1.9 GPa and 10.7 GPa, 1630 K and 1740 K), hpcpx \rightarrow gt (32 \rightarrow 14 at 13.2 GPa and 1750 K), cpx \rightarrow gt (15 \rightarrow 6 at 14.7 GPa and 1800 K), gt \rightarrow capv+br (8 \rightarrow (39, 137, 77) \rightarrow 74 between 20.4 GPa and 28.7 GPa, 1890 K and 1980 K) via capv in (8 \rightarrow 39 at 20.3 GPa and 1880 K), br in (39 \rightarrow 137 at 22.6 GPa and 1900 K) and gt out (77 \rightarrow 74 at 28.7 GPa and 1970 K). In the high- P region (panel b) the following phase assemblages occur: (74) capv+br+fp, (84) capv+ppv+fp, (94) capv+br+ppv+fp, (163) capv+br+fp+cf, (168) capv+ppv+fp+cf, (170) capv+br+ppv+fp+cf. The isentrope intersects the br \rightarrow ppv phase boundary (74 \rightarrow (94) \rightarrow 84 at 119.1 GPa and 2570 K). Phase fields given in parentheses indicate coexistence regions; in those cases, P and T refer to conditions at the boundaries or the center of the intersection between isentrope and coexistence region.

new phases. Below 1 GPa, feldspar forms as anorthite (Table B.2). With increasing P , anorthite is predicted to transform to a spinel-bearing assemblage, before the transformation to a garnet-bearing assemblage occurs, similar to the CMAS system (Figures 5.1 and 5.5). The anorthite stability range in the CFMAS system predicted by the model of [Stixrude and Lithgow-Bertelloni \[2011\]](#) is smaller than that established for pure $\text{CaAl}_2\text{Si}_2\text{O}_8$ [e.g., [Koziol and Newton, 1988](#)] or in tholeiitic basalts [[O'Brien and Rötzler, 2003](#)], however. In addition, in both of these studies, feldspar transforms to a garnet-bearing assemblage directly. The addition of Ca-Al-endmembers in both clinopyroxene (Ca-tschermak) and garnet (grossular) (Table B.2) does not alter the phase proportions between garnet and any of the pyroxene solid solutions compared to FMAS (Figure 5.1).

Formation of Ca-perovskite in CFMAS initiates at slightly higher pressure than in the CFMS system (Figures 5.1, 5.4 and 5.6), and bridgmanite formation occurs from garnet, in good agreement with experiments on pyrolite [[Ishii et al., 2011](#)].

5.1.6 NCFMAS System

In the full pyrolite composition (NCFMAS system, Table 5.1), the jadeite endmember stabilizes clinopyroxene at the expense of garnet, both in terms of an expansion of the stability field (Figures 5.1, 5.7 and 5.8) and phase proportions (Figure 5.1). A Ca-

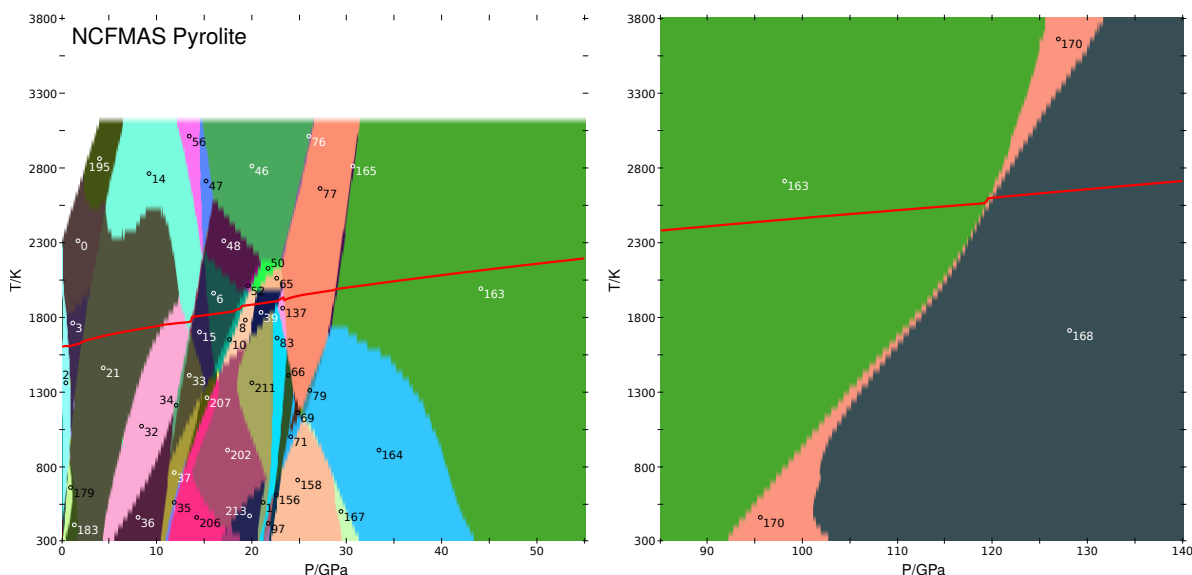


Figure 5.7: Phase diagrams computed with EoS using the model parameters from [Stixrude and Lithgow-Bertelloni \[2011\]](#) for pyrolite composition (Table 5.1) as a function of P and T with 0.1 GPa and 50 K grid spacing. Panel (a) shows the P -range 0 – 55 GPa (surface to lower mantle), panel (b) the P -range 85 – 140 GPa (lowermost mantle). An isentrope computed with predicted material properties, starting with 1600 K at 0 GPa, is shown on top of the phase diagrams as a red line. Numbered stability fields (Table B.3; for abbreviations, see Table B.2) contain the following phase assemblages for the low- P region (panel a): (0) ol+opx+cpx, (1) ri+capv+ak+gt+st, (2) fsp+ol+opx+cpx, (3) sp+ol+opx+cpx, (6) wa+gt, (8) ri+gt, (10) wa+ri+gt, (14) ol+cpx+gt, (15) wa+cpx+gt, (21) ol+opx+cpx+gt, (32) ol+cpx+hpcpx+gt, (33) wa+cpx+hpcpx+gt, (34) ol+wa+cpx+hpcpx+gt, (35) ri+cpx+hpcpx+gt, (36) ol+ri+cpx+hpcpx+gt, (37) wa+ri+cpx+hpcpx+gt, (39) ri+capv+gt, (46) gt+fp, (47) ol+gt+fp, (48) wa+gt+fp, (50) ri+gt+fp, (52) wa+ri+gt+fp, (56) ol+cpx+gt+fp, (65) ri+capv+gt+fp, (66) capv+ak+gt+fp, (69) capv+gt+st+fp, (71) capv+ak+gt+st+fp, (76) gt+br+fp, (77) capv+gt+br+fp, (79) capv+ak+gt+br+fp, (83) ri+capv+ak+gt, (97) ri+capv+ak+cf, (137) ri+capv+gt+br, (156) capv+ak+fp+cf, (157) ri+capv+ak+fp+cf, (158) capv+ak+st+fp+cf, (163) capv+br+fp+cf, (164) capv+ak+br+fp+cf, (165) capv+gt+br+fp+cf, (167) capv+ak+st+br+fp+cf, (179) ol+opx+cpx+ky, (183) ol+opx+cpx+gt+ky, (195) ol+cpx, (202) ri+gt+st, (203) wa+ri+gt+st, (206) ri+cpx+gt+st, (207) wa+ri+cpx+gt+st, (211) ri+capv+gt+st, (213) ri+ak+gt+st, (214) ri+cpx+ak+gt+st. Along the isentrope the following transitions occur in the Mg_2SiO_4 -based system: ol \rightarrow wa (14 \rightarrow 15 at 13.7 GPa and 1780 K), wa \rightarrow ri (6 \rightarrow (10) \rightarrow 8; 18.7 GPa, 1850 K), ri \rightarrow br+fp (137 \rightarrow 77; 23.3 GPa, 1920 K). In the MgSiO_3 -based system the following transitions occur: fsp \rightarrow sp (2 \rightarrow 3; 0.9 GPa, 1600 K), sp \rightarrow gt (3 \rightarrow 21; 2.1 GPa, 1630 K), opx+cpx \rightarrow cpx+hpcpx+gt (3 \rightarrow (21) \rightarrow 32 between 2.1 GPa and 10.5 GPa, 1630 K and 1740 K), hpcpx \rightarrow gt (32 \rightarrow 14; 13.0 GPa, 1750 K), cpx \rightarrow gt (15 \rightarrow 6; 15.5 GPa, 1820 K), gt \rightarrow capv+br+cf (8 \rightarrow (39, 137, 77, 165) \rightarrow 163 between 20.2 GPa and 28.9 GPa, 1880 K and 1990 K) via capv in (8 \rightarrow 39; 20.2 GPa, 1880 K), br in (39 \rightarrow 137; 22.7 GPa, 1910 K), cafe in (77 \rightarrow 165; 28.7 GPa, 1970 K) and gt out (165 \rightarrow 163; 28.9 GPa, 1990 K). In the high- P region (panel b) the following phase assemblages occur: (163) capv+br+fp+cf, (168) capv+ppv+fp+cf, (170) capv+br+ppv+fp+cf. The isentrope intersects the br \rightarrow ppv phase boundary (163 \rightarrow (170) \rightarrow 168) at 119.4 GPa and 2570 K. Phase fields given in parentheses indicate coexistence regions; in those cases, P and T refer to conditions at the boundaries or the center of the intersection between isentrope and coexistence region.

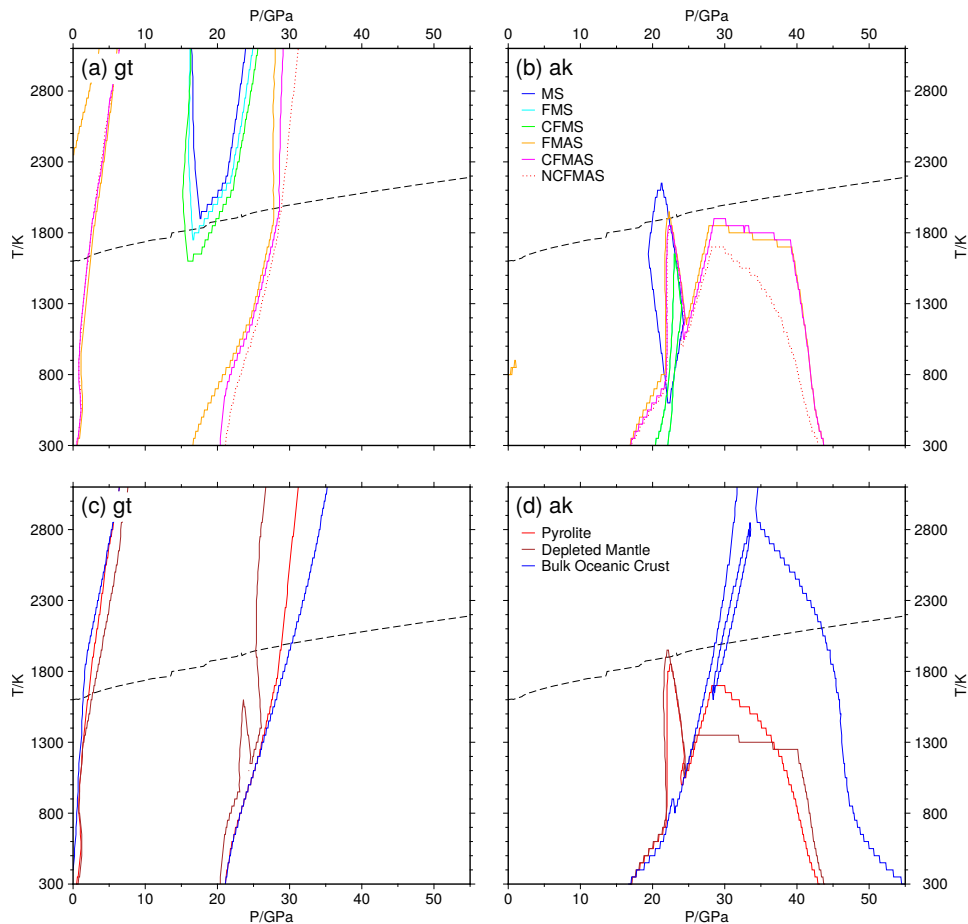


Figure 5.8: Stability fields of garnet (a and c) and akimotoite (b and d) shown by colored contour lines for different compositions: Panels (a) and (b) show results for the reduced pyrolite bulk compositions (Table 5.1) MS (blue), FMS (cyan), CFMS (green), FMAS (orange), CFMAS (magenta); results for NCFMAS (pyrolite) are plotted as dotted red lines. Panels (c) and (d) show stability fields for pyrolite (red), depleted mantle (brown) and bulk oceanic crust (blue) (Table 5.1). The adiabat for NCFMAS (pyrolite) with a potential temperature of 1600 K is displayed as a dashed black line in all panels.

ferrite-structured nepheline phase, NaAlSiO_4 (Table B.2), hosts Na_2O at lower mantle conditions [Irifune and Ringwood, 1993, Liu, 1977, Miyajima et al., 1999], forming from the jadeitic garnet component (Figures 5.1 and 5.7).

The lowermost mantle transition between bridgmanite and post-perovskite is largely unaffected by the addition of Na_2O when compared to the other Al_2O_3 -bearing composition (Figures 5.5, 5.6 and 5.7) and consistent with experiments on KLB-1 peridotite [Murakami and Hirose, 2005, Ono and Oganov, 2005].

5.2 Element Partitioning in Pyrolite

The chemical composition of solution phases is a result of the relative abundance of oxides in the bulk system, the extent of composition space accessible to each species, as well as element partitioning between coexisting phases. These effects are recorded in the variation of mineral compositions as a function of x , P and T as a

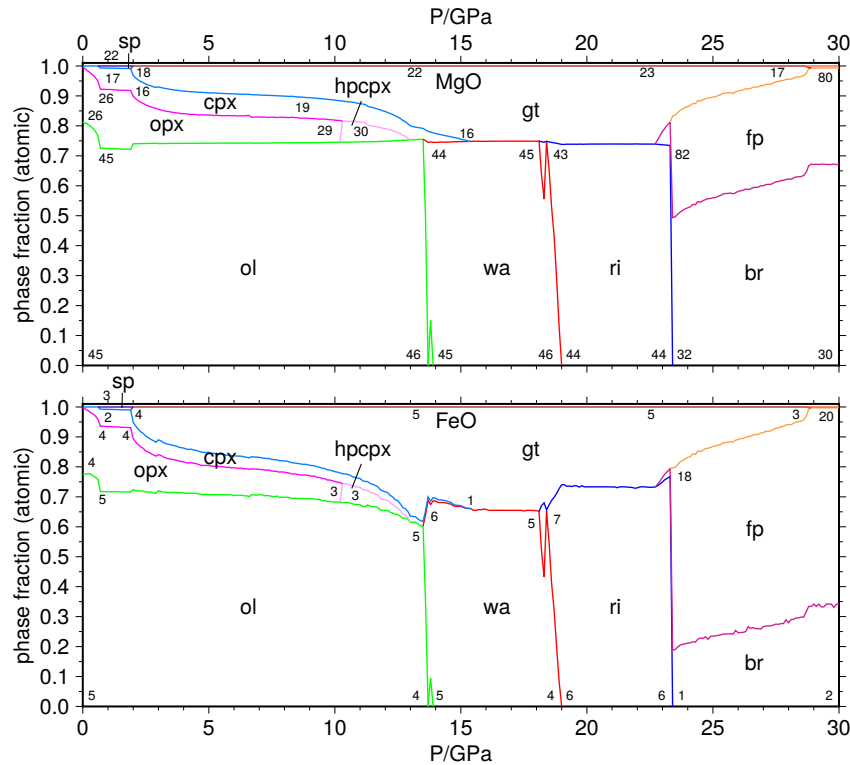


Figure 5.9: Phases hosting magnesium and iron for pyrolite bulk composition (Table 5.1), computed with the thermodynamic database of [Stixrude and Lithgow-Bertelloni \[2011\]](#). The graphs show the relative atomic amounts of stable phases (for abbreviations see Table B.2) containing magnesium (upper panel) and iron (lower panel) along the adiabat with a potential temperature of 1600 K. Labels in the panels indicate the content of Mg^{2+} and Fe^{2+} (number of cations per one hundred oxygen anions) for the different phases, respectively. A changing cation content is indicated by various numbers within a phase stability field.

sensitive measure of the accuracy of thermodynamic models and databases, and can be readily verified against experimental partitioning data. Here we explore element partitioning in NCFMAS pyrolite between the different phases that are stable along the 1600 K isentrope by predicting phase proportions (Figure 5.1), Mg-Fe budget and partitioning (Figure 5.9) as well as CaO , Al_2O_3 and Na_2O incorporation into coexisting phases (Figure 5.10). Element (cation) abundances are reported in number of cations per 100 oxygens (N cation/100 O) in a phase, in order to facilitate a comparison of the content between different minerals.

For the Mg_2SiO_4 - Fe_2SiO_4 phases, the Mg/Fe ratio follows the respective abundance of these elements in pyrolite, and differences in the Mg/Fe values between them are small. General trends that have emerged from experiments [e.g., [Frost, 2003b](#), [Ishii et al., 2011](#), [Kato et al., 2014](#)] and formulated in a thermodynamic model [[Frost, 2003a](#)] are reproduced. Pyroxene and garnet host smaller amounts of Mg and Fe due to the presence of Al_2O_3 , but are preferentially enriched in Fe over Mg (Figure 5.9).

In the lower mantle, FeO is predicted to strongly partition into ferropericlasite over bridgmanite, with an estimated distribution coefficient $K_{D,\text{Fe}/\text{Mg}}^{\text{br}/\text{fp}} = 0.25$. This is consistent with Mg- Fe^{2+} partitioning between bridgmanite and ferropericlasite established experimentally for both the FMS system and pyrolite at uppermost lower mantle conditions [e.g., [Prescher et al., 2014](#), [Sakai et al., 2009](#)]. By contrast, two features are

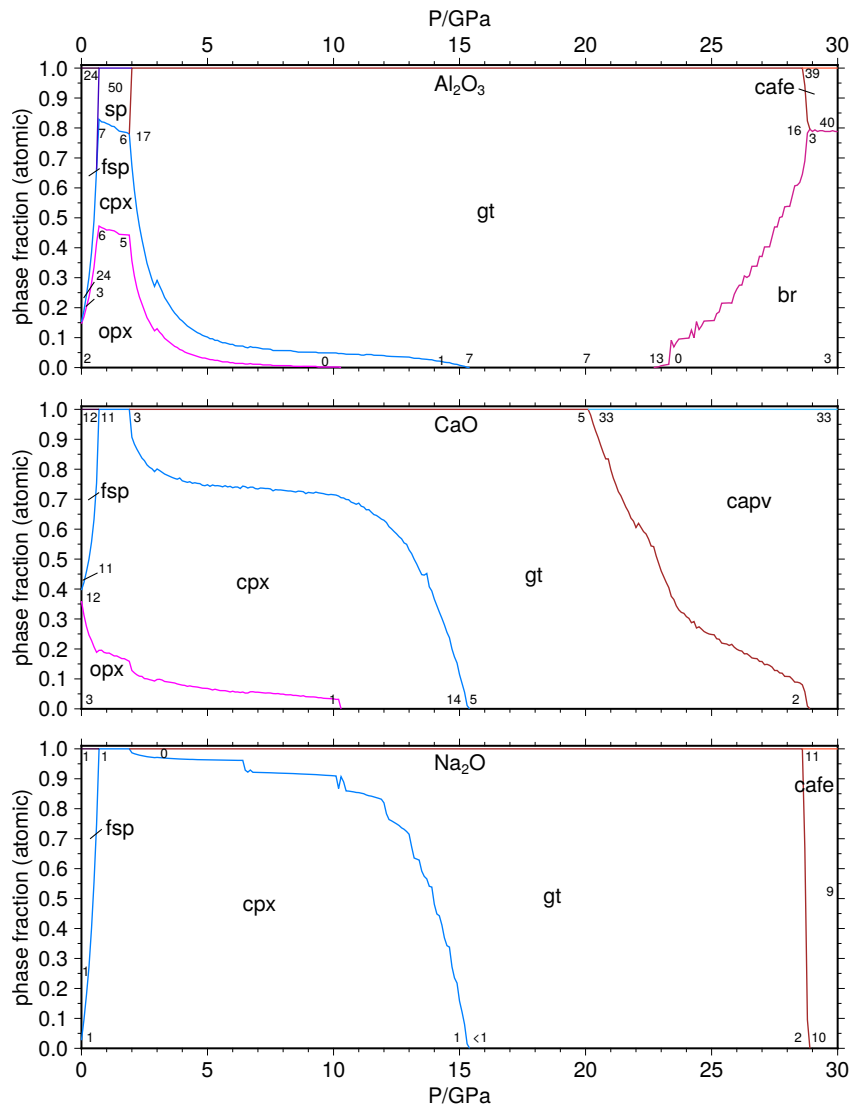


Figure 5.10: Phases hosting aluminum, calcium and sodium for pyrolite bulk composition (Table 5.1), computed with the thermodynamic database of [Stixrude and Lithgow-Bertelloni \[2011\]](#). The graphs show the relative atomic amounts of stable phases (for abbreviations see Table B.2) containing Al^{3+} , Ca^{2+} and Na^{+} (from top to bottom) along the adiabat with a potential temperature of 1600 K. Labels in the panels indicate the cation content of the different phases (number of cations per one hundred oxygen anions). A changing cation content is indicated by various numbers within a phase stability field.

not captured by the current thermodynamic datasets for the mantle [[Holland et al., 2013](#), [Stixrude and Lithgow-Bertelloni, 2011](#)]: (i) the spin crossover in both Fe-bearing bridgmanite and ferropericlase at pressures of the middle lower mantle [e.g., [Kantor et al., 2009](#), [McCammon et al., 2010](#)] appears to strongly affect the Mg-Fe partitioning coefficient of Fe^{2+} between bridgmanite and ferropericlase [[Prescher et al., 2014](#)]; (ii) the presence of Fe^{3+} , through a coupled substitution $\text{Fe}^{3+}\text{Al}^{3+}\text{-Mg}^{2+}\text{Si}^{4+}$ in bridgmanite, appears to exert an important influence on the Mg-Fe exchange with other phases [e.g., [Frost and Langenhorst, 2002](#), [Prescher et al., 2014](#)]. Representation of these features would require a thermodynamic model for high- and low-spin states in the Fe-bearing endmembers, and the calibration and addition of thermodynamic

data for Fe³⁺Al³⁺-bearing bridgmanite, respectively.

In the lowermost mantle, Mg-Fe partitioning between bridgmanite and ferropericlase, on the one hand, and post-perovskite and ferropericlase, on the other hand, does not change appreciably in the model of [Stixrude and Lithgow-Bertelloni \[2011\]](#). By contrast, experimental results [e.g., [Fujino et al., 2014](#), [Sinmyo and Hirose, 2013](#)] suggest that Fe is preferentially incorporated in bridgmanite over post-perovskite, although early experiments suggested the opposite [e.g., [Kobayashi et al., 2005](#)].

Minor constituents in the peridotite mantle (Al₂O₃, CaO and Na₂O) require respective endmembers in the dataset that represent their incorporation into and partitioning between relevant phases. When these components are important constituents of the solution phase, for instance Al₂O₃ in garnet (Figure 5.8), new phase stability fields will emerge at the expense of more simple assemblages (*cf.* Section 5.1.4). By contrast, endmembers for new components control the exact location of discontinuities, and partitioning of minor constituents is very sensitive to the correct choice of composition and properties of the endmember (sometimes fictitious).

The presence of Al₂O₃ produces minor fields of feldspar (with Na₂O and CaO in albite and anorthite, respectively, Table B.2) and (Mg,Fe)Al₃O₄ spinel, as well as an extensive field of garnet that is the dominant Al host over a wide range of *P* (Figures 5.1, 5.8 and 5.10). At low *P*, when spinel is stable, Al₂O₃ is also present in clinopyroxene (jadeite and Ca-tschermak endmembers) and orthopyroxene (Mg-tschermak) to a small extent (2 Al/100 O). When spinel transforms to garnet at 1.9 GPa, its pyrope-almandine-grossular solution accommodates a significant portion of Al₂O₃ from the pyroxenes (Figure 5.10). As the pyroxenes continuously dissolve in majoritic garnet, their Al₂O₃ content decreases rapidly. With the formation of bridgmanite at 22.6 GPa (Figure 5.1), which preferentially consumes majorite and grossular, the Al-content of garnet increases significantly, reaching values of 16 Al/100 O at 28.6 GPa, when it breaks down to the Ca-ferrite phase. This prediction is consistent with experimental data by [Ishii et al. \[2011\]](#) that show an increase from 7 to 10 Al/100 O in garnet in the pressure range between 20 and 25 GPa. In the lower mantle phase assemblage, computed with the thermodynamic database of [Stixrude and Lithgow-Bertelloni \[2011\]](#), the Ca-ferrite phase with a high content of Al in the phase (40 Al/100 O) remains a minor Al host along with modally abundant bridgmanite (3 Al/100 O), similar to experimentally determined values [e.g., [Ishii et al., 2011](#), [Nakajima et al., 2012](#)].

The CaO component is incorporated as anorthite in plagioclase at low *P*, coexisting with abundant orthopyroxene (diopside, hedenbergite and a minor Ca-tschermak component). With increasing *P*, calcium is transferred to the clinopyroxene solution (Figure 5.10). The Ca-content of the coexisting orthopyroxene (orthodiopside, Table B.2) remains low, quantitatively consistent with data by [Férot and Bolfan-Casanova \[2012\]](#). As the clinopyroxene abundance decreases in the mantle assemblage in favor of garnet, the CaO budget is progressively partitioned into the grossular component, with a maximum between 15.3 and 20.1 GPa (Figure 5.10). Garnet hosts 5 Ca/100 O, in close agreement with the maximum solubility established for a peridotite composition (6 Ca/100 O) [[Saikia et al., 2008](#)]. With the formation of Ca-perovskite above 20.1 GPa, the garnet contribution to the CaO-budget decreases at a rate consistent with experimental data [[Ishii et al., 2011](#), [Saikia et al., 2008](#)].

The budget of Na₂O in pyrolite is initially completely accommodated by feldspar,

although the albite component is low, consistent with the small ratio of $\text{Na}_2\text{O}/\text{CaO}$ in bulk pyrolite (Figure 5.10; Table 5.1). With increasing P along the 1600 K isentrope, feldspar transforms to spinel and clinopyroxene between 0 and 0.7 GPa (Figure 5.1), causing its Na_2O content to be transferred to clinopyroxene (jadeite). When garnet starts forming at 1.9 GPa with Al_2O_3 available from spinel (Figure 5.8), sodium is incorporated in garnet through its jadeite-majorite component. The Na-content of the garnet solid solution is moderated by the behavior of principal garnet endmembers: at 20.1 GPa exsolution of Ca-perovskite from garnet commences, and progressively the jadeite-majorite component is passively enriched. At 28.6 GPa, jadeite-majorite is the last garnet component to transform to a lower mantle phase, Ca-ferrite (Figures 5.1 and 5.10).

The Na_2O -bearing phases assessed here strongly depend on the database, with a very restricted set of phases in [Stixrude and Lithgow-Bertelloni \[2011\]](#) (Table B.2). By contrast, the solution models of [Holland et al. \[2013\]](#) include, in addition, a jadeite component in bridgmanite and the $\text{Na}_2\text{O}\text{-Al}_2\text{O}_3$ -rich NAL phase [e.g., [Kato et al., 2013](#)].

5.3 Petrology of Slab Lithologies

Production of basaltic oceanic crust at mid-ocean ridges (~ 7 km thick) by partial melting of primitive mantle (pyrolite) leaves behind a complementary depleted mantle (~ 35 km thick) [[Baker and Beckett, 1999](#)]. During subduction, these two lithologies play distinctive chemical, mechanical and dynamical roles [e.g., [Arredondo and Billen, 2016](#), [Emmerson and McKenzie, 2007](#), [Maierová et al., 2012](#)]. Density differences between the subducting lithosphere and the ambient mantle can lead to acceleration or stagnation of the slab [e.g., [Christensen and Hofmann, 1994](#), [Maierová et al., 2012](#)]. Similarly, an understanding of seismic velocities in the different lithologic layers can be used to trace subducting slab structure [e.g., [Bostock, 2013](#)] or be employed in forward modeling of seismic properties and wave propagation [e.g., [Ricard et al., 2005](#), [Shapiro et al., 2000](#)].

On a geologic time scale, the rehomogenization of basalt and depleted mantle by both mechanical stirring [e.g., [Kellogg and Turcotte, 1990](#), [Nakagawa et al., 2010](#), [Tirone et al., 2016](#)] and chemical diffusion [e.g., [Fei et al., 2012](#), [Holzapfel et al., 2005](#), [Shimojuku et al., 2009](#)] is a slow process, leading to the concept of a marble cake mantle [[Allègre and Turcotte, 1986](#)]. As a consequence, it has been argued that the bulk mantle may be better described by a mechanical mixture of basalt and depleted mantle originating from differentiated lithosphere rather than by a single, homogeneous pyrolite composition [e.g., [Brandenburg and van Keken, 2007](#), [Davies, 1984](#), [Nakagawa et al., 2010](#), [Xu et al., 2008](#)], a premise that we revisit in Section 6.2.2. Therefore, we explore the phase relations (Figures 5.11, 5.12 and 5.13) and various physical properties (Chapter 6) in simplified basaltic crust and depleted peridotite. We use a recently developed chemical model for bulk oceanic crust (BOC) and depleted mantle (DM) [[Chemia et al., 2015](#)] (Table 5.1), in which the BOC composition is determined by analysis of the most primitive mid-ocean ridge basalt glasses. The DM composition is estimated as the complement to BOC using a melt fraction of 0.206,

such that together they recombine to primitive mantle [McDonough and Sun, 1995].

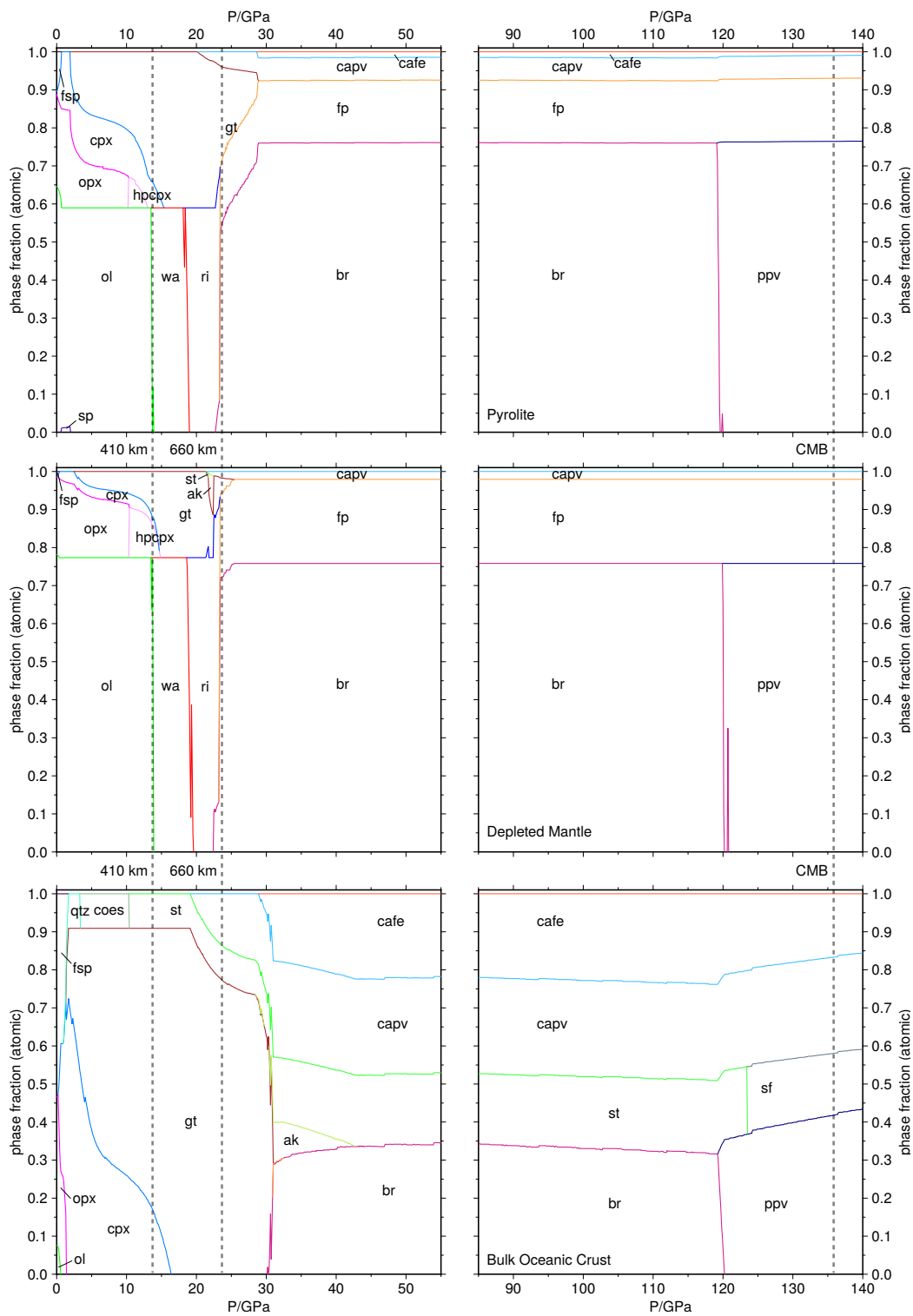


Figure 5.11: Comparison of the stable phase assemblages computed in the P -ranges 0 – 55 GPa (left column) and 85 – 140 GPa (right column) with EoS using model parameters from [Stixrude and Lithgow-Bertelloni \[2011\]](#) for different lithologies (top to bottom): Pyrolite, depleted mantle and bulk oceanic crust (Table 5.1). The graphs show the relative atomic amounts of stable phases (for abbreviations see Table B.2) for the different lithologies along the isentropes with a potential temperature of 1600 K. Pressures of the 410 km and 660 km discontinuities as well as the CMB are indicated by vertical dashed lines.

5.3.1 Phase Relations in Depleted Mantle

With an SiO_2 content slightly lower than pyrolite (Table 5.1), the depleted mantle shows phase assemblages similar to pyrolite (Figure 5.12), but with a larger proportion of Mg_2SiO_4 -based minerals (Figure 5.11). As Na_2O is perfectly incompatible in

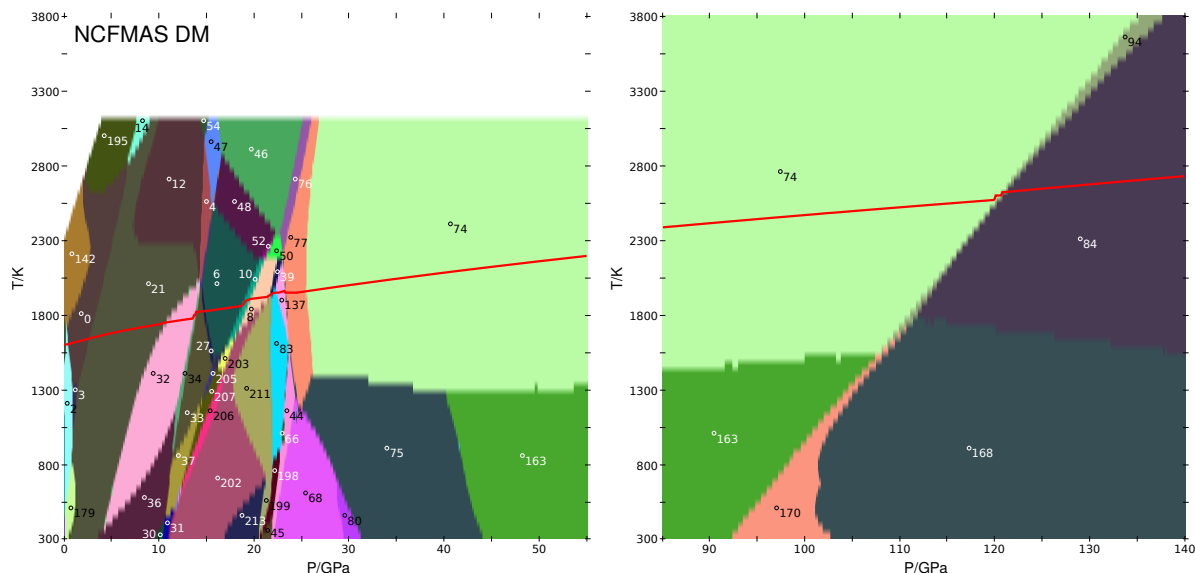


Figure 5.12: Phase diagrams computed with EoS using the model parameters from [Stixrude and Lithgow-Bertelloni \[2011\]](#) for depleted mantle (Table 5.1) as a function of P and T with 0.1 GPa and 50 K grid spacing. Panel (a) shows the P -range 0 – 55 GPa (surface to lower mantle), panel (b) shows the P -range 85 – 140 GPa (lowermost mantle). An isentrope computed with predicted material properties, starting with 1600 K at 0 GPa is shown on top of the phase diagrams as a red line. Numbered stability fields (Table B.3; for abbreviations, see Table B.2) contain the following phase assemblages for the low- P region (panel a): (0) ol+opx+cpx, (2) fsp+ol+opx+cpx, (3) sp+ol+opx+cpx, (4) ol+gt, (6) wa+gt, (8) ri+gt, (10) wa+ri+gt, (12) ol+opx+gt, (14) ol+cpx+gt, (21) ol+opx+cpx+gt, (27) wa+hpcpx+gt, (30) ol+ri+hpcpx+gt, (31) wa+ri+hpcpx+gt, (32) ol+cpx+hpcpx+gt, (33) wa+cpx+hpcpx+gt, (34) ol+wa+cpx+hpcpx+gt, (36) ol+ri+cpx+hpcpx+gt, (37) wa+ri+cpx+hpcpx+gt, (39) ri+capv+gt, (44) capv+ak+fp, (45) ri+capv+ak+fp, (46) gt+fp, (47) ol+gt+fp, (48) wa+gt+fp, (50) ri+gt+fp, (52) wa+ri+gt+fp, (54) ol+opx+gt+fp, (68) capv+ak+st+fp, (74) capv+br+fp, (75) capv+ak+br+fp, (76) gt+br+fp, (77) capv+gt+br+fp, (80) capv+ak+st+br+fp, (83) ri+capv+ak+gt, (137) ri+capv+gt+br, (142) ol+opx, (179) ol+opx+cpx+ky, (195) ol+cpx, (198) ri+capv+ak, (199) ri+capv+ak+st, (202) ri+gt+st, (203) wa+ri+gt+st, (205) wa+cpx+gt+st, (206) ri+cpx+gt+st, (207) wa+ri+cpx+gt+st, (211) ri+capv+gt+st, (213) ri+ak+gt+st. Along the isentrope the following transitions occur in the Mg_2SiO_4 -based system: ol \rightarrow wa (32 \rightarrow 34) \rightarrow 33 at 13.7 GPa and 1800 K), wa \rightarrow ri (6 \rightarrow 10) \rightarrow 8 at 18.8 GPa and 1870 K), ri \rightarrow br+fp (137 \rightarrow 77 at 23.3 GPa and 1950 K). In the MgSiO_3 -based system the following transitions occur: fsp \rightarrow opx+cpx (2 \rightarrow 0 at 0.6 GPa and 1590 K), opx+cpx \rightarrow cpx+hpcpx+gt (0 \rightarrow 21) \rightarrow 32 between 2.7 GPa and 10.7 GPa, 1630 K and 1740 K), cpx \rightarrow hpcpx (33 \rightarrow 27 at 14.6 GPa and 1820 K), hpcpx \rightarrow gt (27 \rightarrow 6 at 15.0 GPa and 1830 K), gt \rightarrow capv+br+fp (8 \rightarrow (39, 83, 137, 77) \rightarrow 74 between 21.7 GPa and 25.4 GPa, 1930 K and 1960 K) via capv in (8 \rightarrow 39 at 21.7 GPa and 1940 K), ak in (39 \rightarrow 83 at 22.0 GPa and 1950 K), ak \rightarrow br (83 \rightarrow 137 at 22.5 GPa and 1950 K) and gt out (77 \rightarrow 74 at 25.4 GPa and 1960 K). In the high- P region (panel b) the following phase assemblages occur: (74) capv+br+fp, (84) capv+ppv+fp, (94) capv+br+ppv+fp, (163) capv+br+fp+cf, (168) capv+ppv+fp+cf, (170) capv+br+ppv+fp+cf. The isentrope intersects the br \rightarrow ppv phase boundary (74 \rightarrow 84) at 120.8 GPa and 2600 K. Phase fields given in parentheses indicate coexistence regions; in those cases, P and T refer to conditions at the boundaries or the center of the intersection between isentrope and coexistence region.

olivine and orthopyroxene, the depleted mantle does not retain any Na_2O and hence phases containing sodium are absent in the DM phase assemblages. In particular, this leads to the absence of the Ca-ferrite phase in the lower mantle and a reduction in clinopyroxene stability at upper mantle pressures, similar to the phase relations in the reduced CFMAS pyrolite composition (Figures 5.1 and 5.6). At pressures below 1 GPa, CaO and Al_2O_3 are incorporated in clinopyroxene and anorthite (Figures 5.11 and 5.12), but the transition to spinel that is typical for pyrolite (Figures 5.7 and 5.1) is absent due to the low abundance of Al_2O_3 , entirely accommodated by the pyroxene solid solutions. This is qualitatively consistent with calculations using the database of Holland and Powell [1998] on the same composition [Chemia et al., 2015], where spinel stability is restricted to $T < 1050$ K.

While phase transitions of the Mg_2SiO_4 -based minerals in the depleted mantle occur at the same pressure and with the same Clapeyron slopes as in pyrolite, the phase relations in the MgSiO_3 -based minerals differ significantly. This is due to the strong depletion of both Al_2O_3 and CaO in the DM composition (Table 5.1). Most importantly, the garnet stability range is reduced when compared to pyrolite (Figure 5.8). The transformation of garnet to bridgmanite occurs at significantly lower pressure than predicted for pyrolite, but in good agreement with the experiments by Ishii et al. [2011]. Along the 1600 K adiabat, with increasing P garnet partially decomposes to ringwoodite and stishovite, and then forms akimotoite, with a very narrow stability range (Figure 5.8). This resembles the phase relations in the pyrolite FMAS system (Figures 5.1 and 5.5), as the CaO-component in DM exsolves Ca-perovskite from garnet at the same P , creating essentially a Ca-free garnet composition. The occurrence of coexisting garnet, stishovite and ringwoodite or garnet and akimotoite at ~ 20 GPa is consistent with experiments by Irifune and Ringwood [1987] that have been performed at lower T , and the bridgmanite and ringwoodite coexistence between ~ 22.5 GPa and ~ 23.5 GPa agrees with experiments by Kato et al. [2014].

Post-perovskite formation occurs at slightly higher pressure than for pyrolite (Figures 5.11, 5.7 and 5.12).

5.3.2 Phase Relations in Bulk Oceanic Crust

With a mole fraction of silica, $x(\text{SiO}_2) > 0.5$ (Table 5.1), the phase assemblages in the bulk oceanic crust consist – for the largest part – of coexisting MgSiO_3 -based minerals and a free SiO_2 phase (Figures 5.11 and 5.13). With BOC strongly enriched in CaO, Al_2O_3 and Na_2O relative to pyrolite (Table 5.1), phase relations between pyroxenes, garnet, akimotoite (Figure 5.8) and other lower mantle phases show significant differences to pyrolite.

At 1600 K and ambient pressure, the phase assemblage predicted is olivine, orthopyroxene and plagioclase (Figures 5.11 and 5.13). With increasing pressure along the 1600 K isentrope, olivine and plagioclase are replaced by clinopyroxene and garnet, with minor quantities of β -quartz (Figures 5.11 and 5.13), a typical phase assemblage for basalt at upper mantle conditions [e.g., Irifune and Ringwood, 1993, Ricolleau et al., 2010]. At high P , the occurrence of pyroxene-based phases along the 1600 K isentrope is similar to pyrolite, with the exception that high-pressure clinopyroxenes – with only MgSiO_3 and FeSiO_3 in the solid solution (Table B.2) – are not

predicted stable (Figures 5.11 and 5.13). Similarly, the stability range of orthopyroxene is limited to the same pressure as plagioclase. Garnet and clinopyroxene with their wide range of solid solutions (Table B.2) dominate the phase assemblage, with clinopyroxene dissolving into garnet, as already described for the pyrolite lithologies

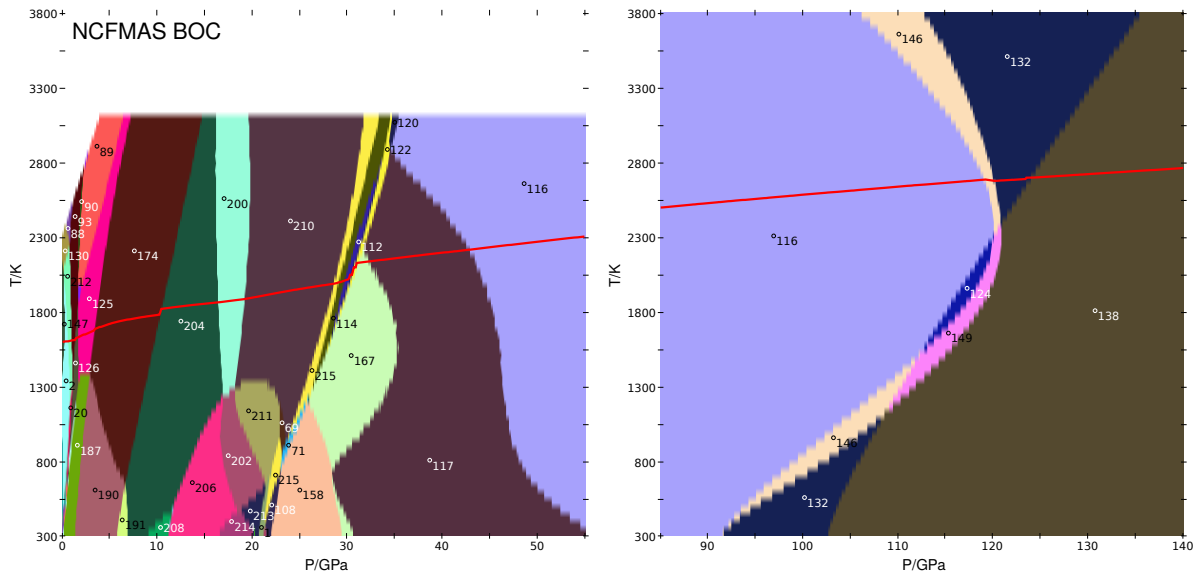


Figure 5.13: Phase diagrams computed with EoS using the model parameters from [Stixrude and Lithgow-Bertelloni \[2011\]](#) for bulk oceanic crust (Table 5.1) as a function of P and T with 0.1 GPa and 50 K grid spacing. Panel (a) shows the P -range 0 – 55 GPa (surface to lower mantle), panel (b) shows the P -range 85 – 140 GPa (lowermost mantle). An isentrope computed with predicted material properties, starting with 1600 K at 0 GPa is shown on top of the phase diagrams as a red line. Numbered stability fields (Table B.3; for abbreviations, see Table B.2) contain the following phase assemblages for the low- P region (panel a): (1) ol+opx+cpx, (2) fsp+ol+opx+cpx, (20) fsp+opx+cpx+gt, (69) capv+gt+st+fp, (71) capv+ak+gt+st+fp, (88) fsp+opx+qz, (89) cpx+qz, (90) fsp+cpx+qz, (93) fsp+opx+cpx+qz, (108) capv+ak+st+cf, (112) capv+gt+st+cf, (114) capv+ak+gt+st+cf, (116) capv+st+br+cf, (117) capv+ak+st+br+cf, (120) capv+gt+st+br+cf, (122) capv+ak+gt+st+br+cf, (125) cpx+gt+qz, (126) fsp+cpx+gt+qz, (130) fsp+opx, (147) fsp+ol+opx, (158) capv+ak+st+fp+cf, (167) capv+ak+st+br+fp+cf, (174) cpx+gt+coes, (187) cpx+gt+qz+ky, (190) cpx+gt+coes+ky, (191) cpx+gt+st+ky, (200) gt+st, (202) ri+gt+st, (204) cpx+gt+st, (206) ri+cpx+gt+st, (208) cpx+hpcpx+gt+st, (210) capv+gt+st, (211) ri+capv+gt+st, (212) fsp+opx+cpx, (213) ri+ak+gt+st, (214) ri+cpx+ak+gt+st, (215) capv+ak+gt+st. Along the isentrope the following transitions occur in the MgSiO_3 -based system: opx \rightarrow cpx (93 \rightarrow 126 at 1.2 GPa and 1610 K), fsp \rightarrow cpx+gt (126 \rightarrow 125 at 1.7 GPa and 1630 K), cpx \rightarrow gt (204 \rightarrow 200 at 16.4 GPa and 1860 K), gt \rightarrow ak+capv+br+fp+cf (200 \rightarrow (210, 215, 114, 112, 122) \rightarrow 167 between 19.1 GPa and 31.2 GPa, 1880 K and 2120 K) via capv in (200 \rightarrow 210 at 19.3 GPa and 1890 K), ak in (210 \rightarrow 215 at 28.5 GPa and 1990 K), cafe in (215 \rightarrow 114 at 29.1 GPa and 2000 K), ak out (114 \rightarrow 112 at 29.8 GPa and 2010 K), br in (112 \rightarrow 122 at 30.6 GPa and 2080 K) and gt out (122 \rightarrow 167 at 31.1 GPa and 2130 K), ak+fp \rightarrow br+cf (167 \rightarrow (117) \rightarrow 116 between 32.2 GPa and 42.7 GPa, 2130 K and 2210 K) via fp out (167 \rightarrow 117 at 32.2 GPa and 2130 K) and ak out (117 \rightarrow 116 at 42.7 GPa and 2210 K). The following SiO_2 phase transitions occur: qz \rightarrow coes (125 \rightarrow 174 at 3.3 GPa and 1680 K), coes \rightarrow st (174 \rightarrow 204 at 10.4 GPa and 1800 K). In the high- P region (panel b) the following phase assemblages occur: (116) capv+st+br+cf, (124) capv+sf+br+cf, (132) capv+st+ppv+cf, (138) capv+sf+ppv+cf, (146) capv+st+br+ppv+cf, (149) capv+sf+br+ppv+cf. The isentrope intersects the br \rightarrow ppv phase boundary (116 \rightarrow (146) \rightarrow 132 between 119.0 GPa and 120.1 GPa, 2680 K and 2670 K) and the st \rightarrow sf phase boundary (132 \rightarrow 138 at 124.3 GPa and 2700 K). Phase fields given in parentheses indicate coexistence regions; in those cases P and T refer to conditions at the boundaries or the center of the intersection between isentrope and coexistence region.

(Section 5.1). The Ca-perovskite forming reaction from garnet is predicted at significantly lower P than experimentally determined [Irifune and Ringwood, 1993, Litasov and Ohtani, 2005]. At $P > 20$ GPa, the phase relations computed here (Figures 5.11 and 5.13) and determined in experiments [Hirose et al., 1999, Irifune and Ringwood, 1993, Litasov and Ohtani, 2005, Ricolleau et al., 2010] differ significantly. In the experiments, a Na₂O-Al₂O₃-rich (NAL) phase [Imada et al., 2012, Kato et al., 2013] is observed that coexists with Ca-ferrite to $P > 40$ GPa. The NAL phase is not included in the assessment of Stixrude and Lithgow-Bertelloni [2011], which can – in part – account for the following two observations (Figures 5.8, 5.13 and 5.11): (i) garnet – with its endmembers jadeite-majorite and pyrope – stays stable over a wide P -range, before Al₂O₃-rich compositions of akimotoite and bridgmanite as well as Na₂O-bearing Ca-ferrite are formed near 30 GPa, consistent with computations by Xu et al. [2008]; (ii) akimotoite is predicted to remain stable in BOC to more than 40 GPa (Figure 5.8). This is a significantly larger pressure than that determined in Xu et al. [2008].

The discrepancy in phase assemblage predictions presented here and the closely related results by Xu et al. [2008] is caused by two factors: (i) differences in the basalt composition used in Xu et al. [2008] [Presnall and Hoover, 1987] and here [Chemia et al., 2015]; (ii) differences in the datasets by Xu et al. [2008] and Stixrude and Lithgow-Bertelloni [2011], in particular those stabilizing bridgmanite (Fe-component) and jadeite-majorite (Table B.2). A more detailed comparison between the two datasets and the two compositions is provided in Appendix A.

At lowermost mantle pressures, post-perovskite in bulk oceanic crust is formed over a narrow coexistence region at conditions very similar to those for pyrolite and depleted mantle (Figures 5.11 and 5.13), although experiments [Grocholski et al., 2012, Ohta et al., 2008] suggest a somewhat lower transition pressure for basaltic compositions.

Along the 1600 K isentrope for bulk oceanic crust, β -quartz transforms to coesite and then to stishovite (Figures 5.11 and 5.13), in good agreement with experiments [e.g., Zhang et al., 1993] and prior thermodynamic assessments [e.g., Swamy et al., 1994]. At pressures of the lower mantle, stishovite undergoes a displacive phase transition from the rutile to the CaCl₂ structure that is accounted for by a Landau model (Section 2.5), with a transition P again in good agreement with experiments [Ono et al., 2002]. The transformation to PbO₂-structured SiO₂ (seifertite) is predicted in the model by Stixrude and Lithgow-Bertelloni [2011] at 125 GPa, i.e., at higher pressure than the post-perovskite transition (Figures 5.11 and 5.13), in agreement with experiments by Grocholski et al. [2013].

Chapter 6

Thermochemical Properties of the Mantle

6.1 Adiabatic Temperatures

We use the stable phase assemblages and their thermodynamic properties to determine isentropic T -profiles as a function of pressure to define mantle adiabats and as approximations to geotherms [Ganguly et al., 2009, Turcotte and Schubert, 2002]. In our approach, we calculate the entropy content of a lithology at the potential temperature and 0 GPa and trace this entropy value as a function of P . This provides an exact solution as an alternative to the parameterized formulation of the adiabat

$$\left(\frac{\partial T}{\partial P}\right)_S = \frac{\alpha}{\rho C_P} \cdot T, \quad (6.1)$$

often used in geophysics, where values for density and thermal expansivity are usually based on P - V - T experimental data [e.g., Brown and Shankland, 1981, Katsura et al., 2010, Stacey and Davis, 2008].

Within a specific phase stability field, temperature along an isentrope increases smoothly due to self-compression, whereas at phase transitions, temperature can change discontinuously through volume collapse and latent heat release or consumption due to a positive or negative Clausius-Clapeyron slope, respectively [e.g., Verhoogen, 1965] (Figure 6.1). Examples for latent heat release are the transformations of olivine to wadsleyite and wadsleyite to ringwoodite, for latent heat consumption the ringwoodite breakdown (Section 5.1). Here we follow isentropes for pyrolite, depleted mantle and bulk oceanic crust with a potential temperature of 1600 K, assumed to be typical for the mantle [e.g., Herzberg et al., 2007], as well as those with potential temperatures of 1400 K and 1800 K. The reference potential temperature chosen here (1600 K) is at the lower end of recent estimates for mid-ocean ridge basalt extraction [Dalton et al., 2014, Sarafian et al., 2017].

6.1.1 Isentrope in Pyrolite Mantle

The 1600 K isentrope for pyrolite is characterized by three discontinuities, representing the olivine to wadsleyite, wadsleyite to ringwoodite transitions and the ringwood-

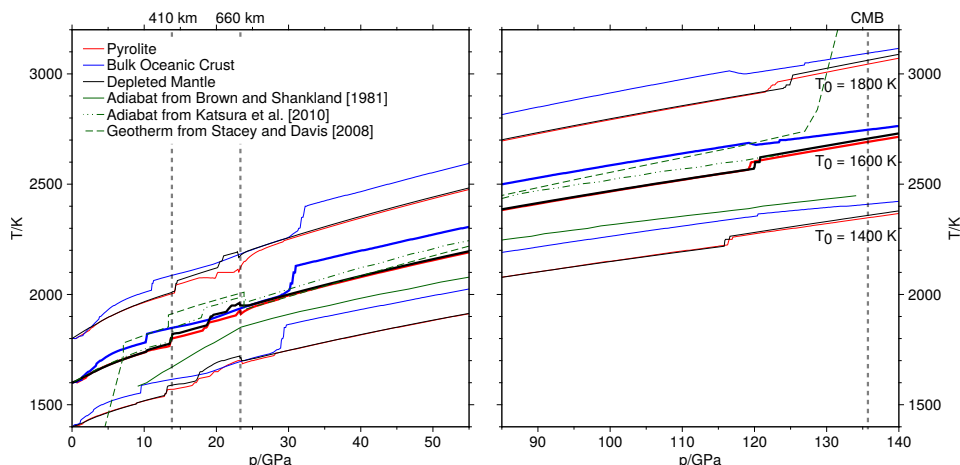


Figure 6.1: Self-consistently computed isentropes using the model parameters from [Stixrude and Lithgow-Bertelloni \[2011\]](#) for three different lithologies, representing the average mantle (pyrolite, red lines) and both the basaltic (bulk oceanic crust, blue lines) and the depleted part (depleted mantle, black lines) of oceanic lithosphere. Adiabats with potential temperatures of 1400 K, 1600 K and 1800 K are shown for a pressure range of 0 – 55 GPa and of 85 – 140 GPa in the left and right panels, respectively. For comparison, the adiabats by [Brown and Shankland \[1981\]](#) (green solid line) and [Katsura et al. \[2010\]](#) (green dash-dotted line), as well as the geotherm by [Stacey and Davis \[2008\]](#) (green dashed line), are included. Vertical dashed lines indicate the pressure of the 410 km and 660 km discontinuities (left panel) and the core-mantle boundary (right panel).

ite breakdown, respectively (Figure 6.1). Of those, wadsleyite transforms to ringwoodite through a significant coexistence region (Section 5.1) and the associated temperature increase is distributed between the ringwoodite-in and wadsleyite-out reactions (Figures 5.1 and 5.7). By contrast, in the MgSiO_3 -based system the phase transitions occur through wide coexistence regions, and only the orthopyroxene-out (10.3 GPa), bridgmanite-in (22.5 GPa) and garnet-out (28.6 GPa) reactions are associated with a small T -increase along the 1600 K isentrope (Figures 5.7 and 6.1), similar to the predictions by [Stixrude and Lithgow-Bertelloni \[2011\]](#). At the base of the mantle, the post-perovskite transition leads to a significant T -increase, consistent with the large positive Clapeyron slope of the transition (Section 5.1).

The model results using the database of [Stixrude and Lithgow-Bertelloni \[2011\]](#) show that the T -increase along an isentrope with pressure varies significantly for different potential temperatures. Hotter isentropes reach a larger temperature difference than colder ones across the mantle. For instance, along the 1600 K isentrope the temperature increases by ~ 1100 K, while for isentropes with a potential temperature of 200 K lower and higher, the differences reach ~ 950 K and ~ 1250 K, respectively. If hotspot volcanism with an excess T of ~ 200 K at extraction [[Herzberg et al., 2007](#)] is indeed caused by thermal plumes that rise adiabatically from the core-mantle boundary, their excess temperature in the lower mantle is predicted to be ~ 350 K, consistent with previous estimates [[Kennett and Bunge, 2008](#), [Piazzoni et al., 2007](#)]. Combined with the consideration that plumes rise quasi-adiabatically, while the surrounding mantle is sub-adiabatic due to slow overturn [[Bunge, 2005](#), [Jeanloz and Morris, 1987](#)], this supports the notion of a stronger contribution of plumes to the global heat budget than often thought [e.g., [Davies, 1993](#)].

A comparison between the 1600 K adiabat and adiabatic gradients computed here

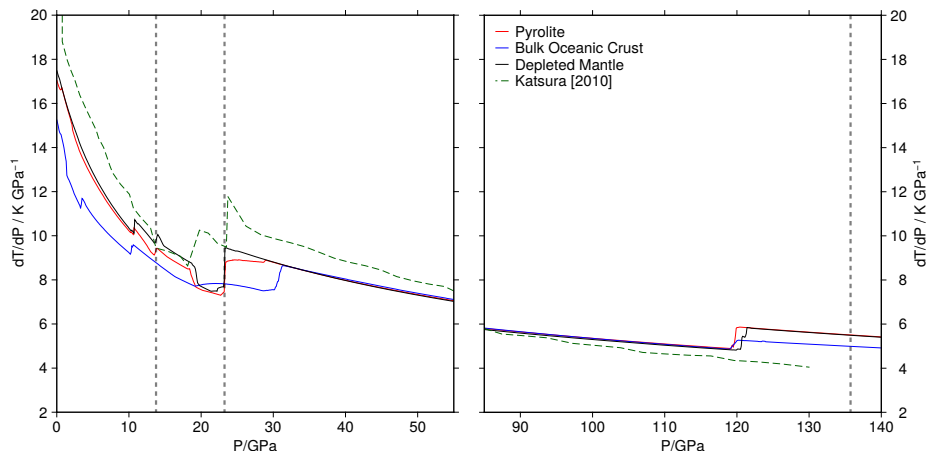


Figure 6.2: Pressure derivative of isentropes computed self-consistently using the model parameters from [Stixrude and Lithgow-Bertelloni \[2011\]](#) (solid red, blue and black lines). The adiabatic gradient from [Katsura et al. \[2010\]](#) is shown for comparison (dashed green line). See Figure 6.1 for the corresponding isentropes.

and that by [Katsura et al. \[2010\]](#) illustrates the importance of considering the full phase assemblage, which takes varying partitioning of chemical components between phases into account (*cf.* Section 5.2), rather than individual phases, as used by [Katsura et al. \[2010\]](#) (Figures 6.1 and 6.2). Temperature discontinuities produced at major phase transitions are less pronounced in a multiphase assemblage, and phase changes in the MgSiO_3 -based systems as well as redistribution of elements between different phases are significant temperature buffers.

6.1.2 Isentropes in Slab Lithologies

Isentropes for a depleted mantle composition show stronger T -discontinuities (Figure 6.1) at the phase transitions of the Mg_2SiO_4 minerals than in pyrolite, as a higher MgO budget results in larger proportions of olivine, wadsleyite and ringwoodite in the assemblage (Figure 5.11). This effect propagates to higher temperatures in the transition zone, and an additional slight increase relative to pyrolite stems from the occurrence of akimotoite and its transformation to bridgmanite at 22.5 GPa (Figures 5.11 and 6.1). In the lower mantle, adiabatic gradients for harzburgite are shallower (Figure 6.2) and the isentropes become similar to those of pyrolite near 30 GPa.

For the oceanic crust, isentropes differ significantly from the peridotite assemblages both in terms of discontinuities and slopes (Figures 6.1 and 6.2). Phase transitions for SiO_2 minerals dominate T -discontinuities at upper mantle pressures (Figures 5.11 and 5.13). Therefore, and despite an overall lower gradient, the bulk oceanic crust heats significantly more rapidly from adiabatic compression than the peridotitic mantle. Near 12 GPa, i.e., above the coesite-stishovite transition in the bulk oceanic crust and below the olivine-wadsleyite transition in DM, temperature differences reach 80 K. With the latent heat release at the Mg_2SiO_4 phase transformations, the isentropes for peridotitic mantle and bulk oceanic crust become comparable. Above 30 GPa, significant heat is added to the basalt assemblage by the garnet-out reaction (Figures 5.11 and 6.1), and throughout the lower mantle, the 1600 K isen-

trope for bulk oceanic crust stays hotter than those for the depleted mantle and pyrolite.

The post-perovskite transition is reached with a negative Clapeyron slope for bulk oceanic crust (Figure 5.13), resulting in a temperature decrease. However, the Clapeyron slope of this phase transition is strongly T -dependent, with a reversal at 2260 K and 121 GPa; in contrast to the 1600 K isentrope, the 1400 K adiabat experiences a slight T -increase at the post-perovskite transition.

The significantly steeper temperature increase for isentropes in the oceanic crust than for those in the surrounding pyrolytic or harzburgitic mantle implies that the crustal section of a subducting slab is heated at a faster rate than the underlying depleted mantle, to a degree that should influence thermal equilibration of the subducting slab. However, the latent heat contribution of the quartz-coesite transformation coincides with other – more significant – heat transport processes, such as the onset of full coupling between the slab and the mantle wedge [e.g., Peacock et al., 2005, Syracuse et al., 2010] or latent heat released due to devolatilization reactions [e.g., Chemia et al., 2015]. With a significantly reduced volatile budget in the bulk oceanic crust at pressures above 5 GPa [e.g., Chemia et al., 2015, van Keken et al., 2011], the coesite-stishovite transformation should exert an effect on the thermal evolution of the slab worth exploring in subduction zone modeling.

6.2 Seismic Properties

6.2.1 Density and Elasticity Profiles of Individual Lithologies

Density and seismic profiles computed along the 1600 K isentrope for pyrolite (Figure 6.3) are similar to previous estimates [e.g., Piazzoni et al., 2007, Vacher et al., 1998, Xu et al., 2008]. Density, compressional and shear wave velocity increase with pressure, and discontinuous changes are associated with phase transitions. The phase transformations in the Mg_2SiO_4 -based systems have the largest effect and lead to discontinuities in density, for example, by 0.08, 0.06 and 0.10 g/cm^{-3} at the olivine-wadsleyite, wadsleyite-ringwoodite transitions and the ringwoodite breakdown, respectively. The relative magnitude of changes in v_P and v_S across these transitions is similar.

Transition pressures are in good agreement with the two major discontinuities in the seismic reference model AK135-f [Kennett et al., 1995, Montagner and Kennett, 1996] at depths of 410 and 660 km. The changes in density and seismic wave velocities at the 410 km discontinuity (13.2 – 13.8 GPa) are comparable to values of AK135-f, and so are the differences for the divariant wadsleyite-ringwoodite transition at 520 km (18.1 – 19.0 GPa) (Figure 5.1). This is in contrast to values from experiments for pure olivine that yield significantly higher jumps [e.g., Mao et al., 2015, Sinogeikin et al., 1998], even if one accounts for the relevant phase proportions (Figure 5.1). At the 660 km discontinuity, the steps in density and seismic wave velocities are not captured quantitatively by the pyrolite system using the database of Stixrude and Lithgow-Bertelloni [2011] (Figure 6.3). Progressive disappearance of garnet at depths larger than 660 km is reflected to some extent in AK135-f (with a separate parametrization

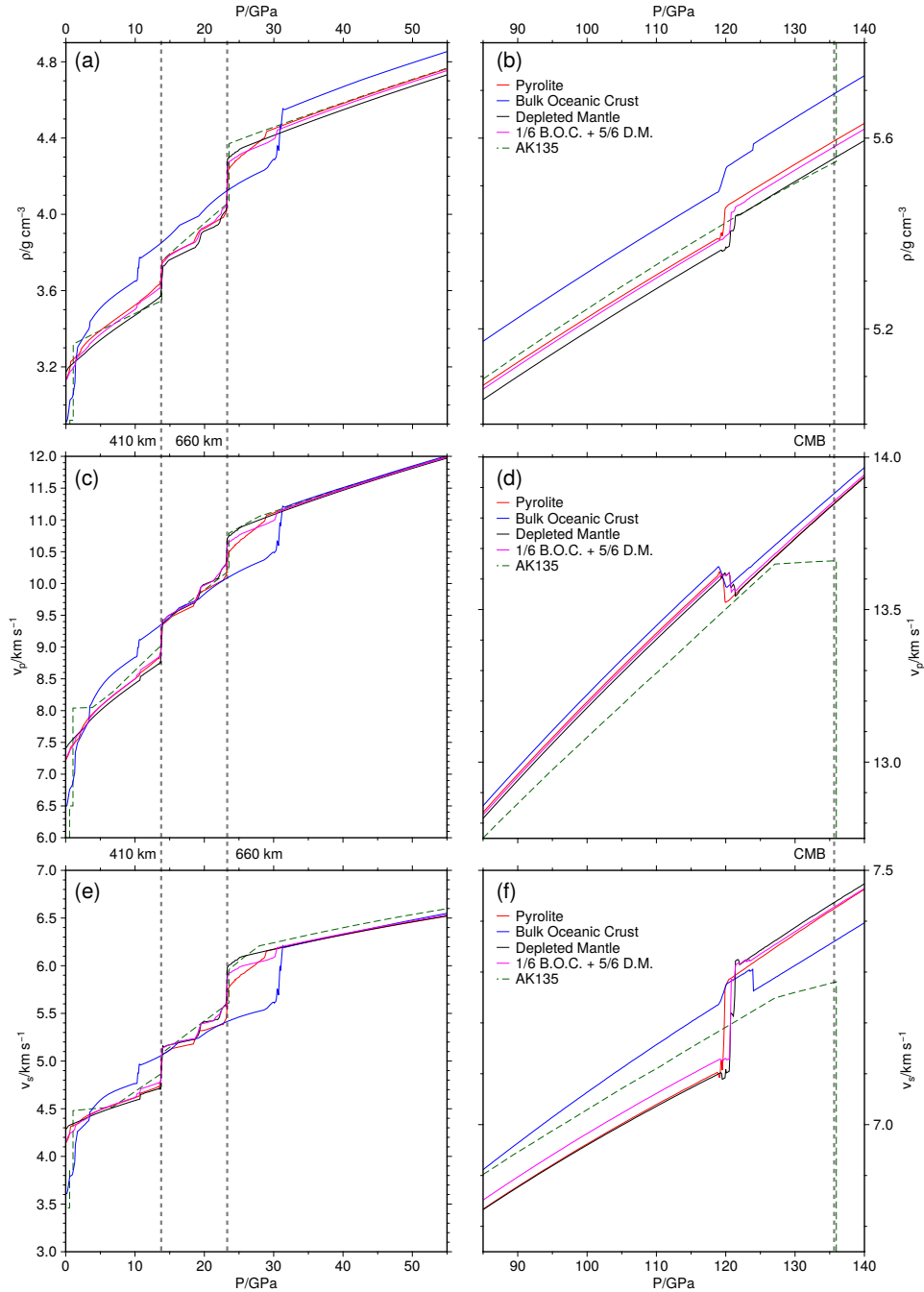


Figure 6.3: Density (panels a and b), P-wave (panels c and d) and S-wave velocities (panels e and f) for the three model lithologies pyrolite (red), bulk oceanic crust (blue) and depleted mantle (black) along their respective 1600 K adiabats (Figure 6.1). Properties of the mechanical mixture of 1/6 bulk oceanic crust with 5/6 depleted mantle (magenta) are shown along the adiabat for pyrolite. Physical parameters are computed with EoS using the model parameters from [Stixrude and Lithgow-Bertelloni \[2011\]](#). For comparison, profiles from AK135-f [[Kennett et al., 1995](#), [Montagner and Kennett, 1996](#)] are included as dashed lines (green). Pressures for the 410 km and 660 km discontinuities and the core-mantle boundary are indicated by vertical dashed lines.

of the model between 660 and 1000 km depth). At higher P , in the absence of garnet, density and v_p agree well with the values of AK135-f, but v_s remains somewhat lower.

The increase of all three properties with pressure in the lower mantle is greater

in seismic models than in predictions using the thermodynamic database of [Stixrude and Lithgow-Bertelloni \[2011\]](#) (Figure 6.3) and these differences increase until the D'' layer is reached. At the post-perovskite transition (120 GPa), density and shear wave velocity increase, while the compressional wave velocity decreases. For other phase transitions in the MgSiO₃-based system – with the exception of the formation of Ca-perovskite – notable discontinuities in at least the shear wave velocity are predicted, but values and impedances are too low to be detected seismically.

In the depleted mantle, the major discontinuities arising from the Mg₂SiO₄-based minerals are more pronounced than in pyrolite (Figure 6.3) due to its higher Mg₂SiO₄ content (Figure 5.11). The simultaneous transformation of both pyroxenes into garnet for DM leads to a more pronounced discontinuity at 14.8 GPa in seismic wave velocities than for pyrolite. Similarly, the complex phase relations at pressures of the lower transition zone in DM result in more substantial changes for all parameters before the ringwoodite breakdown is reached. As the garnet disappearance occurs within 2 GPa of the ringwoodite breakdown, this transition is not individually resolvable in the profiles (Figure 6.3).

For bulk oceanic crust, density and seismic wave velocities at ambient pressure are significantly lower than for the other lithologies (Figure 6.3), but with eclogitization near 2 GPa (Figure 5.11) they become comparable. At higher pressure, the properties of the bulk oceanic crust are dominated by phase transitions of the SiO₂ polymorphs; with the quartz-coesite transition (3.3 GPa), density and seismic velocities become significantly larger than for the other lithologies at upper mantle conditions and these differences are further enhanced at the coesite-stishovite transformation (10.3 GPa). For transition zone pressures, BOC stays denser than pyrolite or depleted mantle due to the presence of stishovite and garnet, but seismic velocities become comparable between the different lithologies due to the presence of the high-pressure Mg₂SiO₄ phases in the two ultramafic lithologies. At uppermost lower mantle pressures, both density and seismic velocities are lower for BOC, as bridgmanite is formed only at 30 GPa (Figure 5.11). Density trends of the primitive and depleted mantle and the oceanic crust presented here are qualitatively consistent with experiments [e.g., [Irifune and Ringwood, 1993](#), [Sinogeikin et al., 1998](#)], but quantitatively the differences in density between these lithologies described by the model of [Stixrude and Lithgow-Bertelloni \[2011\]](#) are smaller.

The results of the thermodynamic model are not applicable to the seismic structure of subduction zones directly, as temperatures are much lower than the adiabats presented here. A comparison between predicted data and seismic observations is further complicated as elastic parameters are affected by the presence of volatiles and crack microstructure [e.g., [Adam and Otheim, 2013](#)]. Nevertheless, the crustal section of the subducting lithosphere can be traced by low v_S , in some instances to depths corresponding to the transformation to an eclogite assemblage. At pressures larger than 2 GPa, seismic velocities become comparable for the different lithologies, and subducted crust cannot be imaged further in most cases [e.g., [Bostock, 2013](#)]. However, a detailed seismic survey of the Cocos slab subducting below central Mexico [[Kim et al., 2012](#)] reveals a transition from a negative to a positive perturbation of v_S in the crustal section of the slab. This conversion coincides with the disappearance of the velocity contrast between the oceanic crust and depleted mantle sections of

the slab, and can be interpreted as elastic velocities in the different lithologies approaching similar values (Figure 6.3).

The significant increase in seismic velocities of eclogitized BOC across the quartz-coesite transition, however, has not yet been mapped in a subducting slab.

6.2.2 Homogeneous vs. Mechanically Mixed Mantle

Differences in the 1D profiles for seismic properties exist between a homogeneous pyrolitic mantle and a mechanical mixture of DM and BOC (5:1 by mass) in terms of the location and magnitude of discontinuities (Figure 6.3). These differences are caused by the larger number of phase transitions in the mechanical mixture that come from both its harzburgite and basalt components (Figure 5.11). However, compared to differences between the seismic observations and thermodynamic predictions, they are minor, and no significant advantage of using a mechanical mixture over a chemically homogeneous pyrolite is apparent.

This inference is best illustrated for the transition zone (Figure 6.3). On the one hand, velocity and density discontinuities occurring across all three major phase transitions are slightly larger for pyrolite than for the mechanical mixture, and therefore in closer agreement with the seismic estimates, as are their gradients across the transition zone – measured as the absolute difference between values at 13.8 and 23.3 GPa. On the other hand, the absolute values for v_P and v_S in the transition zone are larger for the mechanical mixture, and therefore in closer agreement with AK135-f. Gradients of seismic velocities for pyrolite and the mechanical mixture are virtually indistinguishable in both the upper and lower mantle.

Further considerations support the notion that current observations cannot differentiate properties computed for a mechanical mixture and a pyrolite aggregate. We want to illustrate this with three examples:

- (i). Chemical heterogeneity has been invoked to account for large values of the shear to compressional wave velocity ratio ($R_{S/P} = d \ln v_S / d \ln v_P$) in the Earth's lowermost mantle [e.g., Mora et al., 2011, Trampert et al., 2004]. These large differences favor a mechanically mixed mantle, as the heterogeneity is often assumed to be accumulated basaltic oceanic crust [e.g., Brandenburg and van Keken, 2007, Nakagawa et al., 2009, Tackley, 2011]. However, the basaltic fractions involved would often have to be unrealistically high [e.g., Cammarano et al., 2009, Nakagawa et al., 2009, Tackley, 2011], and accumulation of oceanic crust in the lowermost mantle appears dynamically challenging [Li and McNamara, 2013]. Furthermore, Tesoniero et al. [2016] have recently found that $R_{S/P}$ values predicted for pyrolite and a mechanically mixed mantle do not differ in a significant way.
- (ii). Ritsema et al. [2009a,b] have modeled arrival time differences for seismic phases sensitive to the 410 km and 660 km discontinuities (i.e., SS-precursors and receiver functions) using synthetic transition zone structure with both a homogeneous pyrolite and a mechanical mixture model. While they find the variation in transition zone thickness to be similar for both pyrolite and mechanical mixture, the temperature models based on travel time differences point to isentropes

with potential temperature of 1700 – 1750 K for pyrolite and 1600 – 1650 K for the mechanical mixture, respectively. Originally, this inference has been used to support the notion of a mechanically mixed mantle, but with the recent upward revision of the potential temperature for the mantle adiabat [Dalton et al., 2014, Sarafian et al., 2017], this notion no longer holds.

- (iii). Using the same v_P , v_S and ρ models as Ritsema et al. [2009a,b], Cammarano et al. [2011] have shown that a global dataset of free oscillations and body-wave travel times can, in case of mechanical mixture, only be matched with temperatures in the upper 800 km of the mantle that fall below the 1600 K isentrope, i.e., significantly smaller than temperatures of Ritsema et al. [2009a,b].

We want to end this section by emphasizing that a comparison of seismic reference profiles with computed 1D profiles for ρ , v_P and v_S based on a thermodynamic-elastic model such as that of Stixrude and Lithgow-Bertelloni [2011] has inherent limitations for several reasons:

- (i). Attenuation plays a significant role in the Earth's mantle for seismic frequencies [e.g., Goes et al., 2004, Karato, 1993, Stixrude and Lithgow-Bertelloni, 2005b], while computed elastic properties are tabulated for experimental frequencies in the laboratory. In principle, an anelastic correction can be incorporated in a thermodynamic model as a post-processing step, but large uncertainties exist with respect to the parameters entering the correction [Matas and Bukowinski, 2007].
- (ii). Temperature in the Earth's mantle deviates from an adiabatic profile owing to radiogenic heat production and a heat exchange due to slow overturn [e.g., Bunge, 2005, Cobden et al., 2008, Matas et al., 2007]. Slightly lower temperatures in the transition zone would, for example, lead to the stability of akimotoite in pyrolite (Figures 5.7 and 5.8), with additional consequences for elastic properties.
- (iii). The lateral average of a dependent property is not necessarily the same as the single value predicted along the T -profile averaged *a-priori*. For seismic properties, these two approaches yield close results in the lower mantle, but deviate substantially in the vicinity of phase transitions [e.g., Styles et al., 2011, Tesoniero et al., 2016]. Therefore such a comparison is of limited use in inferring the thermal structure or composition of Earth's mantle, although this approach has been pursued for decades [e.g., Cobden et al., 2009, Ita and Stixrude, 1992, Vacher et al., 1998]. We will discuss alternative approaches to infer mantle structure based on thermodynamic models in Section 7.2.

Chapter 7

Current Limitations and Future Developments

7.1 Coverage, Consistency and Accuracy of Thermodynamic Models

The practical significance of thermodynamic models and datasets is related to – and limited by – a number of criteria ranging from the completeness of the database (for a given problem) to the requirement that it should be formulated in a thermodynamically self-consistent way between individual phases and at the level of individual material properties. While these criteria are interlinked, we attempt to address four aspects separately and point out potential routes to resolve them.

- (i). A thermodynamic model should obey basic thermodynamic identities, such as Maxwell's relations, and should be physically reasonable, i.e., approach correct limits at low or high T or P , especially if a model is used for extrapolations beyond the range of the thermodynamic assessment of the phases. As we discuss in Sections 2.1 through 2.3 in detail and demonstrate in Section 4.1.2, significant differences exist in the formulation of the Birch-Murnaghan–Mie-Debye–Grüneisen [Stixrude and Lithgow-Bertelloni, 2011] and Caloric–Modified-Tait [Holland et al., 2013] models, in particular for heat capacity. While the caloric model based on a polynomial expansion agrees much better with experimental data for heat capacity (Figure 4.3), the fact that the Debye model shows the correct asymptotic behavior of the Dulong-Petit limit at high T , makes this model more suitable for extrapolation. Nevertheless, poor representation of experimental data by the latter (Figure 4.3) is an issue of concern. Use of the Kieffer model [Kieffer, 1979a,b] could significantly improve the situation, while maintaining thermodynamic self-consistency [e.g., Jacobs and de Jong, 2007, Jacobs et al., 2013], but its calibration for a sufficient number of phases of geological interest has not yet been undertaken.
- (ii). In assessing available data for the endmembers, a significant number of parameters need to be fit, with strong correlation between different parameters, e.g., the bulk modulus and its pressure derivative from compression experiments

[Angel, 2000], or between enthalpy and entropy when using phase equilibrium constraints [Gottschalk, 1996, Powell and Holland, 1985]. Fitting of parameters has been performed sequentially [e.g., Stixrude and Lithgow-Bertelloni, 2005a, 2011] or simultaneously [e.g., Holland and Powell, 2011, Kennett and Jackson, 2009] and this choice strongly influences the parameter values, even for relatively well characterized phases. Using periclase as an example, significant differences in the properties that determine the Grüneisen parameter (Figure 2.4) exist between the assessments by Stixrude and Lithgow-Bertelloni [2011] and Kennett and Jackson [2009], which in turn strongly influence inferred mantle properties, ranging from the adiabatic gradient to seismic velocities [Connolly and Khan, 2016]. However, adjusting parameters for specific phases only – with the goal to improve agreement with individual observations [e.g., Kurnosov et al., 2017] – may compromise the integrity of the dataset, i.e., its internal consistency and applicability [Connolly, 2009].

For example, a comparison of phase assemblages in the bulk oceanic crust with different datasets of the Birch-Murnaghan–Mie-Debye–Grüneisen model [Stixrude and Lithgow-Bertelloni, 2011, Xu et al., 2008] illustrates that small differences in thermodynamic parameters have a large influence on phase stability fields (Figure A.1). The occurrence of akimotoite in bulk oceanic crust when using the database of Stixrude and Lithgow-Bertelloni [2011] that is not predicted with the database of Xu et al. [2008] can be traced to small changes in the thermodynamic properties of the bridgmanite endmembers and jadeite-majorite. In contrast to bulk oceanic crust, phase relations in pyrolite or depleted mantle remain rather insensitive to these differences in the dataset. Such unexpected behavior suggests that the thermodynamic model by Stixrude and Lithgow-Bertelloni [2011] is sufficiently well constrained for peridotitic bulk composition, dominated by MgO and SiO₂, but with only minor quantities of FeO, CaO, Al₂O₃ and Na₂O. For higher contents of Al₂O₃, CaO and Na₂O, uncertainties and discrepancies in the endmember or mixing properties propagate to the composition of interest and limit the applicability of the database. Phase assemblages computed for other bulk compositions, e.g., for other terrestrial planets [e.g., Sohl and Schubert, 2015], therefore require critical examination of the predictions.

- (iii). In the treatment of solution phases, the parametrization of excess contribution to mixing properties remains among the most influential factors. The model of Stixrude and Lithgow-Bertelloni [2005b, 2011] uses pair-wise interactions only (*cf.* Section 2.6), as proposed by Powell and Holland [1993] and Berman and Aranovich [1996] for robust extrapolation outside the composition and T -space of experimental constraints. Although some thermodynamic models for mineral solutions use inter-site interaction parameters that may be further augmented by T - or P -dependence [e.g., Holland and Powell, 2003], available data for mantle phases are limited, and given uncertainties in calorimetric measurements (Figure 4.8) only in few cases more complex representations of the excess mixing properties would be warranted.

For endmembers of solutions that are not studied, unstable, or fictitious, i.e.,

introduced as convenient compositional endmember, the assessment relies on extrapolations from the solution model to the endmember composition or on reciprocal systematics [Holland and Powell, 1998, 2011, Stixrude and Lithgow-Bertelloni, 2005b]. The latter approach usually provides fictitious results that may be corrected by enthalpic and/or entropic increments when experimental data or natural observations are available [Powell, 1987], whereas the extrapolation from a solution model makes the endmember and solution properties mutually dependent with shared uncertainty [e.g., Holland and Powell, 2011], ultimately affecting phase relations. The significant differences in the phase diagram for the forsterite-fayalite join computed with various models and databases (Figure 4.9) illustrate the sensitivity to endmember parametrization, in this case due to the unstable Fe-wadsleyite endmember. Additional experiments or simulations for compositions along the $\text{Mg}_2\text{SiO}_4\text{-Fe}_2\text{SiO}_4$ binary would be required to better constrain the phase diagram and to stabilize the thermodynamic assessment of unstable endmembers.

- (iv). Issues of coverage or completeness of the dataset are critical when phases are expected to occur that are not included in the database. A sodium aluminosilicate with nepheline composition (*cf.* Section 5.1), for example, is an important sodium host in the bulk oceanic crust to pressures above 40 GPa [e.g., Ricolleau et al., 2010], but – in contrast to Holland et al. [2013] – not assessed in the database of Stixrude and Lithgow-Bertelloni [2011]. In this situation, the chemical component in question is predicted to be hosted in a different phase (metastably) leading to overestimated phase proportions and erroneous phase composition and physical properties, in this case the stability of Ca-ferrite. Often, integration of new endmembers into a solution can significantly change physical properties within the solution. By adding an FeAlO_3 -component to bridgmanite, the agreement between computed elastic profiles of the pyrolite model and seismic profiles has improved significantly [Kurnosov et al., 2017]. However, the influence of this additional component on phase stability has not been investigated and would probably require a revised assessment of all endmembers in the bridgmanite solution, or a wider reassessment of phases that confine its stability field [e.g., Connolly, 2009].

7.2 Consequences for Geophysical Applications

The development of thermodynamic models of mantle petrology has been largely driven by the desire to interpret seismic observations in terms of the chemical composition and temperature of Earth's mantle. Such efforts started for 1D profiles [e.g., Ita and Stixrude, 1992, Vacher et al., 1998] (*cf.* Section 6.2) before shifting to lateral heterogeneity imaged by tomography [e.g., Schuberth et al., 2009b, Trampert et al., 2004]. Similar to the discussion on the homogeneous vs. a mechanically heterogeneous state of the mantle (Section 6.2.2), the viability of a chemical boundary within the mantle [e.g., Duffy and Anderson, 1989, Kellogg et al., 1999] remains a matter of debate, with divergent conclusions [e.g., Kurnosov et al., 2017, Murakami et al., 2012, Ricolleau et al., 2009, Wang et al., 2015]. Twenty years ago, Vacher et al. [1998]

inferred that it is not possible to distinguish between a layered and a uniform mantle based on existing data, and this notion continues to hold to date. It is further supported by a recent stochastic study, evaluating the effects of uncertainties in the assessed thermodynamic parameters on resulting 1-D mantle structure in terms of adiabatic, density and seismic velocity profiles [Connolly and Khan, 2016].

Given the practical uncertainties in the context of formulating a thermodynamic model and parameters, and their implications for mantle structure, Connolly and Khan [2016] suggest that many of the conclusions that have been drawn from matching density and elastic profiles between seismology and thermodynamic models present an overinterpretation of results. This concerns, in particular, the inversion of seismic profiles in terms of temperature and composition [e.g., Cammarano et al., 2011, Cobden et al., 2009, Matas et al., 2007]. The problem is enhanced by the inherent non-uniqueness of inversion, especially in terms of composition [e.g., Afonso et al., 2013]. Even a probabilistic Bayesian approach to inversion [e.g., Afonso et al., 2015, Drilleau et al., 2013, Khan et al., 2011] cannot provide useful constraints on mantle structure. Here we advocate a complementary route to extend our knowledge about the state of the mantle that combines forward models in geodynamics and seismology.

7.2.1 Geodynamic Equation-of-State

An intrinsic problem of coupling thermodynamics and geodynamics arises from the fact that physical properties can change discontinuously across phase transitions, which causes conceptual and numerical complications in the conservation equations of fluid dynamics. Let us consider a univariant (or nearly univariant) phase transition with negative Clapeyron slope, similar to the ringwoodite breakdown. If material is advected across this transition, ringwoodite decomposes to bridgmanite and periclase under the absorption of latent heat, cooling the mineral assemblage. In a thermally isolated system, temperature decreases and the assemblage is expected to transform back to ringwoodite; in practice, the heat balance in an isolated system moderates the reaction progress making it essentially continuous, i.e., divariant. To overcome this singularity problem in geodynamics, effective parameters have been introduced that smear discontinuities in heat capacity and thermal expansivity that enter the energy equation, lifting singularities and dampening numerical instabilities that may arise otherwise. This can be achieved either by using a phase function that accounts for a finite width of the phase transition [e.g., Nakagawa et al., 2009, Richter, 1973, Schubert et al., 1975] or by evaluating thermodynamic properties on a dense discrete grid and then averaging over several nodes or evaluating derivatives numerically [e.g., Afonso et al., 2015, Nakagawa et al., 2009].

An alternative solution to the singularity problem is to formulate the thermodynamic model and geodynamic conservation equations with fundamental variables that are continuous through a phase transition such as pressure and entropy. The energy equation in geodynamics can be formulated in terms of the corresponding thermodynamic potential – enthalpy [e.g., Schubert et al., 2001]. With pressure being a fundamental variable in the enthalpy method, its determination in the geodynamic code needs to be performed self-consistently as well, accounting for hydro-

static [Cammarano, 2013] and dynamic pressure [Connolly, 2009], i.e., going beyond a depth-pressure conversion that is typically applied in geodynamic studies [e.g., Bull et al., 2009, Nakagawa et al., 2012]. Complementary, Connolly [2009] has proposed a formulation of geodynamic equations-of-state in terms of internal energy, with the variables volume and entropy. To account for discontinuous or rapid volume changes, Connolly [2009] included a dilation term in the continuity equation. While the enthalpy method has been used with success in studies of magma dynamics [Dannberg and Heister, 2016, Hebert et al., 2009, Katz, 2008, Keller and Katz, 2016], neither this approach nor the internal energy formulation of Connolly [2009] have been applied in mantle convection.

7.2.2 Forward Seismic Models

Thermodynamic models can serve as a tool for geophysical predictions that are testable against observations or indirect inferences such as tomographic images. Geodynamic predictions may include synthetic seismic structures, but using density alone, for example, geoid undulations and their time variations can be computed, leading to predictions of the rate of true polar wander [Schaber et al., 2009].

The classical approach of assessing geodynamic models are qualitative comparisons of their spectral characteristics with tomographic images [e.g., Becker and Boschi, 2002, Bull et al., 2009, Nakagawa et al., 2010]. Such interpretations rely on approximate, often oversimplified linear scaling relations between T and elastic parameters [e.g., Bower et al., 2013, Bull et al., 2010, Bunge and Davies, 2001]. A thermodynamic model, by contrast, provides access to the full non-linear relation between those parameters. Non-linear effects are particularly strong in the vicinity of phase transitions [e.g., Ritsema et al., 2009b, Stixrude and Lithgow-Bertelloni, 2007, Styles et al., 2011], where small lateral differences in temperature control progress of phase transformations or can result in different equilibrium assemblages (e.g., Figure 5.7). The spectral characteristics of 3D thermal and associated elastic structures, derived from the same geodynamic model, have been shown to differ significantly [Schuberth et al., 2009b] due to non-linear effects from ubiquitous phase transitions. The importance of phase relations when interpreting tomographic images in terms of thermal structure must be emphasized, and even in constructing 1D seismic reference profiles, non-linear effects of laterally differing phase assemblages are likely to introduce a potential bias at depths of major phase transitions [e.g., Styles et al., 2011].

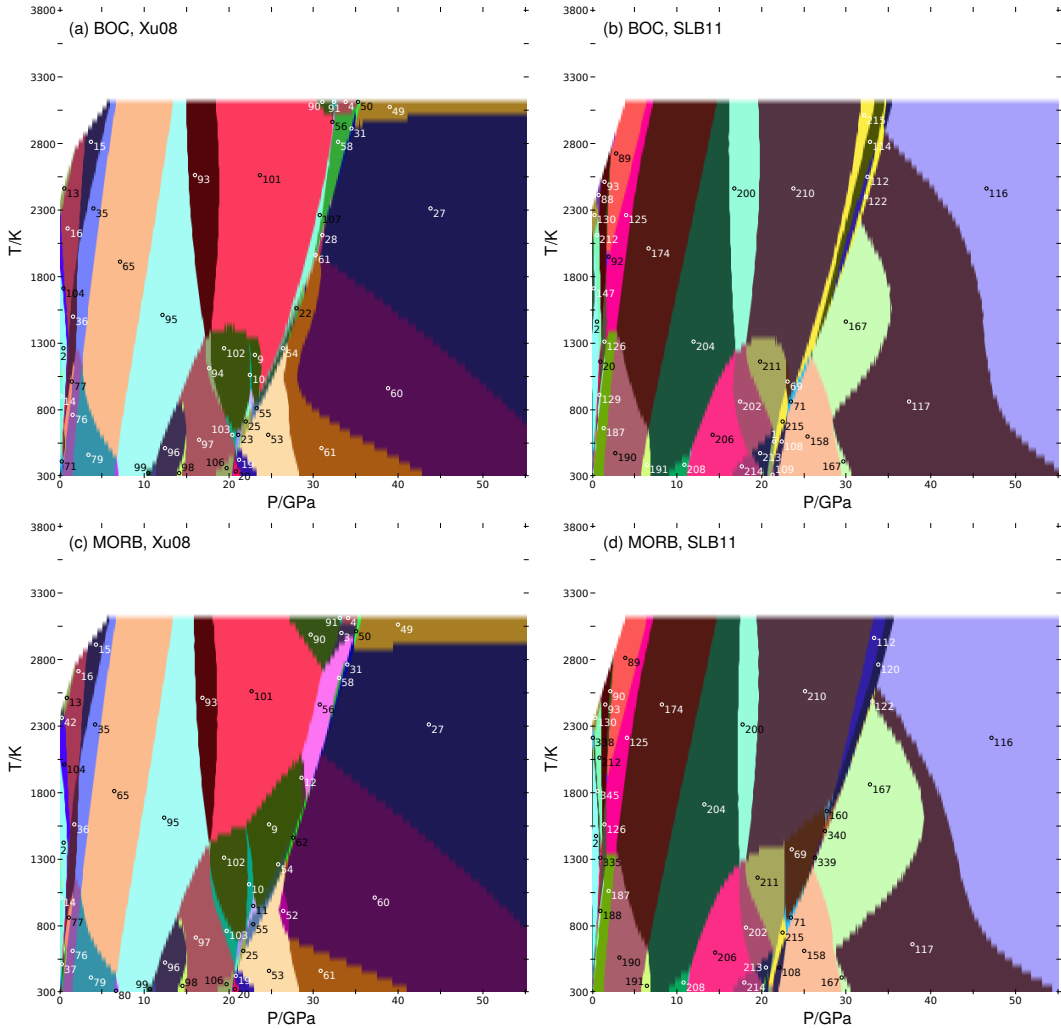
The amplitudes of seismic anomalies in tomographic images are influenced by damping, limited resolution, and non-uniqueness due to uneven source-receiver distribution and the necessity to regularize the inversions. Therefore, geodynamic results require “tomographic filtering” to ensure consistency in quantitative comparisons [e.g., Davies et al., 2012, Schuberth et al., 2009a].

A strategy to address ambiguity problems of tomographic inversion and their interpretation is the prediction of synthetic seismic data, e.g., travel time residuals, based on the results of geodynamic simulations, which can then directly be compared to observations. This requires techniques that go beyond the infinite-frequency approximation of ray tracing [e.g., Davies et al., 2015, Davies and Bunge,

2001] and account for wave field effects, such as wave front healing. Solving the full 3D (an-)elastic wave equation on elastic models based on geodynamic simulations will allow for a self-consistent characterization of wave field effects on a global [Schuberth et al., 2015] and regional scale [Maguire et al., 2016], and for a test of geophysical hypotheses directly against seismological observations [Schuberth et al., 2012].

Appendix A

Database Differences



We have observed large differences between the phase diagrams for bulk oceanic crust (Table 5.1) predicted with the database of [Stixrude and Lithgow-Bertelloni \[2011\]](#) (Figure 5.13) and that of basalt in [Xu et al. \[2008\]](#). In order to compare and analyze these discrepancies we have performed four sets of calculations, using both the databases of [Stixrude and Lithgow-Bertelloni \[2011\]](#) and [Xu et al. \[2008\]](#) and two different sets of basalt compositions: bulk oceanic crust of [Chemia et al. \[2015\]](#) and basalt of [Presnall and Hoover \[1987\]](#). Using the database of [Xu et al. \[2008\]](#) and the basalt composition of [Presnall and Hoover \[1987\]](#), we reproduce the phase diagram of [Xu et al. \[2008\]](#) well (Figure A.1).

Figure A.1: P - T phase diagrams computed for two basaltic compositions: BOC (Table 5.1) in the top row and a mid-ocean ridge basalt by [Presnall and Hoover \[1987\]](#), reduced to six components, as used by [Xu et al. \[2008\]](#) (lower row). Computations used 0.1 GPa and 50 K grid spacing. Phase relations have been calculated with the Mie-Debye-Grüneisen-Birch-Murnaghan model using the thermodynamic dataset of [Xu et al. \[2008\]](#) (left column) and [Stixrude and Lithgow-Bertelloni \[2011\]](#) (right column). The phase fields with the same numbers in the left and right columns represent different phase assemblages; consult Table B.4 for the left column and Table B.3 for the right column. In panels (a) and (c) the following phase assemblages occur: (2) fsp+ol+opx+cpx, (3) capv+gt+st+br+ppv, (4) capv+ak+gt+st+br+ppv, (9) capv+gt+st+fp, (10) ri+capv+gt+st+fp, (11) capv+ak+gt+st+fp, (12) capv+gt+st+br+fp, (13) fsp+opx+qz, (14) fsp+ol+cpx+qz, (15) opx+cpx+qz, (16) fsp+opx+cpx+qz, (19) capv+ak+st+cf, (20) ri+capv+ak+st+cf, (22) capv+gt+st+cf, (23) ri+capv+gt+st+cf, (25) capv+ak+gt+st+cf, (27) capv+st+br+cf, (28) capv+ak+st+br+cf, (31) capv+gt+st+br+cf, (35) cpx+gt+qz, (36) fsp+cpx+gt+qz, (37) fsp+ol+cpx+gt+qz, (42) fsp+opx, (49) capv+st+br+ppv+cf, (50) capv+gt+st+br+ppv+cf, (52) capv+st+fp+cf, (53) capv+ak+st+fp+cf, (54) capv+gt+st+fp+cf, (55) capv+ak+gt+st+fp+cf, (56) capv+gt+st+br, (58) capv+ak+gt+st+br, (60) capv+st+br+fp+cf, (61) capv+ak+st+br+fp+cf, (62) capv+gt+st+br+fp+cf, (65) cpx+gt+coes, (71) fsp+ol+cpx+gt+ky, (76) cpx+gt+qz+ky, (77) fsp+cpx+gt+qz+ky, (79) cpx+gt+coes+ky, (80) cpx+gt+st+ky, (90) capv+gt+st+ppv, (91) capv+ak+gt+st+ppv, (93) gt+st, (94) ri+gt+st, (95) cpx+gt+st, (96) wa+cpx+gt+st, (97) ri+cpx+gt+st, (98) wa+ri+cpx+gt+st, (99) cpx+hpcpx+gt+st, (101) capv+gt+st, (102) ri+capv+gt+st, (103) ri+cpx+capv+gt+st, (104) fsp+opx+cpx, (106) ri+cpx+ak+gt+st, (107) capv+ak+gt+st. In panels (b) and (d) the following phase assemblages are predicted: (2) fsp+ol+opx+cpx, (20) fsp+opx+cpx+gt, (69) capv+gt+st+fp, (71) capv+ak+gt+st+fp, (88) fsp+opx+qz, (89) cpx+qz, (90) fsp+cpx+qz, (92) opx+cpx+qz, (93) fsp+opx+cpx+qz, (108) capv+ak+st+cf, (109) ri+capv+ak+st+cf, (112) capv+gt+st+cf, (114) capv+ak+gt+st+cf, (116) capv+st+br+cf, (117) capv+ak+st+br+cf, (120) capv+gt+st+br+cf, (122) capv+ak+gt+st+br+cf, (125) cpx+gt+qz, (126) fsp+cpx+gt+qz, (129) fsp+opx+cpx+gt+qz, (130) fsp+opx, (147) fsp+ol+opx, (158) capv+ak+st+fp+cf, (160) capv+gt+st+br, (167) capv+ak+st+br+fp+cf, (174) cpx+gt+coes, (187) cpx+gt+qz+ky, (188) fsp+cpx+gt+qz+ky, (190) cpx+gt+coes+ky, (191) cpx+gt+st+ky, (200) gt+st, (202) ri+gt+st, (204) cpx+gt+st, (206) ri+cpx+gt+st, (208) cpx+hpcpx+gt+st, (210) capv+gt+st, (211) ri+capv+gt+st, (212) fsp+opx+cpx, (213) ri+ak+gt+st, (214) ri+cpx+ak+gt+st, (215) capv+ak+gt+st, (335) fsp+sp+opx+cpx+gt, (338) fsp+sp+opx, (339) capv+gt+st+fp+cf, (340) capv+gt+st+pv+fp+cf, (345) fsp+sp+opx+cpx.

Appendix B

Tables

Table B.1: Summary of symbols and notations used in the text.

Description	Symbol	SI Units
Thermodynamic Potentials		
Internal Energy	E	J mol^{-1}
Enthalpy	H	J mol^{-1}
Gibbs energy	G	J mol^{-1}
Additional Gibbs energy in Landau model	G_L	J mol^{-1}
Helmholtz energy	A	J mol^{-1}
Interaction energy in solution model	W	J mol^{-1}
First-Order Derivatives		
Pressure	P	Pa
Phase transition pressure	P_{tr}	Pa
Thermodynamic temperature	T	K
Molar Volume	V	$\text{m}^3 \text{mol}^{-1}$
Total Volume	V_{tot}	m^3
Maximum volume of disorder in Landau model	$V_{L,\text{max}}$	$\text{m}^3 \text{mol}^{-1}$
Entropy	S	$\text{J K}^{-1} \text{mol}^{-1}$
Configurational entropy	S_{cf}	$\text{J K}^{-1} \text{mol}^{-1}$
Elastic Parameters		
Isothermal compressibility	β	Pa^{-1}
Isothermal bulk modulus	K	Pa
Adiabatic bulk modulus	κ	Pa
Adiabatic shear modulus	μ	Pa
P-wave velocity	v_p	m s^{-1}
S-wave velocity	v_s	m s^{-1}
Mass density	ρ	kg m^{-3}
Thermal Parameters		
Thermal expansivity	α	K^{-1}
Heat capacity at constant pressure	C_P	$\text{J K}^{-1} \text{mol}^{-1}$
Heat capacity at constant volume	C_V	$\text{J K}^{-1} \text{mol}^{-1}$
Maximum entropy of disorder in Landau model	$S_{L,\text{max}}$	$\text{J K}^{-1} \text{mol}^{-1}$
Critical temperature	T_C	K
<i>continued on next page</i>		...

Table B.1 <i>continued from previous page</i>		
Description	Symbol	SI Units
Debye temperature	θ_D	K
Einstein temperature	θ_E	K
Grüneisen parameter	γ	
Logarithmic volume derivative of the Grüneisen parameter	q	
Other Quantities		
Molar Mass	M	kg mol ⁻¹
Total Mass	M_{tot}	kg
Number of atoms per formula unit	N	
Mole fraction	x	
Mole amount	X	mol
Shear strain derivative of the Grüneisen parameter	η_S	
Third order Debye function	D_3	
Landau model order parameter	Q	
Solution model endmember size parameter	d	
Subscript for reference conditions	X_0	
Subscript for elastic part	X_{el}	
Subscript for thermal part	X_{th}	
Subscript for ordered phase used in Landau model	X_{ord}	
Subscript for disordered phase used in Landau model	X_{dis}	

Table B.2: Endmember and solution phases in the dataset of [Stixrude and Lithgow-Bertelloni \[2011\]](#). Solution entropies are symmetric except for internal disorder of endmembers.

Phase	Endmember	Formula
Plagioclase feldspar (fsp)	Anorthite (an)	$(\text{Ca})(\text{Al}_2\text{Si}_2)\text{O}_8$
	Albite (ab)	$(\text{Na})(\text{AlSi}_3)\text{O}_8$
Spinel (sp)	Spinel (sp)	$(\text{MgAl}_7)(\text{Mg}_3\text{Al})\text{O}_{16}$
	Hercynite (hc)	$(\text{FeAl}_7)(\text{Fe}_3\text{Al})\text{O}_{16}$
Olivine (ol)	Forsterite (fo)	$(\text{Mg}_2)\text{SiO}_4$
	Fayalite (fa)	$(\text{Fe}_2)\text{SiO}_4$
Wadsleyite (wa)	Mg-Wadsleyite (mgwa)	$(\text{Mg}_2)\text{SiO}_4$
	Fe-Wadsleyite (fewa)	$(\text{Fe}_2)\text{SiO}_4$
Ringwoodite (ri)	Mg-Ringwoodite (mgri)	$(\text{Fe}_2)\text{SiO}_4$
	Fe-Ringwoodite (feri)	$(\text{Fe}_2)\text{SiO}_4$
Orthopyroxene (opx)	Enstatite (en)	$(\text{Mg})(\text{Mg})\text{Si}_2\text{O}_6$
	Ferrosilite (fs)	$(\text{Fe})(\text{Fe})\text{Si}_2\text{O}_6$
	Mg-Tschermak (mgts)	$(\text{Mg})(\text{Al})\text{SiAlO}_6$
	Ortho-Diopside (odi)	$(\text{Ca})(\text{Mg})\text{Si}_2\text{O}_6$
Clinopyroxene (cpx)	Diopside (di)	$(\text{Ca})(\text{Mg})(\text{Si}_2)\text{O}_6$
	Hedenbergite (he)	$(\text{Ca})(\text{Fe})(\text{Si}_2)\text{O}_6$
	Clinoenstatite (cen)	$(\text{Mg})(\text{Mg})(\text{Si}_2)\text{O}_6$
	Ca-Tschermak (cats)	$(\text{Ca})(\text{Al})(\text{SiAl})\text{O}_6$
	Jadeite (jd)	$(\text{Na})(\text{Al})(\text{Si}_2)\text{O}_6$
HP-Clinopyroxene (hpcpx)	HP-Clinoenstatite (hpcen)	$(\text{Mg}_2)\text{Si}_2\text{O}_6$
	HP-Clinoferrosilite (hpcfs)	$(\text{Fe}_2)\text{Si}_2\text{O}_6$
Ca-Perovskite (capv)		CaSiO_3
Akimotoite (ak)	Mg-Akimotoite (mgak)	$(\text{Mg})(\text{Si})\text{O}_3$
	Fe-Akimotoite (feak)	$(\text{Fe})(\text{Si})\text{O}_3$
Garnet (gt)	Corundum (co)	$(\text{Al})(\text{Al})\text{O}_3$
	Pyrope (py)	$(\text{Mg}_3)(\text{Al})(\text{Al})\text{Si}_3\text{O}_{12}$
	Almandine (al)	$(\text{Fe}_3)(\text{Al})(\text{Al})\text{Si}_3\text{O}_{12}$
	Grossular (gr)	$(\text{Ca}_3)(\text{Al})(\text{Al})\text{Si}_3\text{O}_{12}$
	Mg-Majorite (mj)	$(\text{Mg}_3)(\text{Mg})(\text{Si})\text{Si}_3\text{O}_{12}$
	Jadeite-Majorite (jdmj)	$(\text{Na}_2\text{Al})(\text{Al})(\text{Si})\text{Si}_3\text{O}_{12}$
α Quartz (aqz)		SiO_2
β Quartz (qz)		SiO_2
Coesite (coes)		SiO_2
Stishovite (st)		SiO_2
Seifertite (sf)		SiO_2
Bridgmanite (br)	Mg-Bridgmanite (mgbr)	$(\text{Mg})(\text{Si})\text{O}_3$
	Fe-Bridgmanite (febr)	$(\text{Fe})(\text{Si})\text{O}_3$
	Al-Bridgmanite (albr)	$(\text{Al})(\text{Al})\text{O}_3$
Post-Perovskite (ppv)	Mg-Post-Perovskite (mppv)	$(\text{Mg})(\text{Si})\text{O}_3$
	Fe-Post-Perovskite (fppv)	$(\text{Fe})(\text{Si})\text{O}_3$
	Al-Post-Perovskite (appv)	$(\text{Al})(\text{Al})\text{O}_3$
Ferropericlase (fp)	Periclase (pe)	$(\text{Mg})\text{O}$
...	<i>continued on next page</i>	

Table B.2 *continued from previous page*

Phase	Endmember	Formula
	Wüstite (wu)	(Fe)O
Ca-Ferrite (cf)	Mg-Ca-Ferrite (mgcf)	(Mg)(Al)AlO ₄
	Fe-Ca-Ferrite (fecf)	(Fe)(Al)AlO ₄
	Na-Ca-Ferrite (nacf)	(Na)(Si)AlO ₄
Kyanite (ky)		Al ₂ SiO ₅
Nepheline (neph)		NaAlSiO ₄

Table B.3: Numbering of stable phase assemblages in phase diagrams for (reduced) pyrolite compositions (Figures 5.2, 5.3, 5.4, 5.5, 5.6 and 5.7), depleted mantle (Figure 5.12) and bulk oceanic crust (Figure 5.13), and the right panels of Figure A.1). Phase abbreviations are listed in Table B.2. Gaps in numbering correspond to phase assemblages that do not occur at a significant number of grid points.

Id	Phases in Stable Assemblage
0	ol, opx, cpx
1	ri, capv, ak, gt, st
2	fsp, ol, opx, cpx
3	sp, ol, opx, cpx
4	ol, gt
6	wa, gt
7	ol, wa, gt
8	ri, gt
9	sp, ri, gt
10	wa, ri, gt
12	ol, opx, gt
14	ol, cpx, gt
15	wa, cpx, gt
16	ol, wa, cpx, gt
20	fsp, opx, cpx, gt
21	ol, opx, cpx, gt
26	ol, hpcpx, gt
27	wa, hpcpx, gt
28	ri, hpcpx, gt
30	ol, ri, hpcpx, gt
31	wa, ri, hpcpx, gt
32	ol, cpx, hpcpx, gt
33	wa, cpx, hpcpx, gt
34	ol, wa, cpx, hpcpx, gt
35	ri, cpx, hpcpx, gt
36	ol, ri, cpx, hpcpx, gt
37	wa, ri, cpx, hpcpx, gt
39	ri, capv, gt
44	capv, ak, fp
45	ri, capv, ak, fp
46	gt, fp
47	ol, gt, fp
48	wa, gt, fp
49	ol, wa, gt, fp
50	ri, gt, fp
52	wa, ri, gt, fp
54	ol, opx, gt, fp
56	ol, cpx, gt, fp
65	ri, capv, gt, fp
66	capv, ak, gt, fp
...	<i>continued on next page</i>

Table B.3 *continued from previous page*

Id	Phases in Stable Assemblage
67	ri, capv, ak, gt, fp
68	capv, ak, st, fp
69	capv, gt, st, fp
71	capv, ak, gt, st, fp
72	ri, ak, gt
74	capv, br, fp
75	capv, ak, br, fp
76	gt, br, fp
77	capv, gt, br, fp
79	capv, ak, gt, br, fp
80	capv, ak, st, br, fp
83	ri, capv, ak, gt
84	capv, ppv, fp
85	gt, ppv, fp
88	fsp, opx, qz
89	cpx, qz
90	fsp, cpx, qz
92	opx, cpx, qz
93	fsp, opx, cpx, qz
94	capv, br, ppv, fp
97	ri, capv, ak, cf
108	capv, ak, st, cf
109	ri, capv, ak, st, cf
112	capv, gt, st, cf
114	capv, ak, gt, st, cf
116	capv, st, br, cf
117	capv, ak, st, br, cf
120	capv, gt, st, br, cf
122	capv, ak, gt, st, br, cf
124	capv, sf, br, cf
125	cpx, gt, qz
126	fsp, cpx, gt, qz
129	fsp, opx, cpx, gt, qz
130	fsp, opx
132	capv, st, ppv, cf
133	ri, gt, br
137	ri, capv, gt, br
138	capv, sf, ppv, cf
142	ol, opx
146	capv, st, br, ppv, cf
147	fsp, ol, opx
149	capv, sf, br, ppv, cf
156	capv, ak, fp, cf
157	ri, capv, ak, fp, cf
...	<i>continued on next page</i>

Table B.3 *continued from previous page*

Id	Phases in Stable Assemblage
158	capv, ak, st, fp, cf
160	capv, gt, st, br
163	capv, br, fp, cf
164	capv, ak, br, fp, cf
165	capv, gt, br, fp, cf
167	capv, ak, st, br, fp, cf
168	capv, ppv, fp, cf
170	capv, br, ppv, fp, cf
174	cpx, gt, coes
179	ol, opx, cpx, ky
183	ol, opx, cpx, gt, ky
187	cpx, gt, qz, ky
188	fsp, cpx, gt, qz, ky
190	cpx, gt, coes, ky
191	cpx, gt, st, ky
195	ol, cpx
198	ri, capv, ak
199	ri, capv, ak, st
200	gt, st
201	wa, gt, st
202	ri, gt, st
203	wa, ri, gt, st
204	cpx, gt, st
205	wa, cpx, gt, st
206	ri, cpx, gt, st
207	wa, ri, cpx, gt, st
208	cpx, hpcpx, gt, st
210	capv, gt, st
211	ri, capv, gt, st
212	fsp, opx, cpx
213	ri, ak, gt, st
214	ri, cpx, ak, gt, st
215	capv, ak, gt, st
216	wa, opx, cpx
219	ol, wa, opx, cpx
221	ol, ri, opx, cpx
222	ol, wa, hpcpx, gt
224	wa, capv, gt
226	opx, fp
227	ol, opx, fp
235	ak, fp
236	ri, ak, fp
237	ol, hpcpx
238	sp, gt, fp
...	<i>continued on next page</i>

Table B.3 *continued from previous page*

Id	Phases in Stable Assemblage
239	wa, cpx, gt, fp
242	wa, capv, gt, fp
243	ak, gt, fp
245	wa, hpcpx
246	st, fp
248	capv, st, fp
250	ak, st, fp
251	ol, wa, hpcpx
254	ri, hpcpx
257	ol, ri, hpcpx
258	wa, ri, hpcpx
260	br, fp
263	ri, sf
265	ak, br, fp
268	st, br, fp
269	capv, st, br, fp
270	ak, st, br, fp
273	ol, cpx, hpcpx
274	ppv, fp
278	wa, cpx, hpcpx
279	ol, wa, cpx, hpcpx
280	ol, qz
283	ri, cpx, hpcpx
285	ol, ri, cpx, hpcpx
286	sf, ppv, fp
289	wa, ri, cpx, hpcpx
291	br, ppv, fp
294	wa, br
295	ri, br
296	ri, capv, br
298	sp, ol, opx
299	wa, opx
300	ri, st, br
302	ri, capv, st, br
303	br, fp, cf
304	ak, br, fp, cf
306	ppv, fp, cf
307	br, ppv, fp, cf
311	ol, ri, opx
312	wa, ak
313	ol, opx, ky
314	ol, opx, gt, ky
316	ri, ak
317	ol, opx, ak
...	<i>continued on next page</i>

Table B.3 *continued from previous page*

Id	Phases in Stable Assemblage
321	wa, st
322	ri, st
323	wa, ri, st
325	ri, cpx, st
326	wa, ri, cpx, st
329	ri, cpx, hpcpx, st
330	ri, capv, st
332	ri, ak, st
335	fsp, sp, opx, cpx, gt
338	fsp, sp, opx
339	capv, gt, st, fp, cf
340	capv, gt, st, pv, fp, cf
345	fsp, sp, opx, cpx

Table B.4: Numbering of stable phase assemblages in computed phase diagrams for bulk oceanic crust and mid-ocean ridge basalt compositions using the thermodynamic dataset of Xu et al. [2008], used in the left panels of Figure A.1. Phase abbreviations are listed in Table B.2. Gaps in numbering correspond to phase assemblages that do not occur at a significant number of grid points.

Id	Phases in Stable Assemblage
2	fsp, ol, opx, cpx
3	capv, gt, st, br, ppv
4	capv, ak, gt, st, br, ppv
9	capv, gt, st, fp
10	ri, capv, gt, st, fp
11	capv, ak, gt, st, fp
12	capv, gt, st, br, fp
13	fsp, opx, qz
14	fsp, ol, cpx, qz
15	opx, cpx, qz
16	fsp, opx, cpx, qz
19	capv, ak, st, cf
20	ri, capv, ak, st, cf
22	capv, gt, st, cf
23	ri, capv, gt, st, cf
25	capv, ak, gt, st, cf
27	capv, st, br, cf
28	capv, ak, st, br, cf
31	capv, gt, st, br, cf
35	cpx, gt, qz
36	fsp, cpx, gt, qz
37	fsp, ol, cpx, gt, qz
42	fsp, opx
49	capv, st, br, ppv, cf
50	capv, gt, st, br, ppv, cf
52	capv, st, fp, cf
53	capv, ak, st, fp, cf
54	capv, gt, st, fp, cf
55	capv, ak, gt, st, fp, cf
56	capv, gt, st, br
58	capv, ak, gt, st, br
60	capv, st, br, fp, cf
61	capv, ak, st, br, fp, cf
62	capv, gt, st, br, fp, cf
65	cpx, gt, coes
71	fsp, ol, cpx, gt, ky
76	cpx, gt, qz, ky
77	fsp, cpx, gt, qz, ky
79	cpx, gt, coes, ky
80	cpx, gt, st, ky
...	<i>continued on next page</i>

Table B.4 *continued from previous page*

Id	Phases in Stable Assemblage
90	capv, gt, st, ppv
91	capv, ak, gt, st, ppv
93	gt, st
94	ri, gt, st
95	cpx, gt, st
96	wa, cpx, gt, st
97	ri, cpx, gt, st
98	wa, ri, cpx, gt, st
99	cpx, hpcpx, gt, st
101	capv, gt, st
102	ri, capv, gt, st
103	ri, cpx, capv, gt, st
104	fsp, opx, cpx
106	ri, cpx, ak, gt, st
107	capv, ak, gt, st

Acknowledgements

I thank Gerd Steinle-Neumann, David Dolejš, Bernhard Schuberth and Hans-Peter Bunge, who accompanied this thesis project with helpful suggestions, debugging aid and many ideas for extensions and improvements.

I greatly appreciated helpful discussions with Stephan Barth, Zurab Chemia, Lorenzo Colli, Dan Frost, Brian Kennett, Mainak Mookherjee, Robert Myhill and Jens Weismüller.

For invaluable moral support and real-life logistics, without which I could not have spent so much time and energy on this work, I want to express my profound gratitude to my friends and relatives Andreas Amereller, Stephan Barth, Silvia Chust, Wilfried Chust and Martin Tschöpe.

Bibliography

- L. Adam and T. Otheim. Elastic laboratory measurements and modeling of saturated basalts. *Journal of Geophysical Research*, 118(3):840–851, 2013. doi:[10.1002/jgrb.50090](https://doi.org/10.1002/jgrb.50090).
- J. C. Afonso, J. Fulla, W. L. Griffin, Y. Yang, A. G. Jones, J. A. D. Connolly, and S. Y. O'Reilly. 3-D multiobservable probabilistic inversion for the compositional and thermal structure of the lithosphere and upper mantle. I: a priori petrological information and geophysical observables. *Journal of Geophysical Research*, 118:2586–2617, 2013. doi:[10.1002/jgrb.50124](https://doi.org/10.1002/jgrb.50124).
- J. C. Afonso, S. Zlotnik, and P. Diez. An efficient and general approach for implementing thermodynamic phase equilibria information in geophysical and geodynamic studies. *Geochemistry, Geophysics, Geosystems*, 16(10):3767–3777, 2015. doi:[10.1002/2015GC006031](https://doi.org/10.1002/2015GC006031).
- T. J. Ahrens. Petrologic properties of the upper 670 km of the Earth's mantle; geophysical implications. *Physics of the Earth and Planetary Interiors*, 7(2):187–198, June 1973. doi:[10.1016/0031-9201\(73\)90008-3](https://doi.org/10.1016/0031-9201(73)90008-3).
- M. Akaogi. Phase transitions of minerals in the transition zone and upper part of the lower mantle. *GSA Special Papers*, 421:1–13, 2007. doi:[10.1130/2007.2421\(01\)](https://doi.org/10.1130/2007.2421(01)).
- M. Akaogi, A. Navrotsky, T. Yagii, and S. Akimoto. Pyroxene-garnet transformation: Thermochemistry and elasticity of garnet solid solutions, and application to a pyrolite mantle. In M. H. Manghnani and Y. Syono, editors, *High-Pressure Research in Mineral Physics*, Geophysical Monograph Series, pages 251–260. Terra Scientific Publishing Company, 1987. doi:[10.1029/GM039p0251](https://doi.org/10.1029/GM039p0251).
- M. Akaogi, M. Yano, Y. Tejima, M. Iijima, and H. Kojitani. High-pressure transitions of diopside and wollastonite: Phase equilibria and thermochemistry of $\text{CaMgSi}_2\text{O}_6$, CaSiO_3 and CaSi_2O_5 - CaTiSiO_5 system. *Physics of the Earth and Planetary Interiors*, 143-144:145–156, 2004. doi:[10.1016/j.pepi.2003.08.008](https://doi.org/10.1016/j.pepi.2003.08.008).
- C. J. Allègre and D. L. Turcotte. Implications of a two-component marble-cake mantle. *Nature*, 323:123–127, 1986. doi:[10.1038/323123a0](https://doi.org/10.1038/323123a0).
- D. L. Anderson. Petrology of the mantle. *Mineralogical Society of America Special Paper*, 3:85–93, February 1970.

- D. Andrault, M. A. Bouhifd, J. P. Itié, and P. Richet. Compression and amorphization of $(\text{Mg,Fe})_2\text{SiO}_4$ olivines: An X-ray diffraction study up to 10 GPa. *Physics and Chemistry of Minerals*, 22(2):99–107, 1995. doi:[10.1007/BF00202469](https://doi.org/10.1007/BF00202469).
- D. Andrault, N. Bolfan-Casanova, and N. Guignot. Equation of state of lower mantle $(\text{Al,Fe})\text{-MgSiO}_3$ perovskite. *Earth and Planetary Science Letters*, 193:501–508, 2001. doi:[10.1016/S0012-821X\(01\)00506-4](https://doi.org/10.1016/S0012-821X(01)00506-4).
- R. J. Angel. Equations of state. *Reviews in Mineralogy and Geochemistry*, 41(1):35–59, 2000. doi:[10.2138/rmg.2000.41.2](https://doi.org/10.2138/rmg.2000.41.2).
- I. Ansara, A. T. Dinsdale, and M. H. Rand. COST 507: Thermochemical database for light metal alloys. Technical report, European Commission, 1998.
- K. M. Arredondo and M. I. Billen. The effects of phase transitions and compositional layering in two-dimensional kinematic models of subduction. *Journal of Geodynamics*, 100:159–174, 2016. doi:[10.1016/j.jog.2016.05.009](https://doi.org/10.1016/j.jog.2016.05.009).
- N. W. Ashcroft and N. D. Mermin. *Solid State Physics*. Saunders, Philadelphia, 1976.
- P. D. Asimow and M. S. Ghiorso. Algorithmic modifications extending melts to calculate subsolidus phase relations. *American Mineralogist*, 83:1127–1132, 1998. doi:[10.2138/am-1998-9-1022](https://doi.org/10.2138/am-1998-9-1022).
- M. Asplund, N. Grevesse, A. J. Sauval, and P. Scott. The chemical composition of the sun. *Annual Review of Astronomy and Astrophysics*, 47:481–522, 2009. doi:[10.1146/annurev.astro.46.060407.145222](https://doi.org/10.1146/annurev.astro.46.060407.145222).
- M. B. Baker and J. R. Beckett. The origin of abyssal peridotites: A reinterpretation of constraints based on primary bulk compositions. *Earth and Planetary Science Letters*, 171:49–61, 1999. doi:[10.1016/S0012-821X\(99\)00130-2](https://doi.org/10.1016/S0012-821X(99)00130-2).
- C. Bale, P. Chartrand, S. Degterov, G. Eriksson, K. Hack, R. B. Mahfoud, J. Melançon, A. Pelton, and S. Petersen. FactSage thermochemical software and databases. *Calphad*, 26(2):189–228, 2002. doi:[10.1016/S0364-5916\(02\)00035-4](https://doi.org/10.1016/S0364-5916(02)00035-4).
- C. Bale, E. Bélisle, P. Chartrand, S. Dechterov, G. Eriksson, K. Hack, I.-H. Jung, Y.-B. Kang, J. Melançon, A. Pelton, C. Robelin, and S. Petersen. FactSage thermochemical software and databases – recent developments. *Calphad*, 33(2):295–311, 2009. doi:[10.1016/j.calphad.2008.09.009](https://doi.org/10.1016/j.calphad.2008.09.009).
- C. W. Bale and G. Eriksson. Metallurgical thermochemical databases – A review. *Canadian Metallurgical Quarterly*, 29(2):105–132, 1990. doi:[10.1179/cmqr.1990.29.2.105](https://doi.org/10.1179/cmqr.1990.29.2.105).
- T. W. Becker and L. Boschi. A comparison of tomographic and geodynamic mantle models. *Geochemistry, Geophysics, Geosystems*, 3:2001GC000168, 2002. doi:[10.1029/2001GC000168](https://doi.org/10.1029/2001GC000168).
- M. Benichou, J. M. Gauthier, G. Hentges, and G. Ribiere. The efficient solution of large-scale linear programming problems – some algorithmic techniques and computational results. *Mathematical Programming*, 13(1):280–322, 1977. doi:[10.1007/BF01584344](https://doi.org/10.1007/BF01584344).

- A. Benisek, K. Etzel, and L. Cemic. Thermodynamic mixing behavior of synthetic Ca-tschermak – diopside pyroxene solid solutions: II. Heat of mixing and activity-composition relationships. *Physics and Chemistry of Minerals*, 34:747–755, 2007. doi:[10.1007/s00269-007-0192-4](https://doi.org/10.1007/s00269-007-0192-4).
- R. G. Berman and L. Y. Aranovich. Optimized standard state and solution properties of minerals – I. Model calibration for olivine, orthopyroxene, cordierite, garnet, and ilmenite in the system FeO-MgO-CaO-Al₂O₃-TiO₂-SiO₂. *Contributions to Mineralogy and Petrology*, 126(1-2):1–24, 1996. doi:[10.1007/s004100050232](https://doi.org/10.1007/s004100050232).
- F. Birch. Finite elastic strain of cubic crystals. *Physical Review*, 71(11):809–824, 1947. doi:[10.1103/PhysRev.71.809](https://doi.org/10.1103/PhysRev.71.809).
- S. R. Bohlen and A. L. Boettcher. The quartz \rightleftharpoons coesite transformation: A precise determination and the effects of other components. *Journal of Geophysical Research*, 87(B8):7073–7078, August 1982. doi:[10.1029/JB087iB08p07073](https://doi.org/10.1029/JB087iB08p07073).
- M. G. Bostock. The Moho in subduction zones. *Tectonophysics*, 609:547–557, 2013. doi:[10.1016/j.tecto.2012.07.007](https://doi.org/10.1016/j.tecto.2012.07.007).
- M. A. Bouhifd, D., G. Fiquet, and P. Richet. Thermal expansion of forsterite up to the melting point. *Geophysical Research Letters*, 23(10):1143–1146, 1996. doi:[10.1029/96GL01118](https://doi.org/10.1029/96GL01118).
- D. J. Bower, M. Gurnis, and D. Sun. Dynamic origins of seismic wavespeed variation in D". *Physics of the Earth and Planetary Interiors*, 214:74–86, 2013. doi:[10.1016/j.pepi.2012.10.004](https://doi.org/10.1016/j.pepi.2012.10.004).
- J. P. Brandenburg and P. E. van Keken. Deep storage of oceanic crust in a vigorously convecting mantle. *Journal of Geophysical Research*, 112:B06403, 2007. doi:[10.1029/2006JB004813](https://doi.org/10.1029/2006JB004813).
- E. Brosh, G. Makov, and R. Z. Shneck. Application of CALPHAD to high pressures. *CALPHAD*, 31(2):173–185, 2007. doi:[10.1016/j.calphad.2006.12.008](https://doi.org/10.1016/j.calphad.2006.12.008).
- J. M. Brown and T. J. Shankland. Thermodynamic parameters in the Earth as determined from seismic profiles. *Geophysical Journal International*, 66(3):579–596, 1981. doi:[10.1111/j.1365-246X.1981.tb04891.x](https://doi.org/10.1111/j.1365-246X.1981.tb04891.x).
- A. Bull, A. McNamara, and J. Ritsema. Synthetic tomography of plume clusters and thermochemical piles. *Earth and Planetary Science Letters*, 278:152–162, 2009. doi:[10.1016/j.epsl.2008.11.018](https://doi.org/10.1016/j.epsl.2008.11.018).
- A. Bull, A. McNamara, T. Becker, and J. Ritsema. Global scale models of the mantle flow field predicted by synthetic tomography models. *Physics of the Earth and Planetary Interiors*, 182:129–138, 2010. doi:[10.1016/j.pepi.2010.03.004](https://doi.org/10.1016/j.pepi.2010.03.004).
- H.-P. Bunge. Low plume excess temperature and high core heat flux inferred from non-adiabatic geotherms in internally heated mantle circulation models. *Physics of the Earth and Planetary Interiors*, 153(1-3):3–10, 2005. doi:[10.1016/j.pepi.2005.03.017](https://doi.org/10.1016/j.pepi.2005.03.017).

- H.-P. Bunge and J. H. Davies. Tomographic images of a mantle circulation model. *Geophysical Research Letters*, 28(1):77–80, 2001. doi:[10.1029/2000GL011804](https://doi.org/10.1029/2000GL011804).
- L. Burdick and D. L. Anderson. Interpretation of velocity profiles of the mantle. *Journal of Geophysical Research*, 80(8):1070–1074, March 1975. doi:[10.1029/JB080i008p01070](https://doi.org/10.1029/JB080i008p01070).
- F. Cammarano. A short note on the pressure-depth conversion for geophysical interpretation. *Geophysical Research Letters*, 40:4834–4838, 2013. doi:[10.1002/grl.50887](https://doi.org/10.1002/grl.50887).
- F. Cammarano, B. Romanowicz, L. Stixrude, C. Lithgow-Bertelloni, and W. Xu. Inferring the thermochemical structure of the upper mantle from seismic data. *Geophysical Journal International*, 179:1169–1185, 2009. doi:[10.1111/j.1365-246X.2009.04338.x](https://doi.org/10.1111/j.1365-246X.2009.04338.x).
- F. Cammarano, P. Tackley, and L. Boschi. Seismic, petrological and geodynamical constraints on thermal and compositional structure of the upper mantle: Global thermochemical models. *Geophysical Journal International*, 187(3):1301–1318, 2011. doi:[10.1111/j.1365-246X.2011.05223.x](https://doi.org/10.1111/j.1365-246X.2011.05223.x).
- D. Canil. Stability of clinopyroxene at pressure-temperature conditions of the transition region. *Physics of the Earth and Planetary Interiors*, 86:25–34, 1994. doi:[10.1016/0031-9201\(94\)05059-7](https://doi.org/10.1016/0031-9201(94)05059-7).
- M. A. Carpenter, R. Powell, and E. K. Salje. Thermodynamics of nonconvergent cation ordering in minerals; I, an alternative approach. *American Mineralogist*, 79(11-12): 1053–1067, 1994.
- K. Catalli, S.-H. Shim, and V. Prakapenka. Thickness and Clapeyron slope of the post-perovskite boundary. *Nature*, 462(10):782–785, 2009. doi:[10.1038/nature08598](https://doi.org/10.1038/nature08598).
- Y. A. Chang, S. Chen, F. Zhang, X. Yan, F. Xie, R. Schmid-Fetzer, and W. A. Oates. Phase diagram calculation: Past, present and future. *Progress in Materials Science*, 49:313–345, 2004. doi:[10.1016/S0079-6425\(03\)00025-2](https://doi.org/10.1016/S0079-6425(03)00025-2).
- J. Chantel. *Measurement of elastic properties of silicates at realistic mantle pressures*. PhD thesis, Universität Bayreuth, 2012.
- J. Chantel, D. J. Frost, C. A. McCammon, Z. Jing, and Y. Wang. Acoustic velocities of pure and iron-bearing magnesium silicate perovskite measured to 25 GPa and 1200 K. *Geophysical Research Letters*, 39:L19307, 2012. doi:[10.1029/2012GL053075](https://doi.org/10.1029/2012GL053075).
- Z. Chemia, D. Dolejš, and G. Steinle-Neumann. Thermal effects of variable material properties and metamorphic reactions in a three-component subducting slab. *Journal of Geophysical Research*, 120:6823–6845, 2015. doi:[10.1002/2015JB012080](https://doi.org/10.1002/2015JB012080).
- U. R. Christensen and A. W. Hofmann. Segregation of subducted oceanic crust in the convecting mantle. *Journal of Geophysical Research*, 99(B10):19867–19884, 1994. doi:[10.1029/93JB03403](https://doi.org/10.1029/93JB03403).

- U. R. Christensen and D. A. Yuen. Layered convection induced by phase transitions. *Journal of Geophysical Research*, 90(B12):10291–10300, 1985. doi:[10.1029/JB090iB12p10291](https://doi.org/10.1029/JB090iB12p10291).
- L. Chudinovskikh and R. Boehler. High-pressure polymorphs of olivine and the 660-km seismic discontinuity. *Nature*, 411:574–577, 2001. doi:[10.1038/35079060](https://doi.org/10.1038/35079060).
- L. Cobden, S. Goes, F. Cammarano, and J. A. D. Connolly. Thermochemical interpretation of one-dimensional seismic reference models for the upper mantle: Evidence for bias due to heterogeneity. *Geophysical Journal International*, 175:627–648, 2008. doi:[10.1111/j.1365-246X.2008.03903.x](https://doi.org/10.1111/j.1365-246X.2008.03903.x).
- L. Cobden, S. Goes, M. Ravenna, E. Styles, F. Cammarano, K. Gallagher, and J. A. D. Connolly. Thermochemical interpretation of 1-D seismic data for the lower mantle: The significance of nonadiabatic thermal gradients and compositional heterogeneity. *Journal of Geophysical Research*, 114, 2009. doi:[10.1029/2008JB006262](https://doi.org/10.1029/2008JB006262).
- L. H. Cohen and W. Klement. High-low quartz inversion: Determination to 35 kilobars. *Journal of Geophysical Research*, 72(16):4245–4251, August 1967. doi:[10.1029/JZ072i016p04245](https://doi.org/10.1029/JZ072i016p04245).
- R. E. Cohen. Thermodynamic solution properties of aluminous clinopyroxenes: Non-linear least squares refinements. *Geochimica et Cosmochimica Acta*, 50:563–575, 1986. doi:[10.1016/0016-7037\(86\)90105-5](https://doi.org/10.1016/0016-7037(86)90105-5).
- J. A. D. Connolly. Computation of phase equilibria by linear programming: A tool for geodynamic modeling and its application to subduction zone decarbonation. *Earth and Planetary Science Letters*, 236:524–541, 2005. doi:[10.1016/j.epsl.2005-04-033](https://doi.org/10.1016/j.epsl.2005-04-033).
- J. A. D. Connolly. The geodynamic equation of state: What and how. *Geochemistry, Geophysics, Geosystems*, 10(10):Q10014, 2009. doi:[10.1029/2009GC002540](https://doi.org/10.1029/2009GC002540).
- J. A. D. Connolly and D. M. Kerrick. Metamorphic controls on seismic velocity of subducted oceanic crust at 100 – 250 km depth. *Earth and Planetary Science Letters*, 204(1-2):61–74, 2002. doi:[10.1016/S0012-821X\(02\)00957-3](https://doi.org/10.1016/S0012-821X(02)00957-3).
- J. A. D. Connolly and A. Khan. Uncertainty of mantle geophysical properties computed from phase equilibrium models. *Geophysical Research Letters*, 43:5026–5034, 2016. doi:[10.1002/2016GL068239](https://doi.org/10.1002/2016GL068239).
- J. A. D. Connolly and K. Petrini. An automated strategy for calculation of phase diagram sections and retrieval of rock properties as a function of physical conditions. *Journal of Metamorphic Geology*, 20(7):697–708, 2002. doi:[10.1046/j.1525-1314.2002.00398.x](https://doi.org/10.1046/j.1525-1314.2002.00398.x).
- S. Cottaar, T. Heister, I. Rose, and C. Unterborn. BurnMan: A lower mantle mineral physics toolkit. *Geochemistry, Geophysics, Geosystems*, 15:1164–1179, 2014. doi:[10.1002/2013GC005122](https://doi.org/10.1002/2013GC005122).

- C. A. Dalton, C. H. Langmuir, and A. Gale. Geophysical and geochemical evidence for deep temperature variations beneath mid-ocean ridges. *Science*, 344(6179):80–83, 2014. doi:[10.1126/science.1249466](https://doi.org/10.1126/science.1249466).
- J. Dannberg and T. Heister. Compressible magma/mantle dynamics: 3-D, adaptive simulations in ASPECT. *Geophysical Journal International*, 207:1343–1366, 2016. doi:[10.1093/gji/ggw329](https://doi.org/10.1093/gji/ggw329).
- G. B. Dantzig. *Linear Programming and Extensions*. Princeton University Press, 1963.
- D. R. Davies, S. Goes, J. Davies, B. Schuberth, H.-P. Bunge, and J. Ritsema. Reconciling dynamic and seismic models of Earth's lower mantle: The dominant role of thermal heterogeneity. *Earth and Planetary Science Letters*, 353-354(0):253–269, 2012. doi:[10.1016/j.epsl.2012.08.016](https://doi.org/10.1016/j.epsl.2012.08.016).
- D. R. Davies, S. Goes, and H. C. P. Lau. Thermally dominated deep mantle LLSVPs: A review. *The Earth's Heterogeneous Mantle*, pages 441–477, 2015. doi:[10.1007/978-3-319-15627-9_14](https://doi.org/10.1007/978-3-319-15627-9_14).
- G. F. Davies. Geophysical and isotopic constraints on mantle convection: An interim synthesis. *Journal of Geophysical Research*, 89(B7):6017–6040, 1984. doi:[10.1029/JB089iB07p06017](https://doi.org/10.1029/JB089iB07p06017).
- G. F. Davies. Cooling the core and mantle by plume and plate flows. *Geophysical Journal International*, 115(1):132–146, 1993. doi:[10.1111/j.1365-246X.1993.tb05593.x](https://doi.org/10.1111/j.1365-246X.1993.tb05593.x).
- J. H. Davies and H.-P. Bunge. Seismically “fast” geodynamic mantle models. *Geophysical Research Letters*, 28(1):73–76, 2001. doi:[10.1029/2000GL011805](https://doi.org/10.1029/2000GL011805).
- C. de Capitani and T. H. Brown. The computation of chemical equilibrium in complex systems containing non-ideal solutions. *Geochimica et Cosmochimica Acta*, 51:2639–2652, 1987. doi:[10.1016/0016-7037\(87\)90145-1](https://doi.org/10.1016/0016-7037(87)90145-1).
- C. de Capitani and K. Petrakakis. The computation of equilibrium assemblage diagrams with THERIAK/DOMINO software. *American Mineralogist*, 95:1006–1016, 2010. doi:[10.2138/am.2010.3354](https://doi.org/10.2138/am.2010.3354).
- P. Debye. Zur Theorie der spezifischen Wärmen. *Annalen der Physik*, 344(14):789–839, 1912. doi:[10.1002/andp.19123441404](https://doi.org/10.1002/andp.19123441404).
- R. T. Downs, C.-S. Zha, T. S. Duffy, and L. W. Finger. The equation of state of forsterite to 17.2 GPa and effects of pressure media. *American Mineralogist*, 81:51–55, 1996. doi:[10.2138/am-1996-1-207](https://doi.org/10.2138/am-1996-1-207).
- M. Drilleau, É. Beucler, A. Mocquet, O. Verhoeven, G. Moebs, G. Burgos, J.-P. Montagner, and P. Vacher. A Bayesian approach to infer radial models of temperature and anisotropy in the transition zone from surface wave dispersion curves. *Geophysical Journal International*, 195:1165–1183, 2013. doi:[10.1093/gji/ggt284](https://doi.org/10.1093/gji/ggt284).

- T. S. Duffy and D. L. Anderson. Seismic velocities in mantle minerals and the mineralogy of the upper mantle. *Journal of Geophysical Research*, 94(B2):1895–1912, 1989. doi:[10.1029/JB094iB02p01895](https://doi.org/10.1029/JB094iB02p01895).
- A. M. Dziewonski and D. L. Anderson. Preliminary reference Earth model. *Physics of the Earth and Planetary Interiors*, 25:297–356, 1981.
- B. Emmerson and D. McKenzie. Thermal structure and seismicity of subducting lithosphere. *Physics of the Earth and Planetary Interiors*, 163:191–208, 2007. doi:[10.1016/j.pepi.2007.05.007](https://doi.org/10.1016/j.pepi.2007.05.007).
- G. Eriksson and K. Hack. ChemSage – A computer program for the calculation of complex chemical equilibria. *Metallurgical Transactions B*, 21(6):1013–1023, 1990. doi:[10.1007/BF02670272](https://doi.org/10.1007/BF02670272).
- G. Eriksson and E. Rosen. Thermodynamic studies of high-temperature equilibria. 8. General equations for calculations of equilibria in multiphase systems. *Chemica Scripta*, 4(5):193–194, 1973.
- O. Fabrichnaya, S. K. Saxena, P. Richet, and E. F. Westrum. *Thermodynamic Data, Models, and Phase Diagrams in Multicomponent Oxide Systems*. Springer Verlag, 2004.
- O. B. Fabrichnaya. Thermodynamic data for phases in the $FeO - MgO - SiO_2$ system and phase relations in the mantle transition zone. *Physics and Chemistry of Minerals*, 22:323–332, 1995.
- D. W. Fan, W. G. Zhou, C. Q. Liu, Y. G. Liu, F. Wan, Y. S. Xing, J. Liu, L. G. Bai, and H. S. Xie. The thermal equation of state of $(Fe_{0.86}Mg_{0.07}Mn_{0.07})_3Al_2Si_3O_{12}$ almandine. *Mineralogical Magazine*, 73(1):95–102, 2009. doi:[10.1180/minmag.2009.073.1.95](https://doi.org/10.1180/minmag.2009.073.1.95).
- H. Fei, C. Hegoda, D. Yamazaki, M. Wiedenbeck, H. Yurimoto, S. Shcheka, and T. Katsura. High silicon self-diffusion coefficient in dry forsterite. *Earth and Planetary Science Letters*, 345-348:95–103, 2012. doi:[10.1016/j.epsl.2012.06.044](https://doi.org/10.1016/j.epsl.2012.06.044).
- Y. Fei and C. M. Bertka. *Phase transitions in the Earth's mantle and mantle mineralogy*, volume 6 of *Special Publications*, pages 189–207. The Geochemical Society, 1999.
- Y. Fei, S. Saxena, and G. Eriksson. Some binary and ternary silicate solution models. *Contributions to Mineralogy and Petrology*, 94(2):221–229, 1986. doi:[10.1007/BF00592938](https://doi.org/10.1007/BF00592938).
- Y. Fei, J. van Orman, J. Li, W. van Westrenen, C. Sanloup, W. Minarik, K. Hirose, T. Komabayashi, M. Walter, and K. Funakoshi. Experimentally determined post-spinel transformation boundary in Mg_2SiO_4 using MgO as an internal pressure standard and its geophysical implications. *Journal of Geophysical Research*, 109(B2): B02305, 2004. doi:[10.1029/2003JB002562](https://doi.org/10.1029/2003JB002562).
- G. J. Finkelstein, P. K. Dera, S. Jahn, A. R. Oganov, C. M. Holl, Y. Meng, and T. S. Duffy. Phase transitions and equation of state of forsterite to 90 GPa from single-crystal X-ray diffraction and molecular modeling. *American Mineralogist*, 99:35–43, 2014. doi:[10.2138/am.2014.4526](https://doi.org/10.2138/am.2014.4526).

- G. Fiquet, Q. Dewaele, D. Andrault, M. Kunz, and T. L. Bihan. Thermoelastic properties and crystal structure of MgSiO_3 perovskite at lower mantle pressure and temperature conditions. *Geophysical Research Letters*, 27(1):21–24, 2000. doi:[10.1029/1999GL008397](https://doi.org/10.1029/1999GL008397).
- J. J. Forrest and D. Goldfarb. Steepest-edge simplex algorithms for linear programming. *Mathematical Programming*, 57(1):341–374, 1992. doi:[10.1007/BF01581089](https://doi.org/10.1007/BF01581089).
- D. J. Frost. The structure and sharpness of $(\text{Mg,Fe})_2\text{SiO}_4$ phase transformations in the transition zone. *Earth and Planetary Science Letters*, 216(3):313–328, 2003a. doi:[10.1016/S0012-821X\(03\)00533-8](https://doi.org/10.1016/S0012-821X(03)00533-8).
- D. J. Frost. Fe^{2+} -Mg partitioning between garnet, magnesiowüstite, and $(\text{Mg,Fe})_2\text{SiO}_4$ phases of the transition zone. *American Mineralogist*, 88(2-3):387–397, 2003b. doi:[10.2138/am-2003-2-315](https://doi.org/10.2138/am-2003-2-315).
- D. J. Frost. The upper mantle and transition zone. *Elements*, 4(3):171–176, 2008. doi:[10.2113/GSELEMENTS.4.3.171](https://doi.org/10.2113/GSELEMENTS.4.3.171).
- D. J. Frost and F. Langenhorst. The effect of Al_2O_3 on Fe-Mg partitioning between magnesiowüstite and magnesium silicate perovskite. *Earth and Planetary Science Letters*, 199:227–241, 2002. doi:[10.1016/S0012-821X\(02\)00558-7](https://doi.org/10.1016/S0012-821X(02)00558-7).
- K. Fujino, D. Nishio-Hamane, T. Nagai, Y. Seto, Y. Kuwayama, M. Whitaker, H. Ohfuji, T. Shinmei, and T. Irifune. Spin transition, substitution, and partitioning of iron in lower mantle minerals. *Physics of the Earth and Planetary Interiors*, 228:186–191, 2014. doi:[10.1016/j.pepi.2013.12.008](https://doi.org/10.1016/j.pepi.2013.12.008).
- A. Férot and N. Bolfan-Casanova. Water storage capacity in olivine and pyroxene to 14 GPa: Implications for the water content of the Earth's upper mantle and nature of seismic discontinuities. *Earth and Planetary Science Letters*, 349-350:218–230, 2012. doi:[10.1016/j.epsl.2012.06.022](https://doi.org/10.1016/j.epsl.2012.06.022).
- J. Ganguly. *Thermodynamics in Earth and Planetary Sciences*. Springer-Verlag Berlin Heidelberg, 2008. doi:[10.1007/978-3-540-77306-1](https://doi.org/10.1007/978-3-540-77306-1).
- J. Ganguly, A. M. Freed, and S. K. Saxena. Density profiles of oceanic slabs and surrounding mantle: Integrated thermodynamic and thermal modeling, and implications for the fate of slabs at the 660 km discontinuity. *Physics of the Earth and Planetary Interiors*, 172:257–267, 2009. doi:[10.1016/j.pepi.2008.10.005](https://doi.org/10.1016/j.pepi.2008.10.005).
- E. J. Garnero, D. V. Helmberger, and S. P. Grand. Constraining outermost core velocity with SmKS waves. *Geophysical Research Letters*, 20(22):2463–2466, 1993. doi:[10.1029/93GL02823](https://doi.org/10.1029/93GL02823).
- T. Gasparik. Experimentally determined stability of clinopyroxene + garnet + corundum in the system $\text{CaO-MgO-Al}_2\text{O}_3\text{-SiO}_2$. *American Mineralogist*, 69:1025–1035, 1984.
- T. Gasparik. Phase relations in the transition zone. *Journal of Geophysical Research*, 95 (B10):15751–15769, 1990a. doi:[10.1029/JB095iB10p15751](https://doi.org/10.1029/JB095iB10p15751).

- T. Gasparik. A thermodynamic model for the enstatite – diopside join. *American Mineralogist*, 75(9-10):1080–1091, 1990b.
- T. Gasparik. *Phase Diagrams for Geoscientists – An Atlas of the Earth's Interior*. Springer Verlag, 2nd edition, 2003.
- M. S. Ghiorso. Algorithms for the estimation of phase stability in heterogeneous thermodynamic systems. *Geochimica et Cosmochimica Acta*, 58(24):5489–5501, 1994. doi:[10.1016/0016-7037\(94\)90245-3](https://doi.org/10.1016/0016-7037(94)90245-3).
- M. S. Ghiorso and R. O. Sack. Chemical mass transfer in magmatic processes IV. A revised and internally consistent thermodynamic model for the interpolation and extrapolation of liquid-solid equilibria in magmatic systems at elevated temperatures and pressures. *Contributions to Mineralogy and Petrology*, 119(2-3):197–212, 1995. doi:[10.1007/BF00307281](https://doi.org/10.1007/BF00307281).
- S. Goes, F. Cammarano, and U. Hansen. Synthetic seismic signature of thermal mantle plumes. *Earth and Planetary Science Letters*, 218:403–419, 2004. doi:[10.1016/S0012-821X\(03\)00680-0](https://doi.org/10.1016/S0012-821X(03)00680-0).
- M. Gottschalk. Internally consistent thermodynamic data for rock-forming minerals in the system $\text{SiO}_2\text{-TiO}_2\text{-Al}_2\text{O}_3\text{-Fe}_2\text{O}_3\text{-CaO-MgO-FeO-K}_2\text{O-Na}_2\text{O-H}_2\text{O-CO}_2$. *European Journal of Mineralogy*, 9(1):175–223, 1996. doi:[10.1127/ejm/9/1/0175](https://doi.org/10.1127/ejm/9/1/0175).
- B. Grocholski, K. Catalli, S.-H. Shim, and V. Prakapenka. Mineralogical effects on the detectability of the postperovskite boundary. *Proceedings of the National Academy of Sciences*, 109(7):2275–2279, 2012. doi:[10.1073/pnas.1109204109](https://doi.org/10.1073/pnas.1109204109).
- B. Grocholski, S.-H. Shim, and V. B. Prakapenka. Stability, metastability, and elastic properties of a dense silica polymorph, seifertite. *Journal of Geophysical Research*, 118:4745–4757, 2013. doi:[10.1002/jgrb.50360](https://doi.org/10.1002/jgrb.50360).
- S. Gréaux, Y. Kono, N. Nishiyama, T. Kunimoto, K. Wada, and T. Irifune. P - V - T equation of state of $\text{Ca}_3\text{Al}_2\text{Si}_3\text{O}_{12}$ grossular garnet. *Physics and Chemistry of Minerals*, 38: 85–94, 2011. doi:[10.1007/s00269-010-0384-1](https://doi.org/10.1007/s00269-010-0384-1).
- G. D. Gwanmesia, G. Chen, and R. C. Liebermann. Sound velocities in MgSiO_3 -garnet to 8 GPa. *Geophysical Research Letters*, 25(24):4553–4556, 1998. doi:[10.1029/1998GL900189](https://doi.org/10.1029/1998GL900189).
- G. D. Gwanmesia, J. Zhang, K. Darling, J. Kung, B. Li, L. Wang, D. Neuville, and R. C. Liebermann. Elasticity of polycrystalline pyrope $\text{Mg}_3\text{Al}_2\text{Si}_3\text{O}_{12}$ to 9 GPa and 1000 °C. *Physics of the Earth and Planetary Interiors*, 155:179–190, 2006. doi:[10.1016/j.pepi.2005.10.008](https://doi.org/10.1016/j.pepi.2005.10.008).
- G. D. Gwanmesia, L. Wang, R. Triplett, and R. C. Liebermann. Pressure and temperature dependence of the elasticity of pyrope-majorite [$\text{py}_{60}\text{mj}_{40}$ and $\text{py}_{50}\text{mj}_{50}$] garnets solid solution measured by ultrasonic interferometry technique. *Physics of the Earth and Planetary Interiors*, 174:105–112, 2009. doi:[10.1016/j.pepi.2008.07.029](https://doi.org/10.1016/j.pepi.2008.07.029).

- P. M. Harris. Pivot selection methods of the Devex LP code. *Mathematical programming*, 5(1):1–28, 1973. doi:[10.1007/BF01580108](https://doi.org/10.1007/BF01580108).
- R. M. Hazen. Effects of temperature and pressure on the crystal structure of forsterite. *American Mineralogist*, 61(11-12):1280–1293, 1976.
- L. B. Hebert, P. Antoshechkina, P. Asimow, and M. Gurnis. Emergence of a low-viscosity channel in subduction zones through the coupling of mantle flow and thermodynamics. *Earth and Planetary Science Letters*, 278(3-4):243–256, 2009. doi:[10.1016/j.epsl.2008.12.013](https://doi.org/10.1016/j.epsl.2008.12.013).
- G. Helffrich and B. J. Wood. Subregular model for multicomponent solutions. *American Mineralogist*, 74(9-10):1016–1022, 1989.
- C. Herzberg, P. D. Asimow, N. Arndt, Y. Niu, C. M. Lesher, J. G. Fitton, M. J. Cheadle, and A. D. Saunders. Temperatures in ambient mantle and plumes: Constraints from basalts, picrites, and komatiites. *Geochemistry, Geophysics, Geosystems*, 8(2):Q02006, 2007. doi:[10.1029/2006GC001390](https://doi.org/10.1029/2006GC001390).
- R. Hill. Elastic properties of reinforced solids: Some theoretical principles. *Journal of the Mechanics and Physics of Solids*, 11(5):357–372, 1963. doi:[10.1016/0022-5096\(63\)90036-X](https://doi.org/10.1016/0022-5096(63)90036-X).
- M. Hillert and L.-I. Staffansson. The regular solution model for stoichiometric phases and ionic melts. *Acta Chemica Scandinavica*, 24:3618–3626, 1970. doi:[10.3891/acta.chem.scand.24-3618](https://doi.org/10.3891/acta.chem.scand.24-3618).
- K. Hirose, Y. Fei, Y. Ma, and H. Mao. The fate of subducted basaltic crust in the Earth's lower mantle. *Nature*, 397:53–56, 1999. doi:[10.1038/16225](https://doi.org/10.1038/16225).
- K. Hirose, T. Komabayashi, M. Murakami, and K. Funakoshi. In situ measurements of the majorite – akimotoite – perovskite phase transition boundaries in MgSiO₃. *Geophysical Research Letters*, 28(23):4351–4354, 2001. doi:[10.1029/2001GL013549](https://doi.org/10.1029/2001GL013549).
- T. Holland and R. Powell. Activity–composition relations for phases in petrological calculations: An asymmetric multicomponent formulation. *Contributions to Mineralogy and Petrology*, 145(4):492–501, 2003. doi:[10.1007/s00410-003-0464-z](https://doi.org/10.1007/s00410-003-0464-z).
- T. J. B. Holland and R. Powell. An internally consistent thermodynamic data set for phases of petrological interest. *Journal of Metamorphic Geology*, 16:309–343, 1998. doi:[10.1111/j.1525-1314.1998.00140.x](https://doi.org/10.1111/j.1525-1314.1998.00140.x).
- T. J. B. Holland and R. Powell. An improved and extended internally consistent thermodynamic dataset for phases of petrological interest, involving a new equation of state for solids. *Journal of Metamorphic Geology*, 29:333–383, 2011. doi:[10.1111/j.1525-1314.2010.00923.x](https://doi.org/10.1111/j.1525-1314.2010.00923.x).
- T. J. B. Holland, N. F. C. Hudson, R. Powell, and B. Harte. New thermodynamic models and calculated phase equilibria in NCFMAS for basic and ultrabasic compositions through the transition zone into the uppermost lower mantle. *Journal of Petrology*, 54(9):1901–1920, 2013. doi:[10.1093/petrology/egt035](https://doi.org/10.1093/petrology/egt035).

- C. Holzappel, D. C. Rubie, D. J. Frost, and F. Langenhorst. Fe-Mg interdiffusion in (Mg,Fe)SiO₃ perovskite and lower mantle reequilibration. *Science*, 309(5741):1707–1710, 2005. doi:[10.1126/science.1111895](https://doi.org/10.1126/science.1111895).
- S. Huang and J. Chen. Equation of state of pyrope-almandine solid solution measured using a diamond anvil cell and in situ synchrotron x-ray diffraction. *Physics of the Earth and Planetary Interiors*, 228:88–91, 2014. doi:[10.1016/j.pepi.2014.01.014](https://doi.org/10.1016/j.pepi.2014.01.014).
- S. Imada, K. Hirose, T. Komabayashi, T. Suzuki, and Y. Ohishi. Compression of Na_{0.4}Mg_{0.6}Al_{1.6}Si_{0.4}O₄ NAL and Ca-ferrite-type phases. *Physics and Chemistry of Minerals*, 39:525–530, 2012. doi:[10.1007/s00269-012-0508-x](https://doi.org/10.1007/s00269-012-0508-x).
- T. Inoue, T. Irifune, Y. Higo, T. Sanehira, Y. Sueda, A. Yamada, T. Shinmei, D. Yamazaki, J. Ando, K. Funakoshi, and W. Utsumi. The phase boundary between wadsleyite and ringwoodite in Mg₂SiO₄ determined by in situ X-ray diffraction. *Physics and Chemistry of Minerals*, 33:106–114, 2006. doi:[10.1007/s00269-005-0053-y](https://doi.org/10.1007/s00269-005-0053-y).
- T. Irifune and A. E. Ringwood. Phase transformations in a harzburgite composition to 26 GPa: Implications for dynamical behaviour of the subducting slab. *Earth and Planetary Science Letters*, 86(2-4):365–376, 1987. doi:[10.1016/0012-821X\(87\)90233-0](https://doi.org/10.1016/0012-821X(87)90233-0).
- T. Irifune and A. E. Ringwood. Phase transformations in subducted oceanic crust and buoyancy relationships at depths of 600-800 km in the mantle. *Earth and Planetary Science Letters*, 117(1-2):101–110, 1993. doi:[10.1016/0012-821X\(93\)90120-X](https://doi.org/10.1016/0012-821X(93)90120-X).
- T. Irifune and T. Tsuchiya. Phase transitions and mineralogy of the lower mantle. In G. Schubert, editor, *Treatise on Geophysics*, volume 2, chapter 2.03, pages 33–60. Elsevier, 2 edition, 2015.
- T. Irifune, N. Nishiyama, K. Kuroda, T. Inoue, M. Isshiki, W. Utsumi, K. Funakoshi, S. Urakawa, T. Uchida, T. Katsura, and O. Ohtaka. The postspinel phase boundary in Mg₂SiO₄ determined by in situ X-ray diffraction. *Science*, 279:1698–1700, 1998. doi:[10.1126/science.279.5357.1698](https://doi.org/10.1126/science.279.5357.1698).
- T. Ishii, H. Kojitani, and M. Akaogi. Post-spinel transitions in pyrolite and Mg₂SiO₄ and akimotoite-perovskite transition in MgSiO₃: Precise comparison by high-pressure high-temperature experiments with multi-sample cell technique. *Earth and Planetary Science Letters*, 309:185–197, 2011. doi:[10.1016/j.epsl.2011.06.023](https://doi.org/10.1016/j.epsl.2011.06.023).
- J. Ita and S. D. King. Sensitivity of convection with an endothermic phase change to the form of governing equations, initial conditions, boundary conditions, and equation of state. *Journal of Geophysical Research*, 99(B8):15919–15938, 1994. doi:[10.1029/94JB00852](https://doi.org/10.1029/94JB00852).
- J. Ita and S. D. King. The influence of thermodynamic formulation on simulations of subduction zone geometry and history. *Geophysical Research Letters*, 25(9):1463–1466, 1998. doi:[10.1029/98GL51033](https://doi.org/10.1029/98GL51033).

- J. Ita and L. Stixrude. Petrology, elasticity and composition of the mantle transition zone. *Journal of Geophysical Research*, 97(B5):6849–6866, 1992. doi:[10.1029/92JB00068](https://doi.org/10.1029/92JB00068).
- E. Ito and E. Takahashi. Post-spinel transformations in the system $\text{Mg}_2\text{SiO}_4 - \text{Fe}_2\text{SiO}_4$ and some geophysical implications. *Journal of Geophysical Research*, 94(B8):10637–10646, 1989. doi:[10.1029/JB094iB08p10637](https://doi.org/10.1029/JB094iB08p10637).
- E. Ito and H. Yamada. Stability relations of silicate spinels, ilmenites, and perovskites. In *High Pressure Research in Geophysics*. Center for Academic Publishing, Tokyo, 1982.
- J. M. Jackson, S. V. Sinogeikin, and J. D. Bass. Sound velocities and single-crystal elasticity of orthoenstatite to 1073 K at ambient pressure. *Physics of the Earth and Planetary Interiors*, 161:1–12, 2007. doi:[10.1016/j.pepi.2006.11.002](https://doi.org/10.1016/j.pepi.2006.11.002).
- M. H. Jacobs and B. H. de Jong. Placing constraints on phase equilibria and thermophysical properties in the system MgO-SiO_2 by a thermodynamically consistent vibrational method. *Geochimica et Cosmochimica Acta*, 71:3630–3655, 2007. doi:[10.1016/j.gca.2007.05.010](https://doi.org/10.1016/j.gca.2007.05.010).
- M. H. G. Jacobs, R. Schmid-Fetzer, and A. P. van den Berg. An alternative use of Kieffer's lattice dynamics model using vibrational density of states for constructing thermodynamic databases. *Physics and Chemistry of Minerals*, 40:207–227, 2013. doi:[10.1007/s00269-012-0562-4](https://doi.org/10.1007/s00269-012-0562-4).
- R. Jeanloz and S. Morris. Is the mantle geotherm subadiabatic? *Geophysical Research Letters*, 14(4):335–338, 1987. doi:[10.1029/GL014i004p00335](https://doi.org/10.1029/GL014i004p00335).
- F. Jiang, G. D. Gwanmesia, T. I. Dyuzheva, and T. S. Duffy. Elasticity of stishovite and acoustic mode softening under high pressure by Brillouin scattering. *Physics of the Earth and Planetary Interiors*, 172:235–240, 2009. doi:[10.1016/j.pepi.2008.09.017](https://doi.org/10.1016/j.pepi.2008.09.017).
- I. Kantor, L. Dubrovinsky, C. McCammon, G. Steinle-Neumann, A. Kantor, N. Skorodumova, S. Pascarelli, and G. Aquilanti. Short-range order and Fe clustering in $\text{Mg}_{1-x}\text{Fe}_x\text{O}$ under high pressure. *Physical Review B*, 80:014204, 2009. doi:[10.1103/PhysRevB.80.014204](https://doi.org/10.1103/PhysRevB.80.014204).
- S. Karato. Importance of anelasticity in the interpretation of seismic tomography. *Geophysical Research Letters*, 20(15):1623–1626, 1993. doi:[10.1029/93GL01767](https://doi.org/10.1029/93GL01767).
- C. Kato, K. Hirose, T. Komabayashi, H. Ozawa, and Y. Ohishi. NAL phase in K-rich portions of the lower mantle. *Geophysical Research Letters*, 40:5085–5088, 2013. doi:[10.1002/grl.50966](https://doi.org/10.1002/grl.50966).
- T. Kato, Y. Kinoshita, N. Nishiyama, K. Wada, C. Zhou, and T. Irifune. Magnesium silicate perovskite coexisting with ringwoodite in harzburgite stagnated at the lowermost mantle transition zone. *Physics of the Earth and Planetary Interiors*, 232:26–29, 2014. doi:[10.1016/j.pepi.2014.03.009](https://doi.org/10.1016/j.pepi.2014.03.009).

- T. Katsura and E. Ito. The system Mg_2SiO_4 - Fe_2SiO_4 at high pressure and temperatures: Precise determination of stability of olivine, modified spinel. *Journal of Geophysical Research*, 94(B11):15663–15670, 1989. doi:[10.1029/JB094iB11p15663](https://doi.org/10.1029/JB094iB11p15663).
- T. Katsura, H. Yamada, T. Shinmei, et al. Post-spinel transition in Mg_2SiO_4 determined by high P - T in situ X-ray diffractometry. *Physics of the Earth and Planetary Interiors*, 136(1-2):11–24, 2003. doi:[10.1016/S0031-9201\(03\)00019-0](https://doi.org/10.1016/S0031-9201(03)00019-0).
- T. Katsura, H. Yamada, O. Nishikawa, M. Song, A. Kubo, T. Shinmei, S. Yokoshi, Y. Aizawa, T. Yoshino, M. J. Walter, E. Ito, and K. Funakoshi. Olivine-wadsleyite transition in the system $(\text{Mg,Fe})_2\text{SiO}_4$. *Journal of Geophysical Research*, 109(B2):B02209, 2004. doi:[10.1029/2003JB002438](https://doi.org/10.1029/2003JB002438).
- T. Katsura, S. Yokoshi, K. Kawabe, A. Shatskiy, M. A. G. M. Manthilake, S. Zhai, H. Fukui, H. A. C. I. Hegoda, T. Yoshino, D. Yamazaki, T. Matsuzaki, A. Yoneda, E. Ito, M. Sugita, N. Tomioka, K. Hagiya, A. Nozawa, and K. Funakoshi. P - V - T relations of MgSiO_3 perovskite determined by in situ X-ray diffraction using a large-volume high-pressure apparatus. *Geophysical Research Letters*, 36:L01305, 2009. doi:[10.1029/2008GL035658](https://doi.org/10.1029/2008GL035658).
- T. Katsura, A. Yoneda, D. Yamazaki, T. Yoshino, and E. Ito. Adiabatic temperature profile in the mantle. *Physics of the Earth and Planetary Interiors*, 183:212–218, 2010. doi:[10.1016/j.pepi.2010.07.001](https://doi.org/10.1016/j.pepi.2010.07.001).
- R. F. Katz. Magma dynamics with the enthalpy method: Benchmark solutions and magmatic focusing at mid-ocean ridges. *Journal of Petrology*, 49(12):2099–2121, 2008. doi:[10.1093/petrology/egn058](https://doi.org/10.1093/petrology/egn058).
- T. Keller and R. F. Katz. The role of volatiles in reactive melt transport in the asthenosphere. *Journal of Petrology*, 57(6):1073–1108, 2016. doi:[10.1093/petrology/egw030](https://doi.org/10.1093/petrology/egw030).
- L. H. Kellogg and D. L. Turcotte. Mixing and the distribution of heterogeneities in a chaotically convecting mantle. *Journal of Geophysical Research*, 95(B1):421–432, 1990. doi:[10.1029/JB095iB01p00421](https://doi.org/10.1029/JB095iB01p00421).
- L. H. Kellogg, B. H. Hager, and R. D. van der Hilst. Compositional stratification in the deep mantle. *Science*, 283(5409):1881–1884, 1999. doi:[10.1126/science.283.5409.1881](https://doi.org/10.1126/science.283.5409.1881).
- B. L. N. Kennett and H.-P. Bunge. *Geophysical Continua: Deformation in the Earth's Interior*. Cambridge University Press, 2008.
- B. L. N. Kennett and I. Jackson. Optimal equations of state for mantle minerals from simultaneous non-linear inversion of multiple datasets. *Physics of the Earth and Planetary Interiors*, 176:98–108, 2009. doi:[10.1016/j.pepi.2009-04-005](https://doi.org/10.1016/j.pepi.2009-04-005).
- B. L. N. Kennett, E. R. Engdahl, and R. Buland. Constraints on seismic velocities in the Earth from traveltimes. *Geophysical Journal International*, 122(1):108–124, 1995. doi:[10.1111/j.1365-246X.1995.tb03540.x](https://doi.org/10.1111/j.1365-246X.1995.tb03540.x).

- A. Khan, L. Boschi, and J. A. D. Connolly. Mapping the Earth's thermochemical and anisotropic structure using global surface wave data. *Journal of Geophysical Research*, 116:B01301, 2011. doi:[10.1029/2010JB007828](https://doi.org/10.1029/2010JB007828).
- S. W. Kieffer. Thermodynamics and lattice vibrations of minerals: 1. mineral heat capacities and their relationships to simple lattice vibrational models. *Reviews of Geophysics and Space Physics*, 17(1):1–19, 1979a. doi:[10.1029/RG017i001p00001](https://doi.org/10.1029/RG017i001p00001).
- S. W. Kieffer. Thermodynamics and lattice vibrations of minerals: 2. vibrational characteristics of silicates. *Reviews of Geophysics and Space Physics*, 17(1):20–34, 1979b. doi:[10.1029/RG017i001p00020](https://doi.org/10.1029/RG017i001p00020).
- Y. Kim, M. S. Miller, F. Pearce, and R. W. Clayton. Seismic imaging of the Cocos plate subduction zone system in central Mexico. *Geochemistry, Geophysics, Geosystems*, 13, 2012. doi:[10.1029/2012GC004033](https://doi.org/10.1029/2012GC004033).
- S. Klemme and H. S. O'Neill. The near-solidus transition from garnet Iherzolite to spinel Iherzolite. *Contributions to Mineralogy and Petrology*, 138(3):237–248, 2000. doi:[10.1007/s004100050560](https://doi.org/10.1007/s004100050560).
- Y. Kobayashi, T. Kondo, E. Ohtani, N. Hirao, N. Miyajima, T. Yagi, T. Nagase, and T. Kikegawa. Fe-Mg partitioning between (Mg,Fe)SiO₃ post-perovskite, perovskite, and magnesiowüstite in the Earth's lower mantle. *Geophysical Research Letters*, 32: L19301, 2005. doi:[10.1029/2005GL023257](https://doi.org/10.1029/2005GL023257).
- T. Komabayashi. Thermodynamics of melting relations in the system Fe-FeO at high pressure: Implications for oxygen in the Earth's core. *Journal of Geophysical Research*, 119(5):4164–4177, 2014. doi:[10.1002/2014JB010980](https://doi.org/10.1002/2014JB010980).
- Y. Kono, S. Gréaux, Y. Higo, H. Ohfuji, and T. Irifune. Pressure and temperature dependences of elastic properties of grossular garnet up to 17 GPa and 1650 K. *Journal of Earth Science*, 21(5):782–791, 2010. doi:[10.1007/s12583-010-0112-2](https://doi.org/10.1007/s12583-010-0112-2).
- A. M. Koziol and R. C. Newton. Redetermination of the anorthite breakdown reaction and improvement of the plagioclase-garnet-Al₂SiO₅-quartz geobarometer. *American Mineralogist*, 73:216–223, 1988.
- A. Kroupa. Modelling of phase diagrams and thermodynamic properties using Calphad method – development of thermodynamic databases. *Computational Materials Science*, 66:3–13, 2013. doi:[10.1016/j.commatsci.2012.02.003](https://doi.org/10.1016/j.commatsci.2012.02.003).
- Y. Kudoh and Y. Takeuchi. The crystal structure of forsterite Mg₂SiO₄ under high pressure up to 149 kbar. *Zeitschrift für Kristallographie*, 171:291–302, 1985.
- J. Kung, B. Li, T. Uchida, Y. Wang, D. Neuville, and R. C. Liebermann. In situ measurements of sound velocities and densities across the orthopyroxene → high-pressure clinopyroxene transition in MgSiO₃ at high pressure. *Physics of the Earth and Planetary Interiors*, 147:27–44, 2004. doi:[10.1016/j.pepi.2004.05.008](https://doi.org/10.1016/j.pepi.2004.05.008).

- A. Kurnosov, H. Marquardt, D. Frost, T. B. Ballaran, and L. Ziberna. Evidence for a Fe³⁺-rich pyrolitic lower mantle from Al-Fe-bridgmanite elasticity data. *Nature*, 543: 543–546, 2017. doi:[10.1038/nature21390](https://doi.org/10.1038/nature21390).
- V. Lacivita, A. Erba, R. Dovesi, and P. D'Arco. Elasticity of grossular-andradite solid solution: An ab initio investigation. *Physical Chemistry, Chemical Physics*, 16(29): 15331–15338, 2014. doi:[10.1039/C4CP01597E](https://doi.org/10.1039/C4CP01597E).
- S. Lee and R. B. Meyer. Computations of the phase equilibrium, elastic constants, and viscosities of a hard-rod nematic liquid crystal. *The Journal of Chemical Physics*, 84: 3443, 1986. doi:[10.1063/1.450228](https://doi.org/10.1063/1.450228).
- C. E. Lemke. The dual method of solving the linear programming problem. *Naval Research Logistics*, 1(1):36–47, 1954. doi:[10.1002/nav.3800010107](https://doi.org/10.1002/nav.3800010107).
- B. Li and J. Zhang. Pressure and temperature dependence of elastic wave velocity of MgSiO₃ perovskite and the composition of the lower mantle. *Physics of the Earth and Planetary Interiors*, 151:143–154, 2005. doi:[10.1016/j.pepi.2005-02-004](https://doi.org/10.1016/j.pepi.2005-02-004).
- M. Li and A. K. McNamara. The difficulty for subducted oceanic crust to accumulate at the Earth's core-mantle boundary. *Journal of Geophysical Research*, 118:1807–1816, 2013. doi:[10.1002/jgrb.50156](https://doi.org/10.1002/jgrb.50156).
- K. D. Litasov and E. Ohtani. Phase relations in hydrous MORB at 18–28 gpa: Implications for heterogeneity of the lower mantle. *Physics of the Earth and Planetary Interiors*, 150(4):239–263, 2005. doi:[10.1016/j.pepi.2004.10.010](https://doi.org/10.1016/j.pepi.2004.10.010).
- L.-G. Liu. High pressure NaAlSiO₄: The first silicate calcium ferrite isotype. *Geophysical Research Letters*, 4(5):183–186, 1977. doi:[10.1029/GL004i005p00183](https://doi.org/10.1029/GL004i005p00183).
- Z. Liu, T. Irifune, S. Gréaux, T. Arimoto, T. Shinmei, and Y. Higo. Elastic wave velocity of polycrystalline Mj₈₀Py₂₀ garnet to 21 GPa and 2000 K. *Physics and Chemistry of Minerals*, 42:213–222, 2015. doi:[10.1007/s00269-014-0712-y](https://doi.org/10.1007/s00269-014-0712-y).
- W. Loewenstein. Configurational entropy of binary silicate solid solutions. *American Mineralogist*, 39:92–96, 1954.
- H. L. Lukas, E. T. Henig, and B. Zimmermann. Optimization of phase diagrams by a least squares method using simultaneously different types of data. *Calphad*, 1(3): 225–236, 1977. doi:[10.1016/0364-5916\(77\)90002-5](https://doi.org/10.1016/0364-5916(77)90002-5).
- H. L. Lukas, S. G. Fries, and B. Sundman. *Computational Thermodynamics: The Calphad Method*. Cambridge University Press, 2007.
- R. Maguire, J. Ritsema, P. E. van Keken, A. Fichtner, and S. Goes. P- and S-wave delays caused by thermal plumes. *Geophysical Journal International*, 206(2):1169–1178, 2016. doi:[10.1093/gji/ggw187](https://doi.org/10.1093/gji/ggw187).
- P. Maierová, T. Chust, G. Steinle-Neumann, O. Čadek, and H. Čížková. The effect of variable thermal diffusivity on kinematic models of subduction. *Journal of Geophysical Research*, 117:B07202, 2012. doi:[10.1029/2011JB009119](https://doi.org/10.1029/2011JB009119).

- Z. Mao, D. Fan, J.-F. Lin, J. Yang, S. N. Tkachev, K. Zhuravlev, and V. B. Prakapenka. Elasticity of single-crystal olivine at high pressures and temperatures. *Earth and Planetary Science Letters*, 426:204–215, 2015. doi:[10.1016/j.epsl.2015.06.045](https://doi.org/10.1016/j.epsl.2015.06.045).
- J. Matas. *Modélisation thermochimique des propriétés de solides a hautes températures et hautes pressions*. PhD thesis, Charles University Prague and École Normale Supérieure Lyon, 1999.
- J. Matas and M. S. T. Bukowinski. On the anelastic contribution to the temperature dependence of lower mantle seismic velocities. *Earth and Planetary Science Letter*, 259:51–65, 2007. doi:[10.1016/j.epsl.2007.04.028](https://doi.org/10.1016/j.epsl.2007.04.028).
- J. Matas, J. Bass, Y. Ricard, E. Mattern, and M. S. T. Bukowinski. On the bulk composition of the lower mantle: Predictions and limitations from generalized inversion of radial seismic profiles. *Geophysical Journal International*, 170(2):764–780, 2007. doi:[10.1111/j.1365-246X.2007.03454.x](https://doi.org/10.1111/j.1365-246X.2007.03454.x).
- K. Matsuzaka, M. Akaogi, T. Suzuki, and T. Suda. Mg-Fe partitioning between silicate spinel and magnesiowustite at high pressure: Experimental determination and calculation of phase relations in the system Mg_2SiO_4 - Fe_2SiO_4 . *Physics and Chemistry of Minerals*, 27(5):310–319, 2000. doi:[10.1007/s002690050260](https://doi.org/10.1007/s002690050260).
- B. J. McBride, M. J. Zehe, and S. Gordon. NASA Glenn coefficients for calculating thermodynamic properties of individual species. NASA/TP 2002-211556, NASA Glenn Research Center, Cleveland, Ohio, 2002.
- C. McCammon, L. Dubrovinsky, O. Narygina, I. Kantor, X. Wu, K. Glazyrin, I. Sergueev, and A. Chumakov. Low-spin Fe^{2+} in silicate perovskite and a possible layer at the base of the lower mantle. *Physics of the Earth and Planetary Interiors*, 180:215–221, 2010. doi:[10.1016/j.pepi.2009.10.012](https://doi.org/10.1016/j.pepi.2009.10.012).
- C. M. McDonald and C. A. Floudas. Global optimization for the phase and chemical equilibrium problem: Application to the NRTL equation. *Computers & Chemical Engineering*, 19(11):1111–1139, 1995. doi:[10.1016/0098-1354\(94\)00106-5](https://doi.org/10.1016/0098-1354(94)00106-5).
- W. F. McDonough and S.-S. Sun. The composition of the Earth. *Chemical Geology*, 120(3-4):223–253, 1995. doi:[10.1016/0009-2541\(94\)00140-4](https://doi.org/10.1016/0009-2541(94)00140-4).
- P. W. Mirwald and H.-J. Massonne. The low-high quartz and quartz-coesite transition to 40 kbar between 600 °C and 1600 °C and some reconnaissance data on the effect of $NaAlO_2$ component on the low quartz-coesite transition. *Journal of Geophysical Research*, 85(B12):6983–6990, January 1980. doi:[10.1029/JB085iB12p06983](https://doi.org/10.1029/JB085iB12p06983).
- N. Miyajima, K. Fujino, N. Funamori, T. Kondo, and T. Yagi. Garnet-perovskite transformation under conditions of the Earth's lower mantle: An analytical transmission electron microscopy study. *Physics of the Earth and Planetary Interiors*, 116(1-4):117–131, 1999. doi:[10.1016/S0031-9201\(99\)00127-2](https://doi.org/10.1016/S0031-9201(99)00127-2).
- J.-P. Montagner and B. L. N. Kennett. How to reconcile body-wave and normal-mode reference Earth models. *Geophysical Journal International*, 125(1):229–248, 1996. doi:[10.1111/j.1365-246X.1996.tb06548.x](https://doi.org/10.1111/j.1365-246X.1996.tb06548.x).

- S. D. Mora, L. Boschi, P. J. Tackley, T. Nakagawa, and D. Giardini. Low seismic resolution cannot explain S/P decorrelation in the lower mantle. *Geophysical Research Letters*, 38, 2011. doi:[10.1029/2011GL047559](https://doi.org/10.1029/2011GL047559).
- H. Morishima, E. Ohtani, T. Kato, O. Shimomura, and T. Kikegawa. Thermal expansion of MgSiO₃ perovskite at 20.5 GPa. *Geophysical Research Letters*, 21(10):899–902, 1994. doi:[10.1029/94GL00844](https://doi.org/10.1029/94GL00844).
- H. Morishima, E. Ohtani, T. Kato, T. Kubo, A. Suzuki, T. Kikegawa, and O. Shimomura. The high-pressure and temperature equation of state of a majorite solid solution in the system of Mg₄Si₄O₁₂-Mg₃Al₂Si₃O₁₂. *Physics and Chemistry of Minerals*, 27(1): 3–10, 1999. doi:[10.1007/s002690050234](https://doi.org/10.1007/s002690050234).
- Y.-M. Muggianu, M. Gambino, and J.-P. Bros. Enthalpies de formation des alliages liquides Bismuth-Étain-Gallium à 723 K. choix d'une représentation analytique des grandeurs d'excès intégrales et partielles de mélange. *Journal de Chimie Physique et de Physico-Chimie Biologique*, 72(1):83–88, 1975. doi:[10.1051/jcp/1975720083](https://doi.org/10.1051/jcp/1975720083).
- B. Mukhopadhyay, S. Basu, and M. J. Holdaway. A discussion of Margules-type formulations for multicomponent solutions with a generalized approach. *Geochimica et Cosmochimica Acta*, 57(2):277–283, 1993. doi:[10.1016/0016-7037\(93\)90430-5](https://doi.org/10.1016/0016-7037(93)90430-5).
- M. Murakami and K. Hirose. Post-perovskite phase transition and mineral chemistry in the pyrolitic lowermost mantle. *Geophysical Research Letters*, 32:L03304, 2005. doi:[10.1029/2004GL021956](https://doi.org/10.1029/2004GL021956).
- M. Murakami, S. V. Sinogeikin, H. Hellwig, J. D. Bass, and J. Li. Sound velocity of MgSiO₃ perovskite to Mbar pressure. *Earth and Planetary Science Letters*, 256:47–54, 2007. doi:[10.1016/j.epsl.2007-01-011](https://doi.org/10.1016/j.epsl.2007-01-011).
- M. Murakami, Y. Ohishi, N. Hirao, and K. Hirose. Elasticity of MgO to 130 GPa: Implications for lower mantle mineralogy. *Earth and Planetary Science Letters*, 277:123–129, 2009. doi:[10.1016/j.epsl.2008-10-010](https://doi.org/10.1016/j.epsl.2008-10-010).
- M. Murakami, Y. Ohishi, N. Hirao, and K. Hirose. A perovskitic lower mantle inferred from high-pressure, high-temperature sound velocity data. *Nature*, 485:90–95, 2012. doi:[10.1038/nature11004](https://doi.org/10.1038/nature11004).
- F. D. Murnaghan. The compressibility of media under extreme pressures. *Proceedings of the National Academy of Sciences of the United States of America*, 30:244–247, 1944. doi:[10.1073/pnas.30.9.244](https://doi.org/10.1073/pnas.30.9.244).
- T. Nakagawa, P. J. Tackley, F. Deschamps, and J. A. D. Connolly. Incorporating self-consistently calculated mineral physics into thermochemical mantle convection simulations in a 3-d spherical shell and its influence on seismic anomalies in Earth's mantle. *Geochemistry, Geophysics, Geosystems*, 10(3), 2009. doi:[10.1029/2008GC002280](https://doi.org/10.1029/2008GC002280).
- T. Nakagawa, P. J. Tackley, F. Deschamps, and J. A. Connolly. The influence of MORB and harzburgite composition on thermo-chemical mantle convection in a 3-D

- spherical shell with self-consistently calculated mineral physics. *Earth and Planetary Science Letters*, 296:403–412, 2010. doi:[10.1016/j.epsl.2010.05.026](https://doi.org/10.1016/j.epsl.2010.05.026).
- T. Nakagawa, P. J. Tackley, F. Deschamps, and J. A. D. Connolly. Radial 1-D seismic structures in the deep mantle in mantle convection simulations with self-consistently calculated mineralogy. *Geochemistry, Geophysics, Geosystems*, 13(11):Q11002, 2012. doi:[10.1029/2012GC004325](https://doi.org/10.1029/2012GC004325).
- Y. Nakajima, D. J. Frost, and D. C. Rubie. Ferrous iron partitioning between magnesium silicate perovskite and ferropericlase and the composition of perovskite in the Earth's lower mantle. *Journal of Geophysical Research*, 117:B08201, 2012. doi:[10.1029/2012JB009151](https://doi.org/10.1029/2012JB009151).
- R. Newton, T. Charlu, P. Anderson, and O. Kleppa. Thermochemistry of synthetic clinopyroxenes on the join $\text{CaMgSi}_2\text{O}_6$ - $\text{Mg}_2\text{Si}_2\text{O}_6$. *Geochimica et Cosmochimica Acta*, 43(1):55–60, 1979. doi:[10.1016/0016-7037\(79\)90046-2](https://doi.org/10.1016/0016-7037(79)90046-2).
- P. J. O'Brien and J. Rötzler. High-pressure granulites: Formation, recovery of peak conditions and implications for tectonics. *Journal of Metamorphic Geology*, 21(1):3–20, 2003. doi:[10.1046/j.1525-1314.2003.00420.x](https://doi.org/10.1046/j.1525-1314.2003.00420.x).
- K. Ohta, K. Hirose, T. Lay, N. Sata, and Y. Ohishi. Phase transitions in pyrolite and MORB at lowermost mantle conditions: Implications for a MORB-rich pile above the core-mantle boundary. *Earth and Planetary Science Letters*, 267:107–117, 2008. doi:[10.1016/j.epsl.2007.11.037](https://doi.org/10.1016/j.epsl.2007.11.037).
- E. Ohtani, N. Kagawa, and K. Fujino. Stability of majorite $(\text{Mg,Fe})\text{SiO}_3$ at high pressures and 1800 °C. *Earth and Planetary Science Letters*, 102(2):158–166, 1991. doi:[10.1016/0012-821X\(91\)90005-3](https://doi.org/10.1016/0012-821X(91)90005-3).
- B. Olinger. Compression studies of forsterite $(\text{Mg}_2\text{SiO}_4)$ and enstatite (MgSiO_3) . In *High-Pressure Research: Applications in Geophysics*, pages 325–334. Academic, New York, 1977.
- B. O'Neill, J. Bass, J. Smyth, and M. Vaughan. Elasticity of a grossular-pyrope-almandine garnet. *Journal of Geophysical Research*, 94:17819, 1989. doi:[10.1029/JB094iB12p17819](https://doi.org/10.1029/JB094iB12p17819).
- S. Ono and A. R. Oganov. In situ observations of phase transition between perovskite and CaIrO_3 -type phase in MgSiO_3 and pyrolitic mantle composition. *Earth and Planetary Science Letters*, 236:914–932, 2005. doi:[10.1016/j.epsl.2005.06.001](https://doi.org/10.1016/j.epsl.2005.06.001).
- S. Ono, T. Katsura, E. Ito, M. Kanzaki, A. Yoneda, M. J. Walter, S. Urakawa, W. Utsumi, and K. Funakoshi. In situ observation of ilmenite-perovskite phase transition in MgSiO_3 using synchrotron radiation. *Geophysical Research Letters*, 28(5):835–838, 2001. doi:[10.1029/1999GL008446](https://doi.org/10.1029/1999GL008446).
- S. Ono, K. Hirose, M. Murakami, and M. Isshiki. Post-stishovite phase boundary in SiO_2 determined by in situ X-ray observations. *Earth and Planetary Science Letters*, 197(3-4):187–192, 2002. doi:[10.1016/S0012-821X\(02\)00479-X](https://doi.org/10.1016/S0012-821X(02)00479-X).

- H. Palme. Chemical abundances in meteorites. *Reviews in Modern Astronomy*, 1:28–51, 1988. doi:[10.1007/978-3-642-74188-3_2](https://doi.org/10.1007/978-3-642-74188-3_2).
- H. Palme and H. S. C. O'Neill. Cosmochemical estimates of mantle composition. In *Treatise on Geochemistry*, chapter 3.1, pages 1–39. Elsevier, 2016. doi:[10.1016/B978-0-08-095975-7.00201-1](https://doi.org/10.1016/B978-0-08-095975-7.00201-1).
- M. G. Pamato, A. Kurnosov, T. B. Ballaran, D. J. Frost, L. Ziberna, M. Giannini, S. Speziale, S. N. Tkachev, K. K. Zhuravlev, and V. B. Prakapenka. Single crystal elasticity of majoritic garnets: Stagnant slabs and thermal anomalies at the base of the transition zone. *Earth and Planetary Science Letters*, 451:114–124, 2016. doi:[10.1016/j.epsl.2016.07.019](https://doi.org/10.1016/j.epsl.2016.07.019).
- A. Pavese, V. Diella, V. Pischedda, M. Merli, R. Bocchio, and M. Mezouar. Pressure-volume-temperature equation of state of andradite and grossular, by high-pressure and -temperature powder diffraction. *Physics and Chemistry of Minerals*, 28(4):242–248, 2001. doi:[10.1007/s002690000144](https://doi.org/10.1007/s002690000144).
- S. M. Peacock, P. E. van Keken, S. D. Holloway, B. R. Hacker, G. A. Abers, and R. L. Fergason. Thermal structure of the Costa Rica – Nicaragua subduction zone. *Physics of the Earth and Planetary Interiors*, 149:187–200, 2005. doi:[10.1016/j.pepi.2004.08.030](https://doi.org/10.1016/j.pepi.2004.08.030).
- A. D. Pelton. A general “geometric” thermodynamic model for multicomponent solutions. *Calphad*, 25(2):319–328, 2001. doi:[10.1016/S0364-5916\(01\)00052-9](https://doi.org/10.1016/S0364-5916(01)00052-9).
- A. S. Piazzoni, G. Steinle-Neumann, H.-P. Bunge, and D. Dolejš. A mineralogical model for density and elasticity of the Earth’s mantle. *Geochemistry, Geophysics, Geosystems*, 8(11):Q11010, 2007. doi:[10.1029/2007GC001697](https://doi.org/10.1029/2007GC001697).
- J.-P. Poirier. *Introduction to the Physics of the Earth’s Interior*. Cambridge University Press, 2 edition, 2000.
- R. Powell. A comparison of some mixing models for crystalline silicate solid solutions. *Contributions to Mineralogy and Petrology*, 46(4):265–274, 1974. doi:[10.1007/BF00370967](https://doi.org/10.1007/BF00370967).
- R. Powell. Darken quadratic formalism and the thermodynamics of minerals. *American Mineralogist*, 72(1-2):1–11, 1987.
- R. Powell and T. Holland. On the formulation of simple mixing models for complex phases. *American Mineralogist*, 78(11-12):1174–1180, 1993.
- R. Powell and T. J. B. Holland. An internally consistent thermodynamic dataset with uncertainties and correlations: 1. Methods and worked example. *Journal of Metamorphic Geology*, 3(4):327–342, 1985. doi:[10.1111/j.1525-1314.1985.tb00324.x](https://doi.org/10.1111/j.1525-1314.1985.tb00324.x).
- R. Powell, T. J. B. Holland, and B. Worley. Calculating phase diagrams involving solid solutions via non-linear equations, with examples using THERMOCALC. *Journal of Metamorphic Geology*, 16(4):577–588, 1998. doi:[10.1111/j.1525-1314.1998.00157.x](https://doi.org/10.1111/j.1525-1314.1998.00157.x).

- C. Prescher, F. Langenhorst, L. S. Dubrovinsky, V. B. Prakapenka, and N. Miyajima. The effect of Fe spin crossovers on its partitioning behavior and oxidation state in a pyrolitic Earth's lower mantle system. *Earth and Planetary Science Letters*, 399: 86–91, 2014. doi:[10.1016/j.epsl.2014.05.011](https://doi.org/10.1016/j.epsl.2014.05.011).
- D. C. Presnall and J. D. Hoover. High pressure phase equilibrium constraints on the origin of mid-ocean ridge basalts. In *Magmatic processes: Physicochemical Principles*, volume 1, pages 75–88. Geochemical Society University Park, Pa., 1987.
- D. C. Presnall, Y.-H. Weng, C. S. Milholland, and M. J. Walter. Liquidus phase relations in the system MgO-MgSiO₃ at pressures up to 25 GPa – constraints on crystallization of a molten hadean mantle. *Physics of the Earth and Planetary Interiors*, 107:83–95, 1998. doi:[10.1016/S0031-9201\(97\)00126-X](https://doi.org/10.1016/S0031-9201(97)00126-X).
- A. Putnis. *An introduction to mineral sciences*. Cambridge University Press, 1992.
- Y. Ricard, E. Mattern, and J. Matas. Synthetic tomographic images of slabs from mineral physics. In *Earth's Deep Mantle: Structure, Composition, and Evolution*, pages 283–300. American Geophysical Union, 2005. doi:[10.1029/160GM17](https://doi.org/10.1029/160GM17).
- F. M. Richter. Finite amplitude convection through a phase boundary. *Geophysical Journal of the Royal Astronomical Society*, 35(1-3):265–276, 1973. doi:[10.1111/j.1365-246X.1973.tb02427.x](https://doi.org/10.1111/j.1365-246X.1973.tb02427.x).
- A. Ricolleau, Y. Fei, E. Cottrell, H. Watson, L. Deng, L. Z. G. Fiquet, A.-L. Auzende, M. Roskosz, G. Morard, and V. Prakapenka. Density profile of pyrolite under the lower mantle conditions. *Geophysical Research Letters*, 36:L06302, 2009. doi:[10.1029/2008GL036759](https://doi.org/10.1029/2008GL036759).
- A. Ricolleau, J.-P. Perrillat, G. Fiquet, I. Daniel, J. Matas, A. Addad, N. Menguy, H. Cardon, M. Mezouar, and N. Guignot. Phase relations and equation of state of a natural MORB: Implications for the density profile of subducted oceanic crust in the Earth's lower mantle. *Journal of Geophysical Research*, 115:B08202, 2010. doi:[10.1029/2009JB006709](https://doi.org/10.1029/2009JB006709).
- J. Ritsema, P. Cupillard, B. Tauzin, W. Xu, L. Stixrude, and C. Lithgow-Bertelloni. Joint mineral physics and seismic wave traveltime analysis of upper mantle temperature. *Geology*, 37(4):363–366, 2009a. doi:[10.1130/G25428A.1](https://doi.org/10.1130/G25428A.1).
- J. Ritsema, W. Xu, L. Stixrude, and C. Lithgow-Bertelloni. Estimates of the transition zone temperature in a mechanically mixed upper mantle. *Earth and Planetary Science Letters*, 277(1-2):244–252, 2009b. doi:[10.1016/j.epsl.2008.10.024](https://doi.org/10.1016/j.epsl.2008.10.024).
- J. Ritsema, A. Deuss, H. J. van Heijst, and J. H. Woodhouse. S40RTS: a degree-40 shear-velocity model for the mantle from new Rayleigh wave dispersion, teleseismic traveltime and normal-mode splitting function measurements. *Geophysical Journal International*, 184(3):1223–1236, March 2011. doi:[10.1111/j.1365-246X.2010.04884.x](https://doi.org/10.1111/j.1365-246X.2010.04884.x).
- R. A. Robie and B. S. Hemingway. Thermodynamic properties of minerals and related substances at 298.15 K and 1 kbar pressure and at higher temperatures. *U.S. Geological Survey Bulletin*, 2131:461–461, 1995.

- R. A. Robie, C. B. Finch, and B. S. Hemingway. Heat capacity and entropy of fayalite (Fe_2SiO_4) between 5.1 and 383 K: Comparison of calorimetric and equilibrium values for the QFM buffer reaction. *American Mineralogist*, 67:463–469, 1982.
- A. Saikia, D. J. Frost, and D. C. Rubie. Splitting of the 520-kilometer seismic discontinuity and chemical heterogeneity in the mantle. *Science*, 319(5869):1515–1518, 2008. doi:[10.1126/science.1152818](https://doi.org/10.1126/science.1152818).
- T. Sakai, E. Ohtani, H. Terasaki, N. Sawada, Y. Kobayashi, M. Miyahara, M. Nishijima, N. Hirao, Y. Ohishi, and T. Kikegawa. Fe-Mg partitioning between perovskite and ferropericlase in the lower mantle. *American Mineralogist*, 94:921–925, 2009. doi:[10.2138/am.2009.3123](https://doi.org/10.2138/am.2009.3123).
- E. Sarafian, G. A. Gaetani, E. H. Hauri, and A. R. Sarafian. Experimental constraints on the damp peridotite solidus and oceanic mantle potential temperature. *Science*, 355(6328):942–944, 2017. doi:[10.1126/science.aaj2165](https://doi.org/10.1126/science.aaj2165).
- H. Sawamoto. *Phase diagram of MgSiO_3 at pressures up to 24 GPa and temperatures up to 2200 °C: Phase stability and properties of tetragonal garnet*, volume 39 of *Geophysical Monograph*, pages 209–219. Terra Scientific Publishing Company, 1987.
- S. K. Saxena and G. Eriksson. Theoretical computation of mineral assemblages in pyrolite and lherzolite. *Journal of Petrology*, 24(4):538–555, November 1983. doi:[10.1093/petrology/24.4.538](https://doi.org/10.1093/petrology/24.4.538).
- K. Schaber, H.-P. Bunge, B. S. A. Schuberth, R. Malservisi, and A. Horbach. Stability of the rotation axis in high-resolution mantle circulation models: Weak polar wander despite strong core heating. *Geochemistry, Geophysics, Geosystems*, 10(11):Q11W04, 2009. doi:[10.1029/2009GC002541](https://doi.org/10.1029/2009GC002541).
- R. Schmid-Fetzer and J. Gröbner. Focused development of magnesium alloys using the Calphad approach. *Advanced Engineering Materials*, 3(12):947–961, 2001. doi:[10.1002/1527-2648\(200112\)3:12<947::AID-ADEM947>3.0.CO;2-P](https://doi.org/10.1002/1527-2648(200112)3:12<947::AID-ADEM947>3.0.CO;2-P).
- G. Schubert, D. A. Yuen, and D. L. Turcotte. Role of phase transitions in a dynamic mantle. *Geophysical Journal of the Royal Astronomical Society*, 42:705–735, 1975. doi:[10.1111/j.1365-246X.1975.tb05888.x](https://doi.org/10.1111/j.1365-246X.1975.tb05888.x).
- G. Schubert, D. Turcotte, and P. Olson. *Mantle Convection in the Earth and Planets*. Cambridge University Press, 2001.
- B. S. A. Schuberth, H.-P. Bunge, and J. Ritsema. Tomographic filtering of high-resolution mantle circulation models: Can seismic heterogeneity be explained by temperature alone? *Geochemistry, Geophysics, Geosystems*, 10:Q05W03, 2009a. doi:[10.1029/2009GC002401](https://doi.org/10.1029/2009GC002401).
- B. S. A. Schuberth, H.-P. Bunge, G. Steinle-Neumann, C. Moder, and J. Oeser. Thermal versus elastic heterogeneity in high-resolution mantle circulation models with pyrolite composition: High plume excess temperatures in the lowermost mantle. *Geochemistry, Geophysics, Geosystems*, 10(1):Q01W01, 2009b. doi:[10.1029/2008GC002235](https://doi.org/10.1029/2008GC002235).

- B. S. A. Schuberth, C. Zanolli, and G. Nolet. Synthetic seismograms for a synthetic Earth: Long-period P- and S-wave traveltimes variations can be explained by temperature alone. *Geophysical Journal International*, 188:1393–1412, 2012. doi:[10.1111/j.1365-246X.2011.05333.x](https://doi.org/10.1111/j.1365-246X.2011.05333.x).
- B. S. A. Schuberth, C. Zanolli, and G. Nolet. Traveltime dispersion in an isotropic elastic mantle: Strong lower-mantle signal in differential-frequency residuals. *Geophysical Journal International*, 203:2099–2118, 2015. doi:[10.1093/gji/ggv389](https://doi.org/10.1093/gji/ggv389).
- S. Shang, H. Zhang, S. Ganeshan, and Z.-K. Liu. The development and application of a thermodynamic database for magnesium alloys. *JOM*, 60(12):45–47, 2008. doi:[10.1007/s11837-008-0165-1](https://doi.org/10.1007/s11837-008-0165-1).
- N. Shapiro, K. B. Olsen, and S. Singh. Wave-guide effects in subduction zones: Evidence from three-dimensional modeling. *Geophysical Research Letters*, 27(3):433–436, 2000. doi:[10.1029/1999GL010982](https://doi.org/10.1029/1999GL010982).
- S. R. Shieh and T. S. Duffy. Strength and elasticity of SiO₂ across the stishovite – CaCl₂-type structural phase boundary. *Physical Review Letters*, 89(25):255507, 2002. doi:[10.1103/PhysRevLett.89.255507](https://doi.org/10.1103/PhysRevLett.89.255507).
- A. Shimojuku, T. Kubo, E. Ohtani, T. Nakamura, R. Okazaki, R. Dohmen, and S. Chakraborty. Si and O diffusion in (Mg,Fe)₂SiO₄ wadsleyite and ringwoodite and its implications for the rheology of the mantle transition zone. *Earth and Planetary Science Letters*, 284:103–112, 2009. doi:[10.1016/j.epsl.2009.04.014](https://doi.org/10.1016/j.epsl.2009.04.014).
- R. Sinmyo and K. Hirose. Iron partitioning in pyrolytic lower mantle. *Physics and Chemistry of Minerals*, 40:107–113, 2013. doi:[10.1007/s00269-012-0551-7](https://doi.org/10.1007/s00269-012-0551-7).
- S. Sinogeikin, T. Katsura, and J. Bass. Sound velocities and elastic properties of Fe-bearing wadsleyite and ringwoodite. *Journal of Geophysical Research*, 103(B9):20819–20825, 1998. doi:[10.1029/98JB01819](https://doi.org/10.1029/98JB01819).
- S. V. Sinogeikin and J. D. Bass. Elasticity of pyrope and majorite-pyrope solid solutions to high temperatures. *Earth and Planetary Science Letters*, 203:549–555, 2002a. doi:[10.1016/S0012-821X\(02\)00851-8](https://doi.org/10.1016/S0012-821X(02)00851-8).
- S. V. Sinogeikin and J. D. Bass. Elasticity of majorite and a majorite-pyrope solid solution to high pressure: Implications for the transition zone. *Geophysical Research Letters*, 29(2):1017, 2002b. doi:[10.1029/2001GL013937](https://doi.org/10.1029/2001GL013937).
- S. V. Sinogeikin, J. D. Bass, and T. Katsura. Single-crystal elasticity of ringwoodite to high pressures and high temperatures: Implications for 520 km seismic discontinuity. *Physics of the Earth and Planetary Interiors*, 136:41–66, 2003. doi:[10.1016/S0031-9201\(03\)00022-0](https://doi.org/10.1016/S0031-9201(03)00022-0).
- F. Sohl and G. Schubert. Interior structure, composition, and mineralogy of the terrestrial planets. In *Treatise on Geophysics*, volume 10, chapter 10.02, pages 23–64. Elsevier, 2015.

- D. Spielman and S.-H. Teng. Smoothed analysis of algorithms: Why the simplex algorithm usually takes polynomial time. In *Proceedings of the Thirty-third Annual ACM Symposium on Theory of Computing*, STOC '01, pages 296–305, New York, NY, USA, 2001. ACM. doi:[10.1145/380752.380813](https://doi.org/10.1145/380752.380813).
- F. D. Stacey and P. M. Davis. *Physics of the Earth*. Cambridge University Press, New York, 4 edition, 2008.
- L. Stixrude and C. Lithgow-Bertelloni. Mineralogy and elasticity of the oceanic upper mantle: Origin of the low-velocity zone. *Journal of Geophysical Research*, 110: B03204, 2005a. doi:[10.1029/2004JB002965](https://doi.org/10.1029/2004JB002965).
- L. Stixrude and C. Lithgow-Bertelloni. Thermodynamics of mantle minerals – I. Physical properties. *Geophysical Journal International*, 162:610–632, 2005b. doi:[10.1111/j.1365-246X.2005.02642.x](https://doi.org/10.1111/j.1365-246X.2005.02642.x).
- L. Stixrude and C. Lithgow-Bertelloni. Influence of phase transformations on lateral heterogeneity and dynamics in Earth's mantle. *Earth and Planetary Science Letters*, 263:45–55, 2007. doi:[10.1016/j.epsl.2007-08-027](https://doi.org/10.1016/j.epsl.2007-08-027).
- L. Stixrude and C. Lithgow-Bertelloni. Thermodynamics of mantle minerals – II. Phase equilibria. *Geophysical Journal International*, 184:1180–1213, 2011. doi:[10.1111/j.1365-246X.2010.04890.x](https://doi.org/10.1111/j.1365-246X.2010.04890.x).
- K. Stowe. *An Introduction to Thermodynamics and Statistical Mechanics*. Cambridge University Press, 2 edition, 2007.
- E. Styles, D. R. Davies, and S. Goes. Mapping spherical seismic into physical structure: Biases from 3-d phase-transition and thermal boundary-layer heterogeneity. *Geophysical Journal International*, 184(3):1371–1378, 2011. doi:[10.1111/j.1365-246X.2010.04914.x](https://doi.org/10.1111/j.1365-246X.2010.04914.x).
- A. Suzuki, E. Ohtani, H. Morishima, T. Kubo, Y. Kanbe, T. Kondo, T. Okada, H. Terasaki, T. Kato, and T. Kikegawa. In situ determination of the phase boundary between wadsleyite and ringwoodite in Mg_2SiO_4 . *Geophysical Research Letters*, 27(6):803–806, 2000. doi:[10.1029/1999GL008425](https://doi.org/10.1029/1999GL008425).
- V. Swamy, S. K. Saxena, B. Sundman, and J. Zhang. A thermodynamic assessment of silica phase diagram. *Journal of Geophysical Research*, 99(B6):11787–11794, 1994. doi:[10.1029/93JB02968](https://doi.org/10.1029/93JB02968).
- E. M. Syracuse, P. E. van Keken, and G. A. Abers. The global range of subduction zone thermal models. *Physics of the Earth and Planetary Interiors*, 183:73–90, 2010. doi:[10.1016/j.pepi.2010.02.004](https://doi.org/10.1016/j.pepi.2010.02.004).
- P. J. Tackley. Living dead slabs in 3-D: The dynamics of compositionally-stratified slabs entering a “slab graveyard” above the core-mantle boundary. *Physics of the Earth and Planetary Interiors*, 188(3-4):150–162, 2011. doi:[10.1016/j.pepi.2011.04.013](https://doi.org/10.1016/j.pepi.2011.04.013).

- S. Tanaka. Possibility of a low P-wave velocity layer in the outermost core from global SmKS waveforms. *Earth and Planetary Science Letters*, 259(3-4):486–499, 2007. doi:[10.1016/j.epsl.2007.05.007](https://doi.org/10.1016/j.epsl.2007.05.007).
- S. Tateno, K. Hirose, N. Sata, and Y. Ohishi. Determination of post-perovskite phase transition boundary up to 4400 K and implications for thermal structure in D" layer. *Earth and Planetary Science Letters*, 277:130–136, 2009. doi:[10.1016/j.epsl.2008.10.004](https://doi.org/10.1016/j.epsl.2008.10.004).
- A. Tesoniero, F. Cammarano, and L. Boschi. S-to-P heterogeneity ratio in the lower mantle and thermo-chemical implications. *Geochemistry, Geophysics, Geosystems*, 17(7):2522–2538, 2016. doi:[10.1002/2016GC006293](https://doi.org/10.1002/2016GC006293).
- M. Tirone, S. Buhre, H. Schmück, and K. Faak. Chemical heterogeneities in the mantle: The equilibrium thermodynamic approach. *Lithos*, 244:140–150, 2016. doi:[10.1016/j.lithos.2015.11.032](https://doi.org/10.1016/j.lithos.2015.11.032).
- G. W. Toop. Predicting ternary activities using binary data. *Transactions of the Metallurgical Society of AIME*, 233:850–855, 1965.
- J. Trampert, F. Deschamps, J. Resovsky, and D. Yuen. Probabilistic tomography maps chemical heterogeneities throughout the lower mantle. *Science*, 306:853–856, 2004. doi:[10.1126/science.1101996](https://doi.org/10.1126/science.1101996).
- D. L. Turcotte and G. Schubert. *Geodynamics*. Cambridge University Press, 2002.
- W. Utsumi, N. Funamori, T. Yagi, E. Ito, T. Kikegawa, and O. Shimomura. Thermal expansivity of MgSiO₃ perovskite under high pressures up to 20 GPa. *Geophysical Research Letters*, 22(9):1005–1008, 1995. doi:[10.1029/95GL00584](https://doi.org/10.1029/95GL00584).
- P. Vacher, A. Mocquet, and C. Sotin. Computation of seismic profiles from mineral physics: The importance of the non-olivine components for explaining the 660 km depth discontinuity. *Physics of the Earth and Planetary Interiors*, 106(3-4):275–298, 1998. doi:[10.1016/S0031-9201\(98\)00076-4](https://doi.org/10.1016/S0031-9201(98)00076-4).
- P. E. van Keken, B. R. Hacker, E. M. Syracuse, and G. A. Abers. Subduction factory: 4. Depth-dependent flux of H₂O from subducting slabs worldwide. *Journal of Geophysical Research*, 116:B01401, 2011. doi:[10.1029/2010JB007922](https://doi.org/10.1029/2010JB007922).
- J. Verhoogen. Phase changes and convection in the Earth's mantle. *Philosophical Transactions of the Royal Society of London*, 258(1088):276–283, October 1965. doi:[10.1098/rsta.1965.0040](https://doi.org/10.1098/rsta.1965.0040).
- V. L. Vinograd. Configurational entropy of binary solid solutions. In *EMU Notes in Mineralogy: Solid solutions in silicate and oxide systems*, volume 3, chapter 12, pages 303–346. Eötvös University Press, Budapest, 2001.
- X. Wang, T. Tsuchiya, and A. Hase. Computational support for a pyrolitic lower mantle containing ferric iron. *Nature Geoscience*, 8:556–560, 2015. doi:[10.1038/NGEO2458](https://doi.org/10.1038/NGEO2458).

- Y. Wang, S. Shang, L.-Q. Chen, and Z.-K. Liu. Density functional theory-based database development and CALPHAD automation. *JOM*, 65(11):1533–1539, 2013. doi:[10.1007/s11837-013-0751-8](https://doi.org/10.1007/s11837-013-0751-8).
- H. Watanabe. Thermochemical properties of synthetic high-pressure compounds relevant to the Earth's mantle. In S. Akimoto and M. H. Manghnani, editors, *High-Pressure Research in Geophysics*, volume 12 of *Advances in Earth and Planetary Sciences*, pages 441–464. Center for Academic Publications, Tokyo, 1982.
- D. J. Weidner. A mineral physics test of a pyrolite mantle. *Geophysical Research Letters*, 12(7):417–420, 1985. doi:[10.1029/GL012i007p00417](https://doi.org/10.1029/GL012i007p00417).
- S. Wen and H. Nekvasil. SOLV CALC: An interactive graphics program package for calculating the ternary feldspar solvus and for two-feldspar geothermometry. *Computers and Geosciences*, 20(6):1025–1040, 1994. doi:[10.1016/0098-3004\(94\)90039-6](https://doi.org/10.1016/0098-3004(94)90039-6).
- W. B. White, S. M. Johnson, and G. B. Dantzig. Chemical equilibrium in complex mixtures. *Journal of Chemical Physics*, 28(5):751–755, 1958. doi:[10.1063/1.1744264](https://doi.org/10.1063/1.1744264).
- G. Will, W. Hoffbauer, E. Hinze, and J. Lauterjung. The compressibility of forsterite up to 300 kbar measured with synchrotron radiation. *Physica B*, 139-140:193–197, 1986. doi:[10.1016/0378-4363\(86\)90556-5](https://doi.org/10.1016/0378-4363(86)90556-5).
- B. J. Wood and J. R. Holloway. A thermodynamic model for subsolidus equilibria in the system CaO-MgO-Al₂O₃-SiO₂. *Geochimica et Cosmochimica Acta*, 48(1):159–176, January 1984. doi:[10.1016/0016-7037\(84\)90358-2](https://doi.org/10.1016/0016-7037(84)90358-2).
- R. K. Workman and S. R. Hart. Major and trace element composition of the depleted MORB mantle. *Earth and Planetary Science Letters*, 231(1-2):53–72, 2005. doi:[10.1016/j.epsl.2004.12.005](https://doi.org/10.1016/j.epsl.2004.12.005).
- W. Xu, C. Lithgow-Bertelloni, L. Stixrude, and J. Ritsema. The effect of bulk composition and temperature on mantle seismic structure. *Earth and Planetary Science Letters*, 275:70–79, 2008. doi:[10.1016/j.epsl.2008.08.012](https://doi.org/10.1016/j.epsl.2008.08.012).
- T. Yagi, M. Akaogi, O. Shimomura, T. Suzuki, and S. Akimoto. In situ observation of the olivine-spinel transformation in Fe₂SiO₄ using synchrotron radiation. *Journal of Geophysical Research*, 92(B7):6207–6213, 1987. doi:[10.1029/JB092iB07p06207](https://doi.org/10.1029/JB092iB07p06207).
- G. F. Zellmer, M. Edmonds, and S. M. Straub. *Volatiles in subduction zone magmatism*, volume 410 of *Special Publications*, pages 1–17. Geological Society, London, 2014. doi:[10.1144/SP410.13](https://doi.org/10.1144/SP410.13).
- C.-S. Zha, H.-K. Mao, and R. J. Hemley. Elasticity of MgO and a primary pressure scale to 55 GPa. *Proceedings of the National Academy of Sciences*, 97(25):13494–13499, 2000. doi:[10.1073/pnas.240466697](https://doi.org/10.1073/pnas.240466697).
- J. Zhang, R. C. Liebermann, T. Gasparik, C. T. Herzberg, and Y. Fei. Melting and subsolidus relations of SiO₂ at 9–14 GPa. *Journal of Geophysical Research*, 98(B11):19785–19793, 1993. doi:[10.1029/93JB02218](https://doi.org/10.1029/93JB02218).

- L. Zhang, H. Ahsbahs, A. Kutoglu, and C. Geiger. Single-crystal hydrostatic compression of synthetic pyrope, almandine, spessartine, grossular and andradite garnets at high pressures. *Physics and Chemistry of Minerals*, 27(1):52–58, 1999. doi:[10.1007/s002690050240](https://doi.org/10.1007/s002690050240).
- L. Ziberna, S. Klemme, and P. Nimis. Garnet and spinel in fertile and depleted mantle: Insights from thermodynamic modelling. *Contributions to Mineralogy and Petrology*, 166:411–421, 2013. doi:[10.1007/s00410-013-0882-5](https://doi.org/10.1007/s00410-013-0882-5).
- Y. Zou, T. Irifune, S. Gréaux, M. L. Whitaker, T. Shinmei, H. Ohfuji, R. Negishi, and Y. Higo. Elasticity and sound velocities of polycrystalline $\text{Mg}_3\text{Al}_2(\text{SiO}_4)_3$ garnet up to 20 GPa and 1700 K. *Journal of Applied Physics*, 112:014910, 2012. doi:[10.1063/1.4736407](https://doi.org/10.1063/1.4736407).

(Eidesstattliche) Versicherungen und Erklärungen

(§5 Nr.4 PromO)

Hiermit erkläre ich, dass keine Tatsachen vorliegen, die mich nach den gesetzlichen Bestimmungen über die Führung akademischer Grade zur Führung eines Doktorgrades unwürdig erscheinen lassen.

(§8 S.2 Nr.5 PromO)

Hiermit erkläre ich mich damit einverstanden, dass die elektronische Fassung meiner Dissertation unter Wahrung meiner Urheberrechte und des Datenschutzes einer gesonderten Überprüfung hinsichtlich der eigenständigen Anfertigung der Dissertation unterzogen werden kann.

(§8 S.2 Nr.7 PromO)

Hiermit erkläre ich eidesstattlich, dass ich die Dissertation selbständig verfasst und keine anderen als die von mir angegebenen Quellen und Hilfsmittel benutzt habe.

(§8 S.2 Nr.8 PromO)

Ich habe die Dissertation nicht bereits zur Erlangung eines akademischen Grades anderweitig eingereicht und habe auch nicht bereits diese oder eine gleichartige Doktorprüfung endgültig nicht bestanden.

(§8 S.2 Nr.9 PromO)

Hiermit erkläre ich, dass ich keine Hilfe von gewerblichen Promotionsberatern bzw. -vermittlern in Anspruch genommen habe und auch künftig nicht nehmen werde.

Bayreuth, 15.08.2017,

(Thomas Chust)